Long-Term Mechanical Behavior of Yucca Mountain Tuff and its Variability

Final Technical Report for Task ORD-FY04-021

DOE Cooperative Agreement DE-FC28-04RW12232

Jaak J.K. Daemen, Lumin Ma, and Guohua Zhao
Department of Mining Engineering
University of Nevada, Reno

March 2006

Table of Contents

1 Introduction ---------- 1

2 Mechanical Testing ---------- 1
- 2.1 Triaxial Testing ---------- 2
- 2.2 Indirect Splitting Tensile Strength ("Brazilian") Testing ---------- 3
- 2.3 Uniaxial Compression Test ---------- 7
- 2.4 Uniaxial Compression Creep Test ---------- 7
- 2.5 Particle Size Distribution ---------- 7

3 Summary, Conclusions, and Recommendations ---------- 9

4 References ---------- 11

Appendices

1 Triaxial Testing ---------- 22
- 1.1 Summary of results ---------- 23
- 1.2 Force-displacement graphs ---------- 25
- 1.3 Stress-strain graphs ---------- 33
- 1.4 Failure envelopes ---------- 44
- 1.5 Specimen photographs ---------- 46

2 Indirect Tensile Splitting "Brazilian" Tests ---------- 50
- 2.1 Summary of results ---------- 51
- 2.2 Factors influencing tensile strength ---------- 51
- 2.3 Displacement analysis ---------- 62
- 2.4 Contact area (width) and contact pressure distribution ---------- 78
- 2.5 Force-displacement graphs ---------- 84
- 2.6 Photographs ---------- 87

3 Uniaxial Compression Test ---------- 89

4 Uniaxial Compression Creep Test ---------- 95

5 Particle Size Distribution ---------- 101

Attachments

1 Paper - "Stress Rate Dependent Strength of a Welded Tuff in Triaxial Tests", accepted by 41st U.S. Rock Mechanics Symposium, Golden, Colorado, June 2006.

2 Paper Abstract – "Lithophysal Porosity Effect on Mechanical Properties of Welded Topopah Spring Tuff", accepted by 41st Asian Rock Mechanics Symposium, Singapore, November 2006.

1. Introduction

The study of the long term mechanical behavior of Yucca Mountain tuffs is important for several reasons. Long term stability of excavations will affect accessibility (e.g. for inspection purposes), and retrievability. Long term instabilities may induce loading of drip shields and/or emplaced waste, thus affecting drip shield and/or waste package corrosion. Failure of excavations will affect airflow, may affect water flow, and may affect temperature distributions.

The long term mechanical behavior of rocks remains an elusive topic, loaded with uncertainties. A variety of approaches have been used to improve the understanding of this complex subject, but it is doubtful that it has reached a stage where firm predictions can be considered feasible.

The long term mechanical behavior of "soft" rocks, especially evaporites, and in particular rock salt, has been the subject of numerous investigations (e.g. Cristescu and Hunsche, 1998, Cristescu et al, 2002), and basic approaches towards engineering taking into account the long term behavior of such materials have long been well established (e.g. Dreyer, 1972, 1982). The same is certainly not true of "hard" rocks. While it long has been recognized that the long term strength of "hard" rocks almost certainly is significantly less than that measured during "short", i.e. standard (ASTM D 2938), ISRM suggested (Bieniawski et al, 1978) and conventionally used test procedures (e.g. Bieniawski, 1970, Wawersik, 1972, Hoek and Brown, 1980, p. 150), what limited approaches have been taken to develop strategies toward determining the long term mechanical behavior of "hard" rock remain in the early research and investigation stage, at best. One early model developed specifically for time dependent analysis of underground "hard" rock structures is the phenomenological model by Kaiser and Morgenstern (1981). Brady and Brown (1985, p. 93) state that over a wide range of strain rates, from 10^{-8} to 10^{2}/s the difference in strength is only a factor of 2, and that "the observed behavior of rock is not significantly influenced by varying the strain rate within the range that is convenient to use in quasi-static laboratory compression tests." While this is undoubtedly true, it does not really address the question as to whether or not strengths thus measured can be considered appropriate for estimating long term strengths.

One objective of this investigation was to evaluate the applicability of the approaches by Cruden (e.g. Cruden, 1971, 1974, 1983, 1987) and by Lajtai (e.g. Lajtai and Schmidtke, 1986, 1987) to the prediction of the long term mechanical behavior of the investigated tuffs. This involves in particular static fatigue testing, by conducting uniaxial, triaxial, and indirect splitting (Brazilian) tests over a wide range of strain (or stress, or displacement) rates.

2. Mechanical Testing

We have used a variety of mechanical test methods to determine the long term mechanical behavior of the investigated tuffs. The principal approach pursued is to investigate the long term behavior by studying the mechanical behavior over a range of

strain rates, trying to understand the mechanical behavior of the rock at these different strain rates, and try to determine whether and to what extent the behavior can be extrapolated over times well exceeding those of interest for conventional underground construction or mining, but of direct potential importance for repository stability and excavation behavior. The principal test types implemented for this project include triaxial and uniaxial compression, indirect tensile splitting ("Brazilian"), and creep tests.

Most testing performed as part of this project has been done on specimens from the Topopah Spring crystal-poor middle nonlithophysal zone (Tptpmn), with a smaller number of tests on samples from the Topopah Spring crystal-poor lower nonlithophysal zone (Tptpln). Most testing has been done on specimens of 2.4 inch (61 mm) diameter, with a much smaller number on specimens with a 1.77 inch (45 mm) diameter, clearly not a sufficiently wide range to allow a full definition of the size effect, but nevertheless a step in that direction. All testing has been performed on MTS servo-controlled hydraulic test systems.

2.1. Triaxial Testing

Thirty triaxial compression tests have been completed, and for about half of them multiple post-peak loading-unloading cycles have been performed. (When multiple loading-unloading cycles are performed on a sample, the loading steps all are performed at the same displacement rate. The unloading is initiated when the control system detects failure, i.e. a significant load drop, and proceeds relatively quickly, typically in about 5 to 10 minutes. In some cycles an operator set displacement limit was reached, and the cycle thus terminated.). Triaxial testing has been conducted at axial displacement rates from 0.16 to 0.0016 mm/min, corresponding to axial strain rates from about 10^{-5} /s to about 10^{-7} /s (strain rates averaged over the sample length from measured axial displacements), under confining pressures of 5, 10, and 20 MPa. The displacement is controlled with the machine LVDT installed inside the hydraulic cylinder driving the load. Sample information is given in Table 1.1, test conditions and results in Table 1.2, Appendix 1. All but one triaxial test have been performed on samples from the Tptpmn (Topopah Spring middle nonlithophysal) zone, and all on specimens with a nominal 61 mm (2.4 inch) diameter.

The axial force-displacement loading curves virtually all show markedly nonlinear behavior, with the deviation from linearity occurring at about 50 to 60 % of the peak load (Figs. 1.2.1 – 1.2.15), Similar nonlinear behavior is seen in the strain gage results, both for axial and for lateral strain (Figs. 1.3.1 through 1.3.15).

Although the number of results is far from sufficient to allow drawing firm final conclusions, there are strong indications, obtained mainly from cyclic testing, that the tested tuffs are very brittle at confining pressures up to at least 10 MPa (e.g. Figs. 1.3.16, 1.3.18). This confirms observations made during a previous investigation that the tested tuffs are extremely brittle in uniaxial compression (Ma, 2004, Ma and Daemen, 2004). The single cycle force-displacement graphs for virtually all tests suggest rather brittle behavior during the first cycle (Figs. 1.2.1 through 1.2.15). On the other hand at least a

small number of tests at confining pressures of 20 MPa show somewhat less brittle behavior in multiple post-peak cycles. Fig. 1.3.19 illustrates some reduced post-peak stiffness. Figs. 1.3.17 and 1.3.21 illustrate a behavior pattern that has been observed repeatedly: a very steep force drop after the first loading step, and then a sustained load/stress plateau over a quite large displacement distance at an essentially constant load. (In these post-peak cycles the loading was discontinued when an operator set displacement limit was reached). (It is possible that this behavior may be an artifact of the test arrangement, although it is not clear what this would be. Clear is that further testing is needed to establish whether or not and to what extent this is true post-peak rock behavior). Although the data is very preliminary, and far from conclusive, the evidence collected so far strongly suggests that the hypothetical conceptual model postulated by Hudson et al (1973, Fig. 6) may be a very reasonable and appropriate one for the tested tuff, but with the important qualifier included by the authors that it appears that the post peak at faster rates may descend much faster than at slower rates.

Most studies of the effect of strain rate on rock strength have been performed in uniaxial compression. Martin et al (1993) reported a series of unaxial constant strain rate tests on Topopah Spring tuff, under fully saturated conditions. Earlier work by Martin (1972, and Martin and Durham, 1975) already had demonstrated the time dependent fracturing of silicate containing rock in the presence of water.

Kawamoto and Saito (1974) tested cement mortar, sandstone, and tuff, at three strain rates, in uniaxial and triaxial compression, showing the typical strength – strain rate relations. Ray et al (1999) report fatigue cycling of a sandstone at three strain rates. Singh et al (1989) performed uniaxial compression tests on sandstone and on marble at strain rates from 10^{-6} to 10^{3} /s, showing a systematic strength increase with strain rate. Several of these authors comment that the strain at failure appears to be virtually independent of the failure stress (or strain rate), a topic that deserves further investigation.

2.2. Indirect Splitting Tensile Strength ("Brazilian") Testing

One hundred and eleven Brazilian tests have been performed, at machine displacement rates ranging from 0.000145 mm/min to 2 mm/min. Test durations range from a few minutes to tens of hours.

Sample information, test information, and results, are given in Appendix 2. The results should provide a good data base to initiate a static fatigue analysis, but clearly testing over a wider range of strain rates would be desirable, if not essential, to develop statistical significance.

It is striking that many of the fractured specimens show a slightly off center main fracture, curved, apparently closely following a tensile principal stress trajectory (Coker and Filon, 1957, p. 411, Colback, 1966, Figs. 2 and 3, Hiramatsu and Oka, 1970, Fig. 2, Andreev, 1995, Figs. 4.27, 4.28, 4.31) (e.g. Figs. 2.5.7 – 2.5.10). A similar observation was made by Addinall and Hackett, 1964, but they seem to imply only for specimens with a small hole at the center of the disk. They "explain" the deviation as an effect of a

hole size being of the same magnitude as natural discontinuities in the material tested? In most of our tests the primary fracture is accompanied by classical "hourglass" or "triple-cleft" shaped secondary fractures (e.g. Rudnick et al, 1963, Addinall and Hackett, 1964, Colback, 1967, Andreev, 1995, Fig. 4.39). The curved fracture geometry we observe predominantly is very similar to the one observed by Hooper (1971) in glass, except for the fact that we typically observe only one of these "primary" fractures. However, his observation that in glass failure initiates at the loading contact is not consistent with our observations. On multiple occasions specimens that had virtually completely fractured still remained "intact" (barely) at the loaded edges. Nevertheless, the similarities certainly seem sufficient to warrant further study of the Hooper (1971) analysis. Certainly it would be desirable, following Hooper's approach referenced to Gramberg (1965) to pursue a fractographic analysis (e.g. Ameen, 1995) for a more in depth assessment of the mechanics of fracture in the Brazilian tests performed. Brown and Trollope (1968) show curved 'diametrical" fractures (Fig.8), without commenting on the curvature. They also show a fracture surface (Fig 9), using a fractographic approach that indicates failure initiation "near" the center of the disk.

We have given considerable emphasis to the interpretation of displacements measured during indirect tensile splitting tests. The main objective of this aspect of the investigation was to try to determine an explicit measure of the rock stiffness, e.g. in terms of its Young's modulus, on the basis of the simplest possible indirect tensile testing, i.e. by measuring the machine displacement only. If such a determination could be made, reliably and consistently, it would provide an ideal tool to investigate the spatial variability of the rock stiffness, because it requires far less core, sample preparation, test time, and data analysis than compressive testing.

One approach to the displacement analysis has been the use of the displacement formulas given by Jaeger and Cook (1979, Section 10.7). A numerical evaluation of these displacement formulations is given in Appendix 2.3. Problems have been encountered in matching or reconciling these calculated displacements with measured displacements. Investigations into reconciling the discrepancies have been started including measuring the displacements (deformations) of the compressible inserts used during testing, and measuring the test system deformation during testing. Alternative displacement calculations have been considered (e.g. Mushkelishvili, 1963, §80a, 1º; Saada, 1993, Section 19.16). These "solutions" will require considerable further derivations before they can be implemented as a direct numerical formulation.

One possible explanation for the difference between the measured and the calculated displacements may be the fact that the Young's modulus of rock tends to be smaller in tension than in compression (e.g. Price, 1966, p. 8), and hence the behavior may become anisotropic during Brazilian tests. It is possible that the anisotropic solutions that have been published for the Brazilian test could be used for the analysis (e.g. Amadei et al, 1983, Exadaktylos and Kaklis, 2001, Claesson and Bohloli, 2002), or that a bimodular numerical analysis (e.g. Chen and Stimpson, 1993) may be required.

An analysis of this type would require knowing the moduli in tension as well as in compression. Conversely, it may be possible to invert the problem, and calculate the tensile modulus from the displacement measurements if the compressive modulus is known?

One factor that may affect results of Brazilian tests, including deformations, may be the load distribution. Jaeger and Cook (1979), following Hondros (1959), and most rock mechanics authors using Brazilian or similar (e.g. ring) tests assume a uniform contact stress or contact pressure distribution. Such a uniform pressure distribution seems highly unlikely given the contact nature of the problem. Fairhurst (1964), Colback (1966), Vardar and Finnie (1975), among many others, argue that the details of the contact pressure distribution should not be particularly relevant, given that our prime interest is in rock failure, at the center of the disk, i.e. far away from the applied (boundary) stress. This may well be true, is true, but the contact mechanics significantly affects the stress distribution in the contact area, and almost certainly is a major factor in assuring that fracture does not initiate in the contact areas(s). While we recognize that it may be true, is likely true, that the stress state in the center of the disk is largely independent of the load application, e.g. because this is a direct application of Saint Venant's principle (e.g. Saada, 1993, Section 8.13), we investigated the contact stress for other reasons as well, notably because the contact angle is needed in displacement calculations. Results of contact angle measurements are included in Appendix 2, Section 2.4. Measurements of the contact width, and hence contact angle, are subject to fairly large measurement uncertainties (up to 10 % for specimens with 61 mm diameter, possibly larger, up to 15 % for specimens with a 45 mm diameter). Results of contact pressure measurements (using Sensor Products LLC, East Hanover, NJ contact pressure film) are given in Appendix 2.4. Although a detailed numerical analysis of the contact stresses at this time is not yet possible (because the contact stresses are too high, Vadim Shalyt, Sensor Products Inc., personal communication, August 2005), it is clear from the measurements that a parabolic (Hertzian) contact pressure distribution is far more realistic than the assumption of a uniformly distributed pressure. (We were recently informed by Mr. Shalyt (February 20, 2006) that they now can analyze numerically the very high pressure film – it obviously would be most desirable and helpful to perform such numerical determinations, because it would give a much better insight into the actual contact pressures that develop in Brazilian tests). Equally clear from the measurements is that in at least two samples highly localized contact loads develop, almost point loads, presumably caused by the roughness of the contact area. Again, invoking Saint Venant's principle, it may not matter, as long as the principal fracture is initiated at or near the center of the disk, but one has to wonder whether there may be an effect of inducing fracture initiation at or near the loaded edge(s)? (In multiple tests, especially tests run at very low displacement rates, it was clear that the principal fracture did not initiate at the edge(s), because the two halves that were separated in the middle still hung together (although barely) at the edges. An observation identical to one made by Berenbaum and Brodie, 1959, and Mellor and Hawkes, 1971. It is interesting that Gramberg (1989, fig. 12) in what appears to be a very careful fractographic observation of the fractured surface in a Brazilian test locates the initiation point, the fracture nucleus, well off center (although on the compressed diameter).

Several options/approaches may be worthwhile pursuing in order to clarify the effect of the surface roughness on the contact pressure distribution. One method might be to impose smoothness requirements on the contact area, which could be accomplished for example by rounding and smoothing the samples in a lathe, or by grinding the cylindrical (contact) surface area. This would add considerably to the time and hence cost of sample preparation. It may be possible to investigate analytically and/or numerically the influence of surface roughness, although this also would present considerably challenges, both with respect to determining the roughness, and with respect to calculating its effect (e.g. Sayles et al, 1981). Moreover, the analysis would have to be three-dimensional.

Vardar and Finnie (1975) flattened the contact area with the explicit purpose of simplifying the contact pressure and making it uniform over an imposed width.

Hertzian type contact problems pose major analysis challenges, as demonstrated by the fact that it took many decades for correct numerical results to be obtained from the original Hertz formulation (Hertz, 1881), (e.g. Cooper, 1969, Shigley, 1986, p. 79), and that these problems remain difficult to model numerically (e.g. Hilss et al, 1993, p.x). We assume that the contact stresses are strictly normal, i.e. free of shear, an assumption strictly correct only when both bodies in contact have the same moduli (e.g. Lubkin, 1962), an assumption obviously violated in our tests. Moreover, there are fundamental inconsistencies in the application of the "classical" theory to two-dimensional problems (e.g. Schwartz and Harper, 1971). If the contact deformation/pressure is a significant cause of uncertainty about the diametrical compression, its resolution may not be simple.

Mirza et al (1997) calculated the deformations of Brazilian specimens by numerical integration of the diametrical strains. This may be an approach worthwhile pursuing for the analysis of our displacement data. They observed, in their tests on asphalt concrete (bitumen + aggregate mixtures) that the aggregate inclusions/particles significantly affected crack propagation. It is possible that this heterogeneous material behavior may be parallel to the heterogeneity effects in tuff? (In this case, with soft, rather than stiff inclusions?)

Some Brazilian tests have been videorecorded, with the objective of determining the fracture initiation point and the fracture propagation. These measurements have been only partially successful. While the records usually clearly show the prime and secondary fractures, the prime ("diametrical") fracture usually is completely developed in a single frame, providing no information about where the fracture initiates nor about how fast it propagates. The fast completion of the fracture, even at very low loading rates, may confirm the exceedingly brittle behavior of these tuffs?

Most Brazilian testing has been performed on specimens with nominal diameters of 2.4 inch (61 mm), primarily of the Tptpmn (Topopah Spring middle nonlithophysal) formation. Some tests have been performed on specimens with a smaller diameter (1.77 inch (45mm)), thus allowing the beginning of an investigation into size effects, although

clearly not sufficient to allow even a preliminary size effect determination (e.g. Yegulalp and Kim, 1993).

It is striking that the force-displacement graphs of the Brazilian tests consistently show nonlinear behavior (e.g. Figs. 2.5.1 – 2.5.6), although frequently with a linear section as failure is being approached. The initial nonlinearity may be due to the contact area and pressure distribution changing, and/or to intrinsically nonlinear material behavior (as consistently observed in uniaxial and triaxial compression tests)?

2.3. Uniaxial Compression Test

One uniaxial compression test has been performed, on a 2.4 inch (61 mm) diameter sample from the Tptpln (Topopah Spring lower nonlithophysal) formation, at an average axial stress rate of slightly over 9 MPa/min. The specimen failed after slightly less than seven minutes. Details are given in Appendix 3. Figures 3.1 and 3.2 show axial displacement – force and stress – strain loading and unloading curves, suggestive of very brittle behavior.

This test was intended to become a creep test, but the specimen failed before reaching the first intended creep level (70 MPa). The photographs included in Appendix 3 illustrate the extreme heterogeneity of this specimen, which may explain its very low strength? Failure appears to have been predominantly slabbing near one end, although some fairly pervasive axial splitting also is clearly visible.

2.4. Uniaxial Compression Creep Test

One creep test has been performed, on a sample from the Tptpmn formation, with a diameter of 2.4 inch (61 mm). The test, described in Appendix 4, consisted of three loading steps, a typical stepwise creep testing approach (e.g. Kie, 1993). The results are given in Appendix 4. Figure 4.1 shows the force-displacement curves for the three stress levels to which the specimen has been loaded. Figure 4.2 shows the axial stress – axial strain curves. Figure 4.3 shows axial strain as a function of time. Ultimate failure appears to have been fairly localized (Figs 4.4 – 4.8), with a local slab forming on one side, although some additional axial splitting took place.

2.5. Particle size distribution

Simple visual inspection strongly suggests a correlation between strain rate and particle size of the fragments resulting from uniaxial compression tests. Figures 5.1 and 5.2 illustrate this perception. Particle size analysis documented in Appendix 5 confirms this perception, but is in need of further confirmation.

The particle size distribution study was performed by sieving (ASTM C 136, ASTM D 422). The grading, or particle size distribution, is given in Tables 5.1 and 5.2. An initial analysis of the dependency of particle size distribution on strain rate is given in Figures 5.2 through 5.9. These figures confirm the perception that faster strain rates result in

smaller particles. We recognize that the statistical reliability of these results (of this very preliminary study) is uncertain. Reasons for statistical uncertainty include the intrinsically large variability of mechanical properties of Yucca Mountain tuffs, and the relatively small number of tests we have been able to do at very low and at very high strain rates. It obviously would be highly desirable to increase the data base by additional testing, especially in these extreme strain ranges.

Because axial splitting is a major mechanism of tuff failures in uniaxial compression, especially at low strain rates, the fragments resulting from the low strain rates in particular tend to have a markedly elongated shape. This shape effect is not accounted for in the sieving analysis performed here. (In fact, the sieving may have been affected somewhat by manual assistance to assure that particles with highly unequal dimensions were passing the sieve size for the smallest dimension.)

It is well known and has long been recognized that particle shape affects sieving, and, more generally, particle size distribution determinations (e.g. Rosen and Hulburt, 1970, Novak and Thompson, 1986, Ferreira et al, 1993, Hogg et al, 2004). Hence, it certainly would be preferable to repeat particle sizing using techniques that account for any shape effects.

It is clear that a much more comprehensive analysis of the influence of strain rate on failure mechanics would be highly desirable. The most obvious immediate step would be to construct the grading curves for the results obtained. As a next step, this could involve an investigation with more emphasis on the particle shape, rather than on particle size only. A number of techniques are available to pursue such shape investigations. Most basic would be to determine particle shapes according to ASTM D 3398 and/or ASTM D 4791. This would allow classification of the fragments into elongated, flaky, or both (see also Smith and Collis, 1993, pp. 173 – 175, Smith and Collis, 2001, pp. 173 – 175, Primel and Tourenq, 2000, pp. 133-4). In addition, complementary to such most basic measurements would be an analysis following one of a number of well established procedures for determining particle shape characteristics (e.g. in geology/sedimentology (e.g. Wadell, 1933, Krumbein, 1941, Rittenhouse, 1943, Krumbein and Sloss, 1963, pp. 106 - 113) and/or soil mechanics/geotechnical engineering (e.g. Vallerga et al, 1957, Holubec and D'Appolonia, 1973, Dickin, 1973)). These "conventional" or "traditional" approaches are likely to clearly distinguish flaky and/or elongated fragments from more cuboidal or equidimensional ones (e.g. Figures 5.1 and 5.2). In fact, visual observation of the particles suggests that even a simple aspect ratio definition might suffice as a discriminating characteristic? The Rittenhouse (1943) (also Vallejo, 1995) approach may be particularly attractive for this determination, and instructive, because it could provide a quick purely visual estimating framework, without the need for laborious and time consuming manual labor required by more formal numerical schemes. Among these, the axial ratio shape factors (e.g. Eerola and Ylosjoki, 1970) certainly would be expected to be clarifying, although the sphericity/shape factors, according to Barrett (1980), may be better discriminators than simple axial ratios.

An improvement over this basic relatively elementary approach might be to classify the fragments according to the Zingg classification (e.g. Krumbein and Sloss, 1963, Fig. 4-8).

A further improvement undoubtedly would be the use of more comprehensive numerical classifications, e.g. using Fourier and/or fractal analysis (e.g. Ehrlich and Weinberg, 1970, Meloy, 1977, Schwarz and Exner, 1980, Dowdeswell, 1982, Clark, 1986, Meloy and Clark, 1986, Vallejo, 1995, Thomas et al, 1995, Bowman et al, 2001, Wettimuny and Penumadu, 2004). This would allow a much more rigorous definition of the particle shapes (and sizes), and should allow a correlation with induced fracture patterns. We recognize that the immediate physical meaning of the variables involved tends to be lost with such methods, as stated by Kwan et al, 1999, one reason why these methods are considered a complement to rather than a substitute for the more "elementary" conventional but physically more obvious and clearer methods. A most rigorous analysis and discussion of the shape definition issues is presented by MacLeod (2002), which certainly deserves pursuing.

Almost certainly it would be preferable to use some of the more recently developed digital shape acquisition hardware and shape analysis software (e.g. Franklin et al, 1996, Podczeck, 1997, Hundal et al, 1997, Brzezicki and Kasperkiewicz, 1999, Maerz, 2004) for the practical implementation of such analyses.

An implied justification for the study of fragment size/shape as a function of strain rate is that a relation exists between fracture patterns and fragment size/shape. It would be desirable, probably preferable, to directly focus on fracture patterns, rather than indirectly through the study of fragments. Wu and Pollard (1993) convincingly demonstrate a pronounced relation between strain rate and fracture shape and density. It is likely that a study focusing on the fracture geometries would assist in describing and explaining the differences in failure behavior as a function of strain rate. Gramberg (1989) discusses fracture development in some detail, and, specifically (Fig. 17) mentions the "splintering in an explosive way" of glass in uniaxial compression, a rather typical failure mode for the tuffs we tested as well.

3 Summary, Conclusions, and Recommendations

Mechanical testing has been performed to investigate the long term mechanical behavior of Yucca Mountain tuffs. Most of the testing has been performed on specimens from the Topopah Spring crystal-poor middle nonlithophysal (Tptpmn) zone), and some on specimens from the Topopah Spring crystal-poor lower nonlithophysal (Tptpln) zone.

Many of the tested samples are obviously heterogeneous. It may be worthwhile to analyze the mechanical behavior explicitly recognizing this heterogeneity, e.g. following Chen et al, 2004. It certainly would be desirable to normalize all results with respect to density (e.g. Olsson, 1991). This most likely would reduce at least some of the variability. Ideally all such testing should be accompanied by a detailed characterization of the inhomogeneity, in particular distribution, density, shape, etc. distribution of lithophysal cavities and soft vapor-phase altered volumes (e.g. Martin III et al, 1993).

The dominant significant of lithophysal cavities on the mechanical behavior of these tuffs has been recognized and investigated by Karakouzian and associates (e.g. Hudyma, 2001, Avar, 2003, Avar et al, 2003, Hudyma et al, 2004). Price and Bauer (1985) and Price et al (1994) also explicitly address the influence of porosity on mechanical behavior of tuffs.

It is recommended that more cyclic testing be performed, and that the analysis procedures developed by Costin and Holcomb (1981) be applied to the results.

It almost certainly would be productive to pursue damage analysis (e.g. Sun and Hu, 1997, Pan and Wen, 2001).

A high priority would be a continued systematic investigation of the long term strength (and stiffness?) of the various rock types that will form the host rock of an eventual repository. Most promising potential analysis tools have been developed by Cruden (1974, 1987), and Lajtai and co-authors (e.g. Schmidtke and Lajtai, 1985, Lajtai and Schmidtke, 1986, 1987, Lajtai and Bielus, 1986). Ideally long term testing should be conducted under a range of environmental conditions that the rock might be subjected to over the duration of the required repository performance, e.g. with respect to temperature and moisture conditions. In light of the considerable variability of the mechanical properties of these tuffs, it is likely that a considerable number of tests would be required in order to obtain statistically significant results, A combination of uniaxial and triaxial compression tests, with Brazilian and point load tests, might lead to a sufficient data base under a sufficiently wide range of test conditions and for a variety of failure modes.

The effect of water (steam) on the long term mechanical behavior of these tuffs almost certainly deserves much more investigation. It is obvious that the development of a defensible model of the long term mechanical behavior of these tuffs requires considerably more research. As a minimum, a significantly larger data base needs to be developed, in order to assure that the (spatial) variability of the tuffs is adequately understood. Experimental results are needed under the full range of anticipated or likely repository conditions. Rational mechanical models are needed to integrate the data into a credible predictive model.

It clearly would be desirable to perform more detailed petrographic and mineralogical characterization of tested specimens. If only to investigate to what extent such characterizations might allow correlations with mechanical properties, and hence reduce the need for mechanical testing by allowing credible estimates of the mechanical behavior based on mineralogical/petrographical characterizations.

In all probability it would be most helpful to complement mechanical testing with detailed investigations of fractures developing in the specimens (e.g. Åkesson et al, 2004). A better understanding of the physical failure modes might assist in identifying the most appropriate failure model(s).

4. References

Addinall, E. and P. Hackett, 1964, Tensile Failure in Rock-like Materials, pp. 515 – 538, Proceedings of the Sixth Symposium on Rock Mechanics, E.M. Spokes and C.R. Christiansen, The University of Missouri at Rolla.

Amadei, B., J.D. Rogers and R.E. Goodman, 1983, Elastic constants and tensile strength of anisotropic rocks, Proceedings Fifth Congress of the ISRM, Melbourne, Australia, Vol. 1, pp. A189 – A 196, A.A. Balkema, Rotterdam.

Ameen, M.S., Editor, 1995, Fractography: fracture topography as a tool in fracture mechanics and stress analysis, Geological Society Special Publication No. 92, The Geological Society, London.

Andreev, George E., 1995, Brittle Failure of Rock Materials *Test Results and Constitutive Models*, A.A. Balkema, Rotterdam/Brookfield.

Åkesson, Urban, Jan Hansson, and Jimmy Stigh, 2004, Characterisation of microcracks in the Bohus granite, western Sweden, caused by uniaxial cyclic loading, Engineering Geology, Vol. 72, pp. 131 – 142.

ASTM C 136 – 96a, Standard Test Method for Sieve Analysis of Fine and Coarse Aggregates, Annual Book of ASTM Standards 2000, Section 4, Construction, Volume 04.02, Concrete and Aggregates, ASTM, West Conshohocken, PA.

ASTM D 422 – 63 (Reapproved 1998), Standard Test Method for Particle-Size Analysis of Soils, Annual Book of ASTM Standards 2000, Section 4, Construction, Volume 04.08, Soil and Rock (1): D 420 – D 5779, ASTM, West Conshohocken, PA.

ASTM D 2938 – 95, Standard Test Method for Unconfined Compressive Strength of Intact Rock Specimens, Annual Book of ASTM Standards 1996, Section 4, Construction, Volume 04.08, Soil and Rock (1): D 420 – D 4914, ASTM, West Conshohocken, PA

ASTM D 3148 – 96, Standard Test Method for Elastic Moduli of Intact Rock Core Specimens in Uniaxial Compression, Annual Book of ASTM Standards 2000, Section 4, Construction, Volume 04.08, Soil and Rock (1): D 420 – D 5779, ASTM, West Conshohocken, PA.

ASTM D 3398 – 97, Standard Test Method for Index of Aggregate Particle Shape and Texture, Annual Book of ASTM Standards 2000, Section 4, Construction, Volume 04.03, Road and Paving Materials; Vehicle-Pavement Systems, ASTM, West Conshohocken, PA.

ASTM D 3967 – 95a, Standard Test Method for Splitting Tensile Strength of Intact Rock Core Annual Book of ASTM Standards 2000, Section 4, Construction, Volume 04.08, Soil and Rock (1): D 420 – D 5779, ASTM, West Conshohocken, PA., West Conshohocken, PA.

ASTM D 4791 – 99, Standard Test method for Flat particles, Elongated Particles, or Flat and Elongated particles in Coarse Aggregate, Annual Book of ASTM Standards 2000, Section 4, Construction, Volume 04.03, Road and Paving Materials; Vehicle-Pavement Systems, ASTM, West Conshohocken, PA.

Avar, Bahri B., The Influence of Lithophysal Porosity on the In-Situ Stress-Strain Properties of Topopah Spring Tuff, Final Technical Report U.S. DOE/UCCSN Cooperative Agreement, DE-FC28-98NV12081, Document Number TR-02-008, http://hrc.nevada.edu/QA/Report/TR-02-008.pdf.

Avar, B., N. Hudyma, and M. Karakouzian, 2003, Porosity dependence of the elastic modulus of lithophysae-rich tuff: numerical and experimental investigations, International Journal of Rock Mechanics and Mining Sciences, Vol. 40, May, pp. 919-928.

Barrett, P.J., 1980, The shape of rock particles, a critical review, Sedimentology, Vol. 27, pp. 291 – 303.

Berenbaum, R., and I. Brodie, 1959, Measurement of the tensile strength of brittle materials, pp. 281-287, British Journal of Applied Physics, Vol. 12, January.

Bieniawski, Z.T., 1970, Time-Dependent Behaviour of Fractured Rock, Rock Mechanics, Vol. 2, pp. 123-137.

Bieniawski, Z.T., and I. Hawkes, 1977, Suggested Methods for Determining Tensile Strength of Rock Materials, ISRM Commission on Standardization of Laboratory and Field Tests, Committee on Laboratory Tests, Document No. 8, *Int. J. Rock mech. Min. Sci. & Geom. Abstracts,* Vol. 15, No.3, pp. 99-103 (1978).

Bieniawski, Z.T., J.A. Franklin, M.J. Bernede, P. Duffaut, F. Rummel, T. Horibe, E. Broch, E. Rodrigues, W.L. Van Heerden, U.W. Vogler, I. Hansagi, J. Szlavin, B.T. Brady, D.U. Deere, I. Hawkes, and D. Milovanovic, 1978, Suggested Methods for Determining the Uniaxial Compressive Strength and Deformability of Rock Materials, Published in International Journal of Rock Mechanics and Mining Sciences & Geomechanics Abstracts, Vol. 16, No. 2, pp. 135 – 140 (1979), and in Rock Characterization Testing and Monitoring, ISRM Suggested Methods, pp. 113 – 116, E.T. Brown, Editor, Pergamon Press, Oxford, 1981.

Bowman, E.T., K. Soga, and W. Drummond, 2001, Particle shape characterisation using Fourier descriptor analysis, Géotechnique, Vol. 51, No. 6, pp. 545-554.

Brady, B.H.G., and E.T. Brown, 1985, Rock Mechanics For Underground Mining, George Allen & Unwin, London.

Brown, E.T., and D.H. Trollope, The Failure of Brittle Materials under Effective Tensile Stress, Felsmechanik un Ingenieurgeologie – Rock Mechanics and Engineering Geology, Vol. VI, No. 1-2, pp. 229 – 239.

Brzezicki, Jerzy M. and Janusz Kasperkiewicz, 1999, Automatic Image Analysis in Evaluation of Aggregate Shape, Journal of Computing in Civil Engineering, Vol. 13, No. 2, April, pp. 123 – 128.

Chen, Rui and Brian Stimpson, 1993, Indirect Tension Tests on Rock - Analytical/Numerical Correction for Material Bimodularity, Geotechnical Testing Journal, Vol 16, No. 2, pp. 238 – 245.

Chen, S., Z.Q. Yue, L.G. Tham, and P.K.K. Lee, 2004, Modeling of the indirect tensile test for inhomogeneous granite using a digital image-based numerical method, Paper 2B 01 – SINOROCK 2004 Symposium, *Int. J. Rock Mech. Min. Sci.* Vol. 41, No. 3, CD-ROM.

Claesson, J. and B. Bohloli, 2002, Brazilian test: stress field and tensile strength of anisotropic rocks using an analytical solution, *Int. J. Rock Mech. Min. Sci.,* Vol. 39, pp. 991 – 1004.

Clark, N.N., 1986, Three Techniques for Implementing Digital Fractal Analysis of Particle Shape, Powder Technology, Vol. 46, pp. 45 – 52.

Coker, E.G., L.N.G. Filon, 1957, A Treatise on Photo-Elasticity, Revised by H.T. Jessop, Cambridge at the University Press.

Colback, P.S.B., An analysis of brittle fracture initiation and propagation in the Brazilian test, Proc. First Congress International Society of Rock Mechanics, Vol. 1, pp. 385 – 391.

Cooper, Duane H., 1969, Hertzian Contact-Stress Deformation Coefficients, Journal of Applied Mechanics, Transactions of the ASME, Vol. 36, Series E, Number 2, June, pp. 296 – 303.

Costin, Laurence S., 1967, Time-Dependent Deformation and Failure, Ch. 5, pp. 167-215, Fracture Mechanics of Rock, Barry Kean Atkinson, Editor, Academic Press, London.

Costin, L.S. and D.H. Holcomb, 1981, Time-Dependent Failure of Rocks Under Cyclic Loading, *Tectonophysics,* Vol. 79, pp. 279-296.

Cristescu, N.D. and U. Hunsche, 1998, Time effects in rock mechanics, Wiley, Chichester; New York.

Cristescu, N.D., H.R. Hardy, Jr., and R.O. Simionescu, Editors, 2002, Basic and applied salt mechanics: proceedings of the fifth Conference on Mechanical Behavior of Salt, MECASALT V, Bucharest, Romania, 1999, A.A. Balkema Publishers, Lisse (The Netherlands).

Cruden, D.M., 1970, A theory of Brittle Creep in Rock under Uniaxial Comprssion, Journal of Geophysical Research, Vol. 75, No. 17, June, pp. 3431-42.

Cruden, D.M., 1971a, The Form of the Creep Law for Rock Under Uniaxial Compression, Int. J. Rock Mech. Min.Sc., Vol. 8, pp. 105-126.

Cruden, D.M., 1971b, Single-Increment Creep Experiments on Rock Under Uniaxial Compression, Int. J. Rock Mech. Min.Sc., Vol. 8, pp. 127-142.

Cruden, D.M., 1974, The Static Fatigue of Brittle Rock Under Uniaxial Compression, Int. J. Rock Mech. Min. Sci. & Geomech. Abstr., Vol. 11, pp. 67-73.

Cruden, D.M., 1983, Creep in brittle rock after an increment of uniaxial load, Canadian Geotechnical Journal, Vol. 20, pp. 836-839.

Cruden, D.M., 1987, Discussion of Lajtai and Schmidtke, 1986, Rock Mechanics and Rock Engineering, Vol. 20, pp. 87-88.

Dickin, E.A., 1973, Influence of Grain Shape and Size upon the Limiting Porosities of Sands, pp. 113 – 120, Evaluation of Relative Density and Its Role in Geotechnical Projects Involving Cohesionless Soils, ASTM STP 523, American Society for Testing and Materials, Philadelphia, Pa.

Dowdeswell, Julian A., 1982, Scanning Electron Micrographs of Quartz Sand Grains From Cold Environments Examined Using Fourier Shape Analysis, Journal of Sedimentary Petrology, Vol. 52, No. 4, December, pp. 1315 – 1323.

Dreyer, W., 1972, The Science of Rock Mechanics, Trans Tech Publications, Bay Village, Ohio.

Dreyer, W., 1982, Underground Storage of Oil and Gas in Salt Deposits and other Non-Hard Rocks, Halsted Press, New York.

Eerola, M. and M. Ylosjoki, 1970, The effect of particle shape on the friction angle of coarse-grained aggregates, Vol. 1, pp. 445-456, First international congress of the International Association of Engineering Geology, Paris, France.

Ehrlich, Robert and Bernhard Weinberg, 1970, An exact method for characterization of grain shape, Journal of Sedimentary Petrology, Vol. 40, No. 1, pp. 205 – 212.

Exadaktylos, G.E. and K.N. Kaklis, 2001, Applications of an explicit solution for the transversely isotropic disc compressed diametrically, *Int. J. Rock Mech. Min. Sci.,* Vol. 38, pp. 227 – 243.

Fairhurst, C., 1964, On the validity of the "Brazilian" test for brittle materials, *Int. J. Rock Mech. Mining Sci.,* Vol. 1, pp. 535-546.

Ferreira, P.J., M.G. Rasteiro, and M.M. Figueiredo, 1993, Influence of Shape on Particle Size Analysis, Particulate Science and Technology, Vol. 11, pp. 199 – 206.

Franklin, J.A., J.M. Kemeny, and K.K. Girdner, 1996, Evolution of measuring systems: a review, pp. 47 – 52, Measurement of Blast Fragmentation, Proceedings of the Fragblast-5 Workshop on Measurement of Blast Fragmentation, Montreal, Quebec, Canada, August 1996, A.A. Balkema, Rotterdam/Brookfield.

Gramberg, J., 1965, Axial Cleavage Fracturing, a Significant Process in Mining and Geology, Engineering Geology, Vol. 1, No. 1, pp. 31-72.

Gramberg, J., 1989, A Non-Conventional View on Rock Mechanics and Fracture Mechanics, Published for the Commission of the European Communities by A.A. Balkema/Rotterdam/Brookfield.

Hertz, Heinrich, 1881, Ueber die Berűhrung fester elastischer Kőrper (On the contact between solid elastic bodies), Journal fuer die reine und angewandte Mathematik, Vol. 92, pp. 156-171.

Hills, D.A., D. Nowell, and A. Sackfield, 1993, Mechanics of elastic contacts, Butterworth-Heinemann Ltd., Oxford.

Hiramatsu, Yoshio, and Oka, Yukitoshi, 1970, Disc Test, Ring Test, Rectangular Plate Test and Irregular Specimen Test for Determining the Tensile Strength of Rocks, Paper 3-29, pp. 199-206, Vol. II, Proceedings of the Second Congress of the International Society for Rock Mechanics, Beograd, Jugoslavia.

Hoek, E., and E.T. Brown, 1980, Underground Excavations in Rock, The Institution of Mining and Metallurgy, London.

Hogg, R., M.L. Turek, and E. Kaya, 2004, The Role of Particle Shape in Size Analysis and the Evaluation of Comminution Processes, Particulate Science and Technology, Vol. 22, pp. 355 – 366.

Holubec, I. and E. D'Appolonia, 1973, Effect of Particle Shape on the Engineering Properties of Granular Soils, pp. 304 – 318, Evaluation of Relative Density and Its Role in Geotechnical Engineering Involving Cohesionless Soils, ASTM STP 523, American Society for Testing and Materials, Philadelphia, Pa.

Hondros, G., 1959, The Evaluation of Poisson's Ratio and the Modulus of Materials of a Low Tensile Resistance by the Brazilian (Indirect Tensile) Test with Particular Reference to Concrete, Australian Journal of Applied Science, Vol. 10, pp. 243 – 268.

Hooper, J.A., 1971, The Failure of Glass Cylinders in Diametral Compression, J. Mech. Phys. Solids, Vol. 19, pp. 179 – 200.

Hudson, J.A. and E.T. Brown, 1973, Studying Time-Dependent Effects in Failed Rock, pp. 25-34, Proceedings, New Horizons in Rock Mechanics, Proceedings, Fourteenth Symposium on Rock Mechanics, ASCE, New York.

Hudson, J.A.., E.T. Brown, and F. Rummel, 1972, The controlled failure of rock discs and rings loaded in diametrical compression, *Int. J. Rock Mech. Min. Sci.,* Vol. 9, pp. 241-248.

Hudyma, Nick, 2001, Influence of Lithophysal Porosity on Stress-Strain Properties of Topopah Spring Tuff – Numerical Analysis, Document MOD-01-003 Revision 0, http://hrc.nevada.edu/QA/Report/MOD-01-003.pdf.

Hudyma, N., B. Avar, and M. Karakouzian, 2004, Compressive strength and failure modes of lithophysae-rich Topopah Spring Tuff specimens and analog models containing cavities, Engineering Geology, Vol. 73, pp. 179-190.

Hundal, H.S., S. Rohani, H.C. Wood, and M.N. Pons, 1997, Particle shape characterization using image analysis and neural networks, Powder Technology, Vol. 91, pp. 217 – 227.

Jaeger, J.C. and N.G.W. Cook, 1979, Fundamentals of Rock Mechanics, A Halsted Press Book, Chapman and Hall, London.

Jakus, K., D.C. Coyne, and J.E. Ritter, Jr., 1978, Analysis of fatigue data for lifetime predictions for ceramic materials, Journal of Materials Science, Vol. 13, pp. 2071 – 2080.

Kaiser, P.K. and N.R. Morgenstern, Phenomenological Model for Rock with Time-Dependent Strength, pp. 153 – 165, Int. J. Rock Mech. Min. Sci. & Geomech. Abstr., Vol. 18.

Kawamoto, Toshikazy and Toshiaki Saito, 1974, The Behavior of Rock-Like Materials in some controlled strain rates, pp. 161 – 166, Vol. II, Part A, Advances in Rock Mechanics, Reports of Current Research, Proceedings of the Third Congress of the International Society for Rock Mechanics, Denver, CO, National Academy of Sciences, Washington, D.C.

Kie, Tan Tjong, 1993, The Importance of Creep and Time-dependent Dilatancy, as Revealed from Case Records in China, Chapter 31, pp. 709 – 744, Comprehensive Rock

Engineering, John A. Hudson, Editor-in-Chief, Vol. 3, Rock Testing and Site Characterization, John A. Hudson, Volume Editor, Pergamon Press, Oxford.

Kranz, Robert L., 1979, Crack Growth and Development During Creep of Barre Granite, Int. J. Rock mech. Min. Sci. & Geomech. Abstr., Vol. 16, pp. 23-35.

Kranz, Robert L., 1980, The Effects of Confining Pressure and Stress Difference on Static Fatigue of Granite, Journal of Geophysical Research, Vol. 85, No. B4, April 10, pp. 1854-1866.

Krumbein, W.C., 1941, Measurement and Geological Significance of Shape and Roundness of Sedimentary Particles, Journal of Sedimentary Petrology, Vol. 11, No. 2, pp. 64 – 72.

Krumbein, W.C., and L.L. Sloss, 1963, Stratigraphy and Sedimentation, Second Edition, W.H. Freeman and Company, San Francisco.

Kwan, A.K.H., C.F. Mora, and H.C. Chan, 1999, Particle shape analysis of coarse aggregate using digital image processing, Cement and Concrete Research, Vol. 29, pp. 1403 - 1410.

Lajtai, E.Z. and L.P. Bielus, 1986, Stres Corrosion Cracking of Lac du Bonnet Granite in Tension and Compression, Rock Mechanics and Rock Engineering, Vol. 19, pp. 71-87.

Lajtai, E.Z. and R.H. Schmidtke, 1986, Delayed Failure in Rock Loaded in Uniaxial Compression, Rock Mechanics and Rock Engineering, Vol. 19, pp. 11-25.

Lajtai, E.Z. and R.H. Schmidtke, 1987, Authors' Reply to Cruden, 1987, Rock Mechanics and Rock Engineering, Vol. 20, pp. 88-89.

Lubkin, J.L., 1962, Contact Problems, Ch. 42, Handbook of Engineering Mechanics, W. Flűgge, Editor, McGraw-Hill Book Company, Inc., New York.

Ma, Lumin, 2004, Experimental Investigation of Time Dependent Behavior of Welded Topopah Spring Tuff, Ph.D. Dissertation, Geo-Engineering, University of Nevada, Reno.

Ma, L. and J. Daemen, 2004, Time Dependent Mechanical Behavior of Welded Tuff, Part 2, Final Technical Report, Prepared for U.S. DOE/UCCSN Cooperative Agreement DE-FC28-98NV12081, Document ID: TR-03-018, University of Nevada, Reno. <http://hrcweb.nevada.edu/QA/Report/TR-03-018-2.pdf>

MacLeod, N., 2002, Geometric morphometrics and geological shape-classification systems, Earth-Science Reviews, Vol. 59, pp. 27 – 47.

Maerz, Norbert H., 2004, Technical and Computational Aspects of the Measurement of Aggregate Shape by Digital Image Analysis, journal of Computing in Civil Engineering, Vol. 18, No.1, January 1, pp. 10 – 18.

Martin, R.J., J.S. Noel, P.J. Boyd, and R.H. Price, 1997, Creep and Static Fatigue of Welded tuff from Yucca Mountain, Nevada, Int. J. Rock Mech. & Min. Sci., Vol. 34, No. 3-4, Paper No. 190.

Martin, R.J., III, R.H. Price, P.J. Boyd, and J.S. Noel, 1993, The Influence of Strain Rate and Sample Inhomogeneity on the Moduli and Strength of Welded Tuff, pp. 1507-1510, Int. J. Rock Mech. Min. Sci. & Geomech. Abstr., Vol. 30, No. 7.

Mellor, Malcolm, and Ivor Hawkes, 1971, Measurement of Tensile Strength by Diametral Compression of Discs and Annuli, Engineering Geology, Vol. 5, pp. 173-225.

Meloy, T.P., 1977, Fast Fourier Transforms Applied to Shape Analysis of Particle Silhouettes to obtain Morphological Data, Powder Technology, Vl. 17, pp. 27 – 35.

Meloy Thomas P. and Nigel N. Clark, 1986, Fourier Analysis: A computer based approach for particle shape characterization, Proceedings of the Third Conference on the Use of Computers in the Coal Industry, Morgantown, WV, July 1986, Y.J. Wang, R.Larry Grayson, and Richard L. Sanford, Editors, A.A. Balkema, Rotterdam/Boston.

Mirza, M. Waseem, Richard A. Graul, Jonathan L. Groeger, and Aramis Lopez, 1997, Theoretical Evaluation of Poisson's Ratio and Elastic Modulus Using Indirect Tensile Test with Emphasis on Bituminous Mixtures, Transportation Research Record No. 1590, pp. 34 – 44, Transportation Research Board, National Academy Press, Washington, D.C.

Muskhelishvili, N.I., 1963, Some basic problems of the mathematical theory of elasticity, P. Noordhoff, Groningen, The Netherlands.

Novak, J.W. Jr., and J.R. Thompson, 1986, Extending the Use of Particle Sizing Instrumentation to Calculate Particle Shape Factors, Powder Technology, Vol. 45, pp. 159 – 167.

Olsson, W.A., 1991, Compressive strength of tuff as a function of strain rate from 10^{-6} to 10^{3} /sec, International Journal of Rock Mechanics and Minng Sciencess & Geomechanics Abstracts, Vol. 28, No. 1, January, pp. 115 – 118.

Pan, Y.-W., and B.-H. Wen, 2001, Constitutive model for the continuous damage of brittle rock, Géotechnique, Vol. LI, No. 2, pp. 155 – 159.

Podczeck, Fridrun, 1997, A shape factor to assess the shape of particles using image analysis, Powder Technology, Vol. 93, pp. 47 – 53.

Price, Neville J., 1966, Fault and Joint Development in Brittle and Semi-Brittle Rock, Pergamon Press, Oxford.

Price, R.H., and S.J. Bauer, 1985, Analysis of the elastic and strength properties of Yucca Mountain tuff, Nevada, pp. 89 – 96, Vol. 1, Research & Engineering Applications in Rock Masses, Proceedings of the 26th U.S. Symposium on Rock Mechanics, South Dakota School of Mines & Technology, June 1985, Eileen Ashworth, Editor, A.A. Balkema/Rotterdam/Boston.

Price, R.H., P.J. Boyd, J.S. Noel & R.J. Martin III, 1994, Relationship between static and dynamic rock properties in welded and nonwelded tuff, pp. 505 – 512, Rock Mechanics Models and Measurements Challenges from Industry, Proceedings of the 1st North American Rock Mechanics Symposium, The University of Texas at Austin, June 1994, Priscilla P. Nelson and Stephen E. Laubach, Editors, A.A. Balkema/Rotterdam/Brookfield.

Primel, Luis and Claude Tourenq, Editors, 2000, Aggregates, A.A. Balkema, Rotterdam/Brookfield.

Ray, S.K., M. Sarkar, and T.N. Singh, 1999, Effect of cyclic loading and strain rate on the mechanical behavior of sandstone, pp. 543-549, Int. Journal of Rock Mechanics and Mining Sciences, Vol. 36.

Rittenhouse, Gordon, 1943, A Visual Method of Estimating Two-Dimensional Sphericity, Journal of Sedimentary Petrology, Vol. 13, No. 2, pp. 79-81.

Rosen, Howard N., and Hugh M. Hulburt, 1970, Size Analysis of Irregular Shaped Particles in Sieving, Ind. Eng. Chem. Fundam., Vol. 9, No. 4, pp. 658 – 661.

Rudnick, A., A.R. Hunter, and F.C. Holden, 1963, An Analysis of the Diametral-Compression Test, Materials research and standards, Vol. 3, Issue 4, April, pp. 283-289.

Saada, Adel S., 1993, Elasticity Theory and Applications , Second Edition, Krieger Publishing Company, Malabar, Florida.

Sayles, R.S., G.M.S. deSilva, J.A. Leather, J.C. Anderson and P.B. Macpherson, 1981, Elastic conformity in Hertzian contacts, Tribology international, Vol. 14, Issue 6, December, pp. 315-322.

Schmidtke, R.H. and E.Z. Lajtai, 1985, The Long-Term Strength of Lac du Bonnet Granite, Int. J. Rock Mech. Min. Sci. & Geomech. Abstr., Vol. 22, No. 6, pp. 461-465.

Schwartz, Jeremy and Edward Y. Harper, 1971, On the relative approach of two-dimensional elastic bodies in contact, Int. J. Solids Structures, vol. 7, pp. 1613-1626.

Schwarz, H. and H.E. Exner, 1980, The Implementation of the Concept of Fractal Dimension on a Semi-Automatic Image Analyser, Powder Technology, vol. 27, pp. 207 – 213.

Shigley, Joseph Edward, 1986, Mechanical Engineering Design, Mc-Graw-Hill Book Company, New York.

Singh, D.P., V.R. Sastry & P. Srinivas, 1989, Effect of strain rae on mechanical behaviour of rocks, pp. 109 – 114, Rock at Great Depth, Proceedings, V. Maury & D. Fourmaintraux, Editors, A.A. Balkema/Rotterdam/Brookfield.

Smith, M.R. and L. Collis, Editors, 1993, Aggregates Sand, gravel and crushed rock aggregates for construction purposes, Second Edition, The Geological Society of London.

Smith, M.R., and L. Collis, Editors, 2001, Aggregates Sand, gravel and crushed rock aggregates for construction purposes, Third Edition, The Geological Society of London.

Sun, J., and Y.Y. Hu, 1997, Time-dependent Effect on the Tensile Strength of Saturated Granite at Three Gorges Project in China, Int. J. Rock Mech. Min. Sci., Vol. 34, No. ¾, p. 381, paper no. 306.

Thomas, M.C., R.J. Wiltshire, and A.T. Williams, 1995, The use of Fourier descriptors in the classification of particle shape, Sedimentology, Vol. 42, pp. 635 – 645.

Timoshenko, S., and J.N. Goodier, 1970, Theory of Elasticity, McGraw-Hill, New York.

Vallejo, L.E., 1995, Fractal analysis of granular materials, Géotechnique, Vol. 45, No. 1, pp. 159-163.

Vallerga, B.A., H.B. Seed, C.L. Monismith, and R.S. Cooper, 1957, Effect of Shape, Size, and Surface Roughness of Aggregate Particles on the Strength of Granular Materials, pp. 63 – 74, Road and Paving Materials, ASTM Special Publication No. 212, American Society for Testing Materials, Philadelphia, Pa.

Vardar, Ö. and I. Finnie, 1975, An analysis of the Brazilian disk fracture test using the Weibull probabilistic treatment of brittle strength, Int. Jnl. of Fracture, Vol. 11, No.3, June, pp. 495 – 508.

Wadell, Hakon, 1933, Sphericity and Roundness of Rock Particles, The Journal of Geology, Vol. LXI, No. 3, pp. 310 – 331.

Wawersik, W.R., 1972, Time-Dependent Rock Behavior in Uniaxial Compression, pp. 85-106, New Horizons in Rock Mechanics, Proceedings, Fourteenth Symposium on Rock Mechanics, held at The Pennsylvania State University, University park, Pennsylvania, H.R. Hardy, Jr. and R. Stefanko, Editors, published by American Society of Civil Engineers, New York, N.Y., 1973.

Wettimuny, Ramitha and Dayakar Penumadu, 2004, Application of Fourier Analysis to Digital Imaging for Particle Shape Analysis, Journal of Computing in Civil Engineering, Vol. 18, No.1, January 1, pp. 2 – 9.

Wu, H. and D.D. Pollard, 1993, Effect of Strain Rate on a Set of Fractures, Int. J. Rock Mech. Min. Sci. & Geomech. Abstr., Vol. 30, No. 7, pp. 869-872.

Yegulalp, T.M., and K. Kim, 1993, Statistical assessment of scale effect on rock properties using the theory of extremes, Transactions of Society of Mining, Metallurgy, and Exploration, Inc., Vol. 294, pp. 1834 – 1837.

Appendix 1- Triaxial Testing

1.1 Summary of Results

Table 1.1 Source Information of Specimens for Triaxial Tests

Specimen ID	Borehole	Depth (ft)	Length (mm)	Diameter (mm)	Weight (g)	Density (g/cm^3)	Moisture Content (%)	Confining Pressure (MPa)
01026149-1-T	ESF-HD-CHE-8	82.9-83.5	138.18	60.96	907	2.25	0.66	10
01026154-1-T	ESF-HD-CHE-8	108.7-109.4	137.67	60.96	910	2.26	0.77	5
01026155-4-T	ESF-HD-CHE-8	109.4-110.2	135.89	60.96	902	2.27	0.67	5
01026157-3-T	ESF-HD-CHE-8	123.2-123.9	137.41	60.96	911.5	2.27	0.71	5
01026158-2-T	ESF-HD-CHE-8	126.6-127.5	136.91	60.96	907	2.27	0.72	10
01026160-1-T	ESF-HD-CHE-8	130.2-131.2	134.87	60.96	892	2.27	0.73	20
01026160-2-T	ESF-HD-CHE-8	130.2-131.2	132.08	60.96	870	2.26	0.8	10
01026237-T	ESF-HD-WH-45	19.0-19.4	129.54	60.96	861	2.28	0.58	10
01026246-1-T	ESF-HD-WH-46	21.5-22.4	138.43	60.96	925	2.29	0.65	10
01026248-4-T	ESF-HD-WH-47	2.5-3.3	135.64	60.71	878	2.24	0.85	20
01026250-2-T	ESF-HD-WH-47	5.1-6.0	136.14	60.96	907	2.28	0.83	10
01026257-1-T	ESF-HD-WH-41	10.1-11.1	130.56	60.96	861.5	2.26	0.81	20
01026259-1-T	ESF-HD-WH-41	15.9-16.4	135.13	60.86	895	2.28	0.67	5
01026543-1-T	ESF-HD-CHE-8	18.1-18.8	151.13	60.71	980.5	2.24	0.76	20
01026174-1-T	UE-25 UZ #16	1075.6-1076.1	117.09	60.09	794.5	2.39	0.5	5
01026241-1-T	ESF-HD-WH-46	2.8-3.4	113.54	60.85	737	2.23	0.88	5
01026145-1-T	ESF-HD-CHE-8	31.6-32.8	137.92	60.96	906.5	2.25	0.55	10
01026146-1-T	ESF-HD-CHE-8	47.6-48.5	134.62	60.71	874	2.24	0.63	20
01026255-1-T	ESF-HD-WH-41	8.8-9.5	136.40	60.96	909.5	2.28	0.88	20
01026258-4-T	ESF-HD-WH-41	12.9-14.0	132.59	60.83	877.5	2.28	0.68	5
01026153-1-T	ESF-HD-CHE-8	107.9-108.5	132.84	60.96	882.5	2.28	0.62	5
01026144-1-T	ESF-HD-CHE-8	29.9-30.7	138.87	60.86	890.5	2.20	0.56	10
01026253-1-T	ESF-HD-WH-47	29.1-29.9	137.67	60.8	897.5	2.25	0.67	20
01026145-2-T	ESF-HD-CHE-4	31.6-32.8	131.57	60.96	869	2.26	0.58	20
01026541-2-T	ESF-HD-CHE-5	3.3-3.8	126.75	60.96	825.5	2.23	0.06	5
01026225-6-T	ESF-HD-WH-42	19.8-20.8	124.46	60.96	828.5	2.28	1.33	10
01026227-2-T	ESF-HD-WH-43	6.2-7.9	113.03	60.75	747	2.28	0.8	10
01026226-1-T	ESF-HD-WH-42	24.5-25.0	118.36	60.88	787	2.28	0.89	5
01026229-2-T	ESF-HD-WH-43	12.0-12.7	123.70	60.75	817.5	2.28	0.86	20
01026227-1-T	ESF-HD-WH-44	6.2-7.9	127.25	60.66	851	2.31	0.82	20
Note: All the specimens except 01026174-1-T (from Tptpln, borehole UE25 UZ#16) were from Tptpmn.								

Table 1.2 Results of Triaxial Tests

Specimen ID	Confining Stress (MPa)	Displacement Rate (mm/min)	Axial Stress at Failure (MPa)	Stress Rate (MPa/s)	Young's Modulus (GPa)	Poisson's Ratio	Axial Strain at Failure (mm/mm)	Lateral Stain at Failure (mm/mm)
01026149-1-T	10	0.16	349.65	0.3709	NA	NA	NA	NA
01026154-1-T	5	0.16	245.59	0.3589	NA	NA	NA	NA
01026155-4-T	5	0.16	309.54	0.3882	NA	NA	NA	NA
01026157-3-T	5	0.016	291.97	0.0372	NA	NA	NA	NA
01026158-2-T	10	0.0016	342.99	0.0037	NA	NA	NA	NA
01026160-1-T	20	0.16	386.53	0.3741	NA	NA	NA	NA
01026160-2-T	10	0.16	303.57	0.3727	NA	NA	NA	NA
01026237-T	10	0.016	192.32	0.0378	NA	NA	NA	NA
01026246-1-T	10	0.0016	343.18	0.0038	NA	NA	NA	NA
01026248-4-T	20	0.16	263.32	0.3492	NA	NA	NA	NA
01026250-2-T	10	0.016	346.93	0.0365	NA	NA	NA	NA
01026257-1-T	20	0.016	322.84	0.0359	NA	NA	NA	NA
01026259-1-T	5	0.016	263.58	0.0371	NA	NA	NA	NA
01026543-1-T	20	0.016	303.15	0.0330	NA	NA	NA	NA
01026174-1-T	5	0.16	279.29	0.4382	NA	NA	NA	NA
01026241-1-T	5	0.0016	222.67	0.0035	32.06	0.19	0.0077	-0.0017
01026145-1-T	10	0.0016	297.62	0.0037	36.01	0.16	0.0088	-0.0014
01026146-1-T	20	0.0016	312.23	0.0035	31.55	0.18	0.0100	-0.0014
01026255-1-T	20	0.0016	370.88	0.0036	31.2	0.19	0.0122	-0.0023
01026258-4-T	5	0.0016	297.54	0.0038	35.6	0.19	0.0090	-0.0021
01026153-1-T	5	0.16	342.13	0.3772	34.4	0.23	0.0107	-0.0029
01026144-1-T	10	0.16	373.76	0.3743	34.89	0.23	0.0115	-0.0039
01026253-1-T	20	0.16	243.21	0.3560	28.9	0.15	0.0104	-0.0013
01026145-2-T	20	0.16	344.98	0.3952	33.77	0.19	0.0100	-0.0016
01026541-2-T	5	0.16	228.3	0.3748	35.64	0.19	0.0063	-0.0011
01026225-6-T	10	0.016	346.46	0.0375	30.74	0.19	0.0121	-0.0025
01026227-2-T	10	0.016	312.55	0.0396	33.88	0.24	0.0097	-0.0032
01026226-1-T	5	0.16	266.74	0.3647	34.33	0.17	0.0085	-0.0018
01026229-2-T	20	0.16	378.43	0.3872	33	0.18	0.0116	-0.0019
01026227-1-T	20	0.016	382.66	0.0040	37.39	0.15	0.0108	-0.0021

Note: All the specimens except 01026174-1-T (from Tptpln, borehole UE25 UZ#16) were from Tptpmn.

1.2 Force-Displacement Graphs

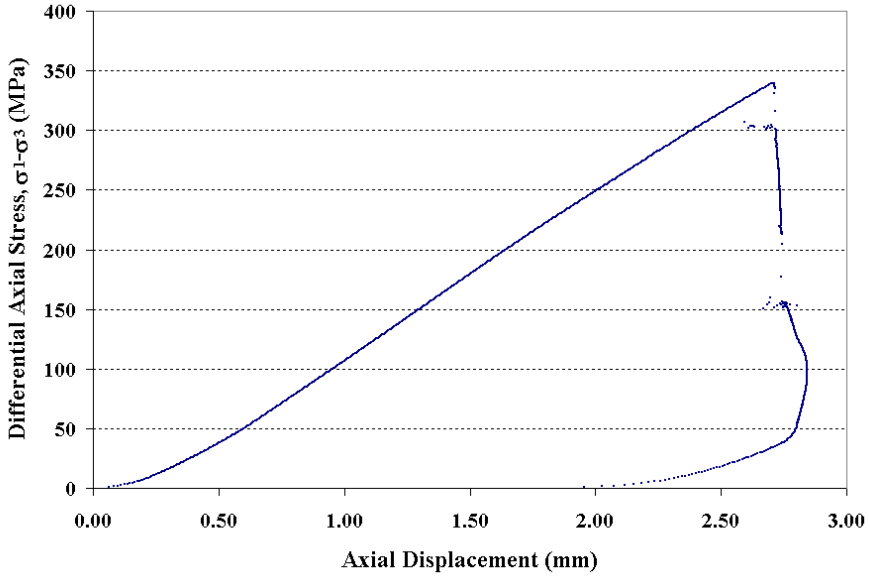

Figure 1.2.1 Axial force-axial displacement curve for Specimen 01026149-1-T, Confining pressure = 10 MPa, Axial stress at failure= 349.65 MPa, Displacement rate = 0.16 mm

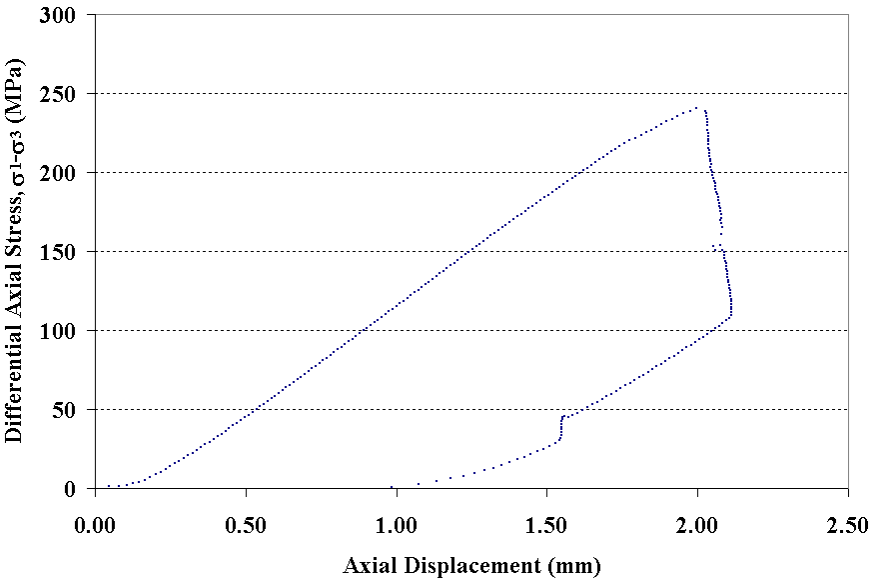

Figure 1.2.2 Axial force-axial displacement curve for specimen 01026154-1-T, Confining pressure = 5MPa, Axial stress at failure = 245.59 MPa, Displacement rate = 0.16 mm

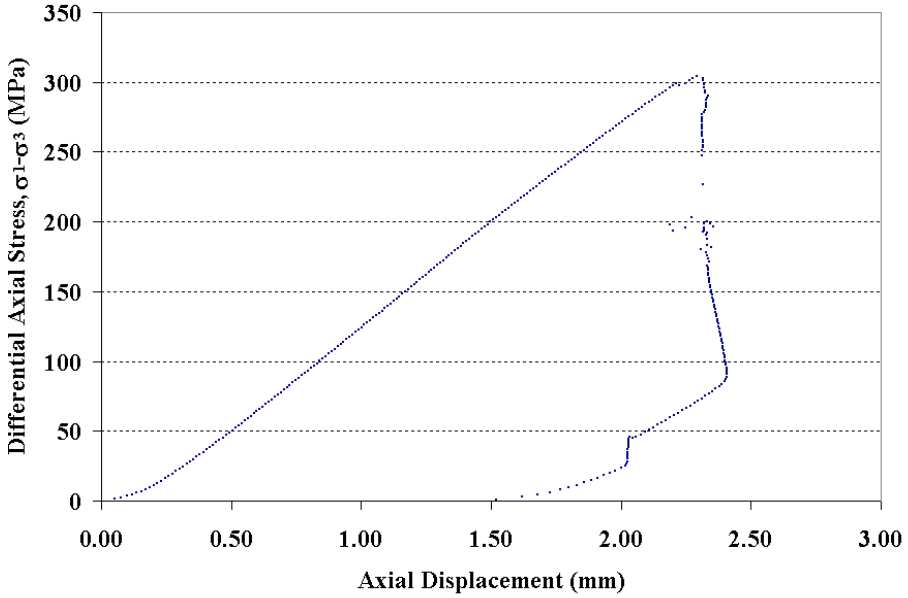

Figure 1.2.3 Axial force-axial displacement curve for specimen 01026155-4-T, Confining pressure = 5 MPa, Axial stress at failure = 309.54 MPa, Displacement rate = 0.16 mm

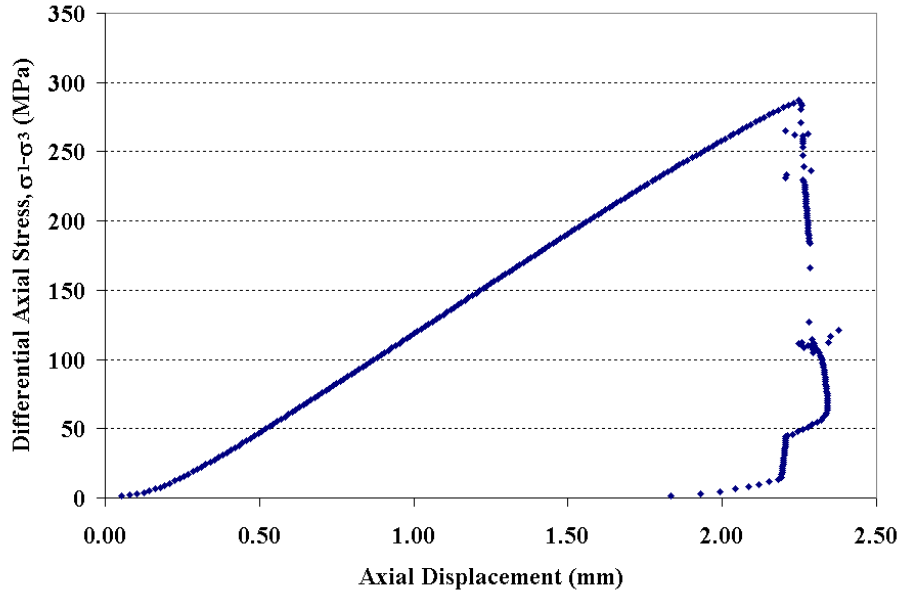

Figure 1.2.4 Axial force-axial displacement curve for specimen 01026157-3-T, Confining pressure = 5 MPa, Axial stress at failure = 291.97 MPa, Displacement rate = 0.016 mm

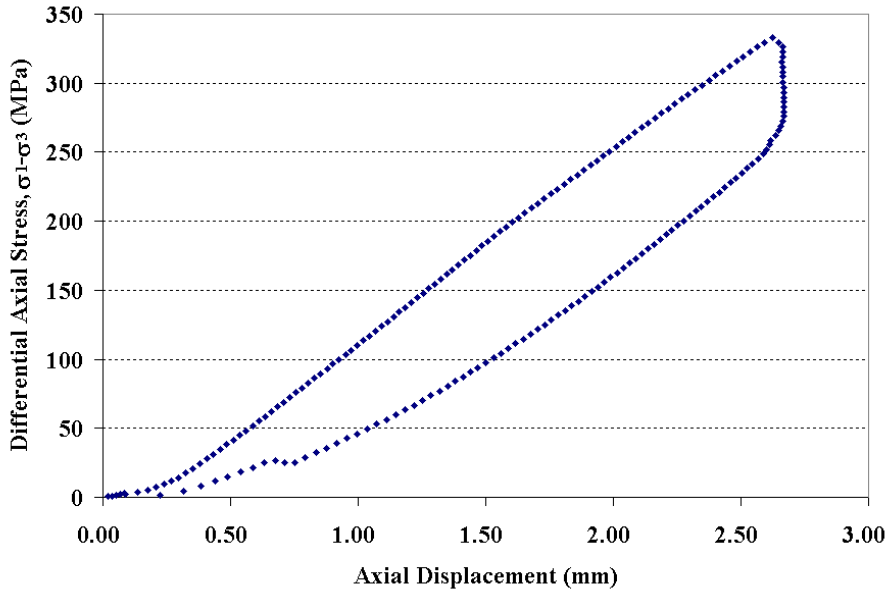

Figure 1.2.5 Axial force-axial displacement curve for specimen 01026158-2-T, Confining pressure = 10 MPa, Axial stress at failure = 342.99 MPa, Displacement rate = 0.0016 mm

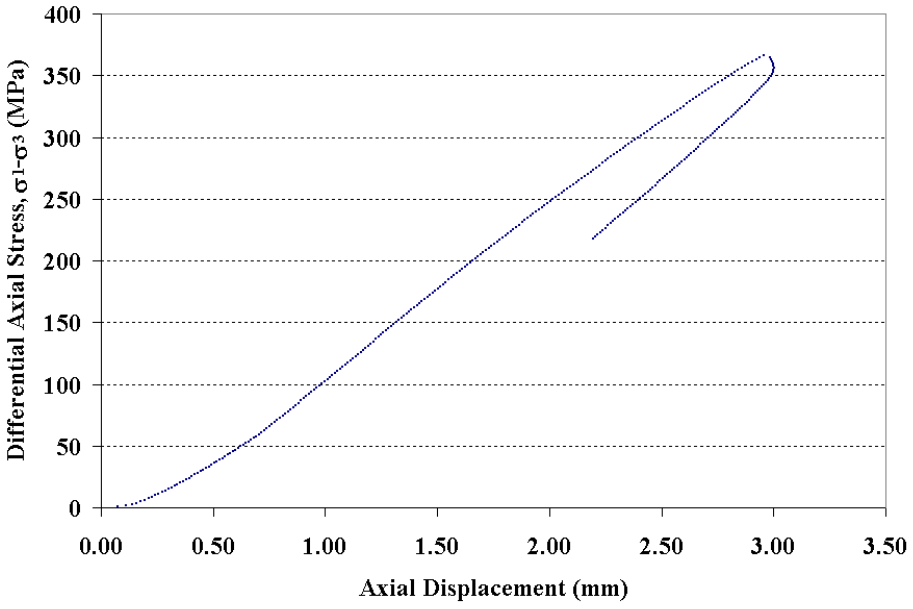

Figure 1.2.6 Axial force-axial displacement curve for specimen 01026160-1-T, Confining pressure = 20 MPa, Axial stress at failure = 386.53 MPa, Displacement rate = 0.16 mm

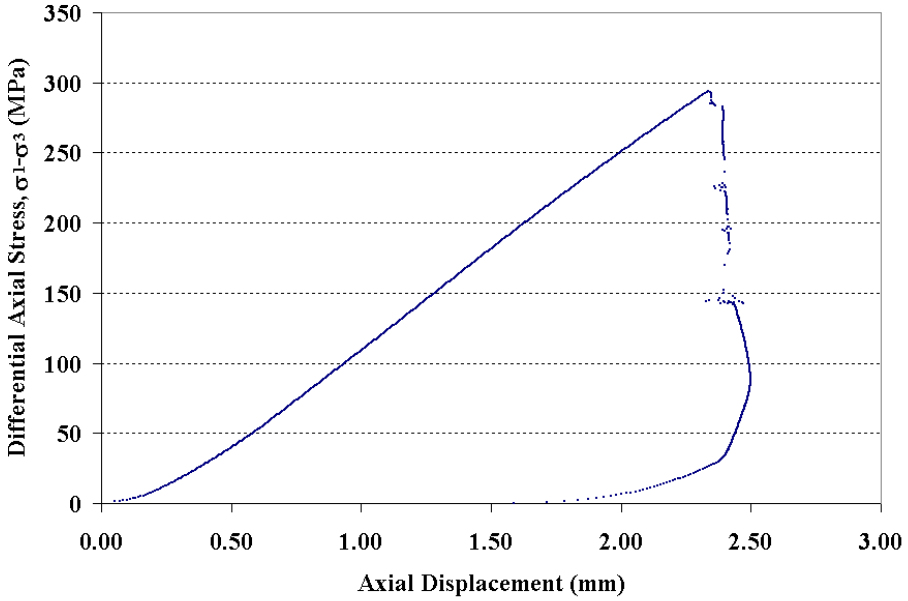

Figure 1.2.7 Axial force-axial displacement curve for specimen 01026160-2-T, Confining pressure = 10 MPa, Axial stress at failure = 303.57 MPa, Displacement rate = 0.16 mm

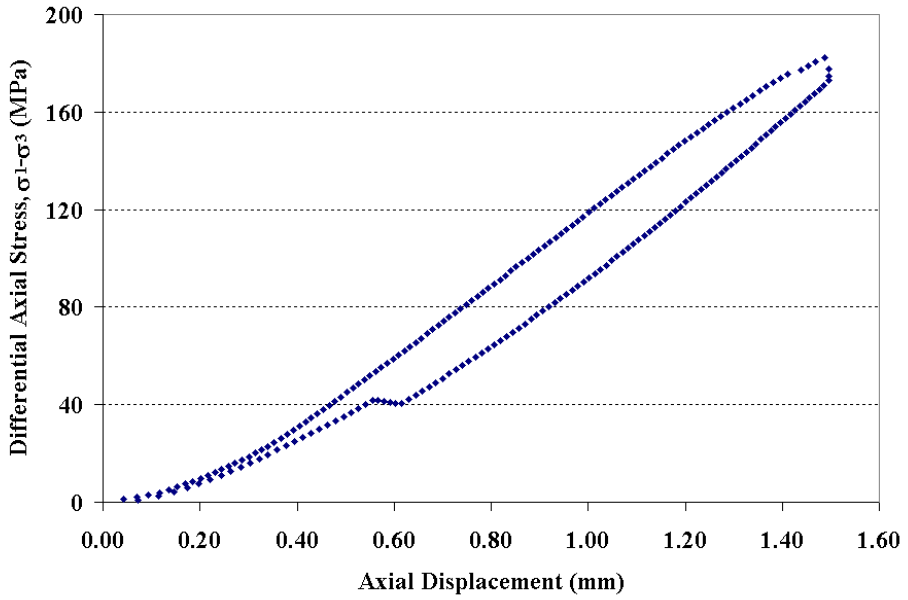

Figure 1.2.8 Axial force-axial displacement curve for specimen 01026237-T, Confining pressure = 10 MPa, Axial stress at failure = 192.32 MPa, Displacement rate = 0.016 mm

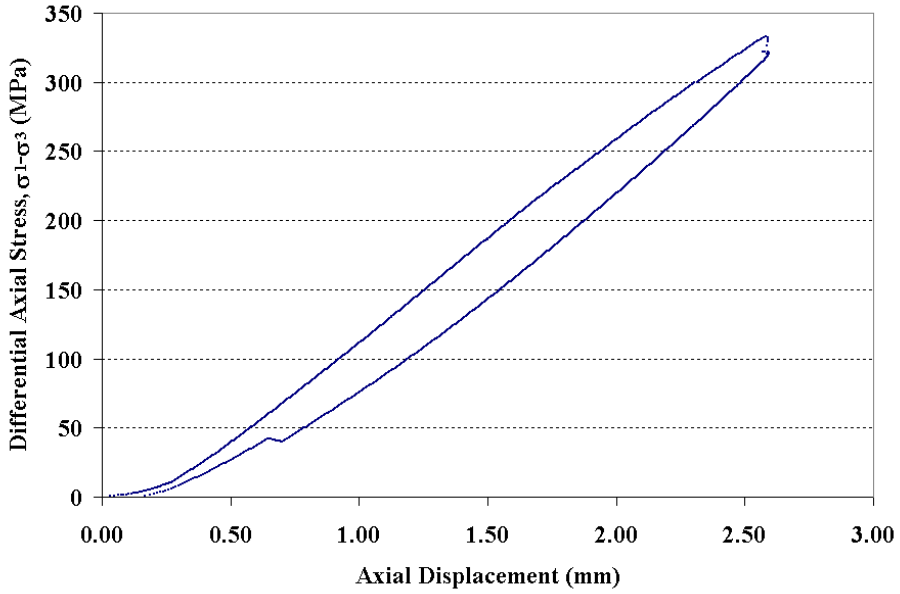

Figure 1.2.9 Axial force-axial displacement curve for specimen 01026246-1-T, Confining pressure = 10 MPa, Axial stress at failure = 343.18 MPa, Displacement rate = 0.0016 mm

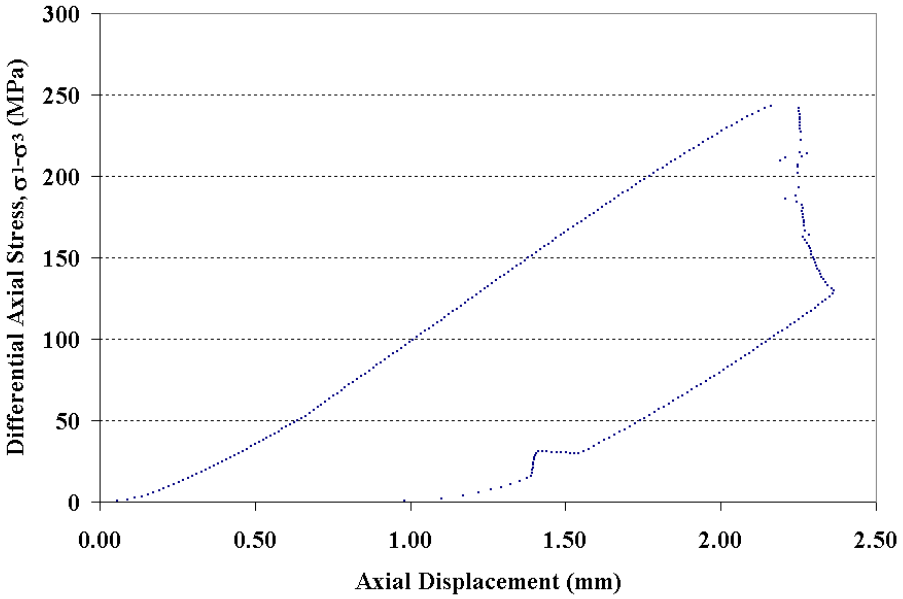

Figure 1.2.10 Axial force-axial displacement curve for specimen 01026248-4-T, Confining pressure = 20 MPa, Axial stress at failure = 263.32 MPa, Displacement rate = 0.16 mm

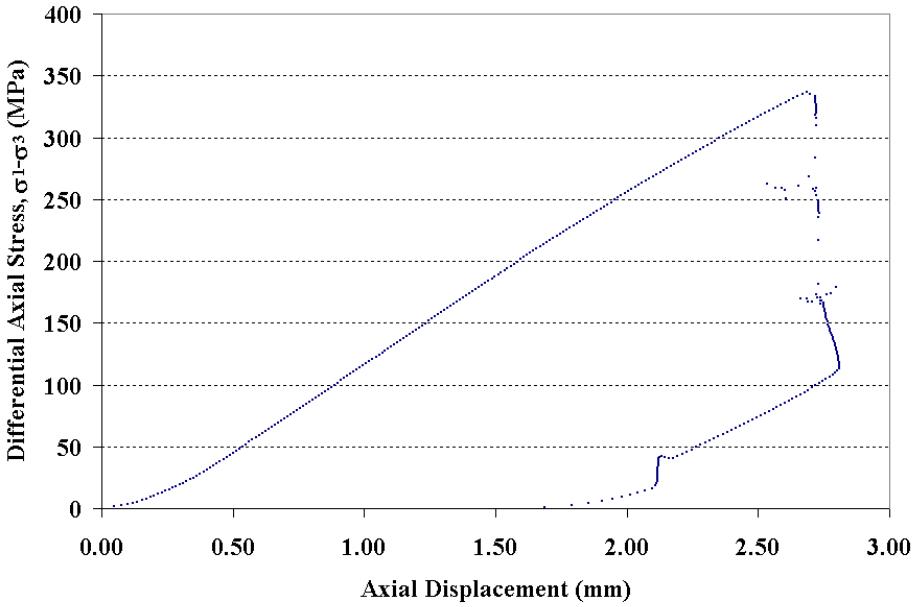

Figure 1.2.11 Axial force-axial displacement curve for specimen 01026250-2-T, Confining pressure = 10 MPa, Axial stress at failure = 346.93 MPa, Displacement rate = 0.016 mm

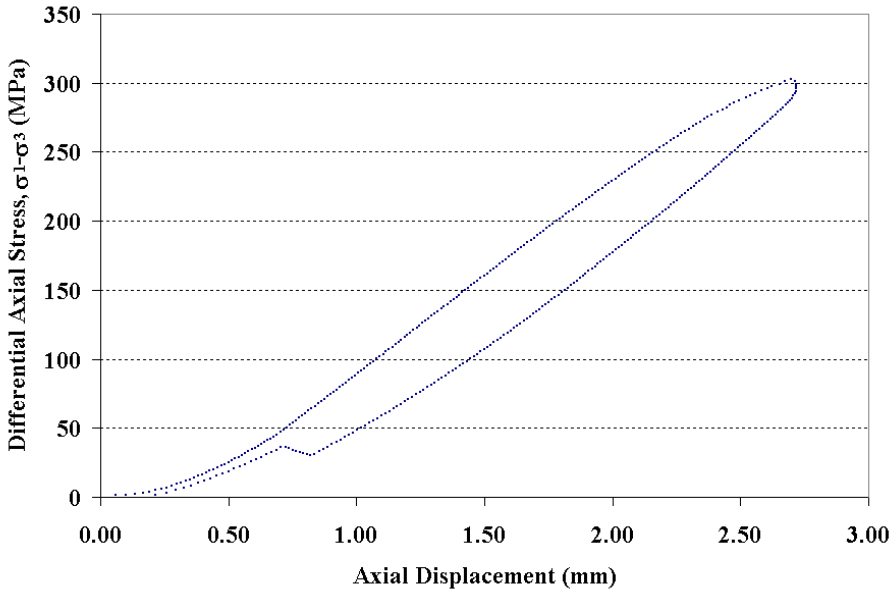

Figure 1.2.12 Axial force-axial displacement curve for specimen 01026257-1-T, Confining pressure = 20 MPa, Axial stress at failure = 322.84 MPa, Displacement rate = 0.016 mm

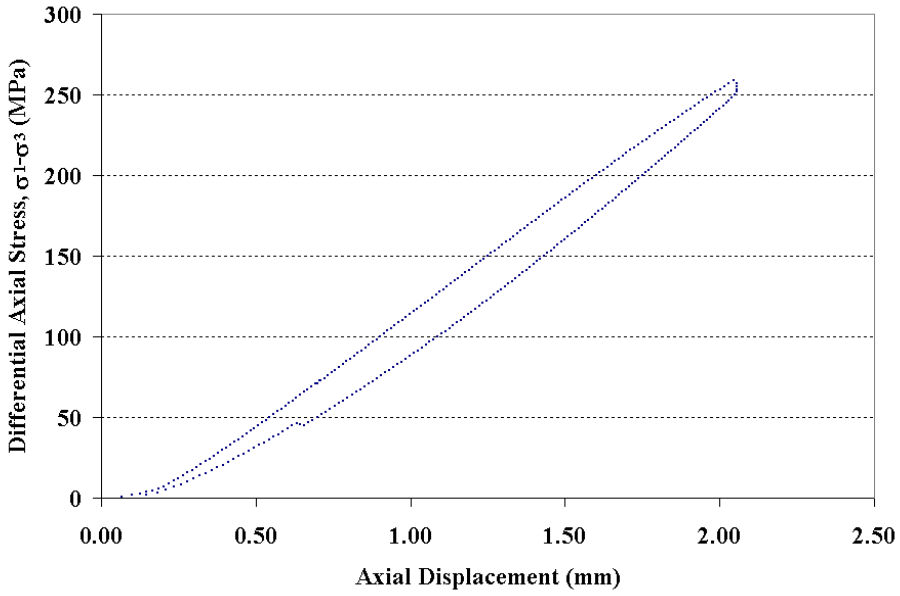

Figure 1.2.13 Axial force-axial displacement curve for specimen 01026259-1-T, Confining pressure = 5 MPa, Axial stress at failure = 263.58 MPa, Displacement rate = 0.016 mm

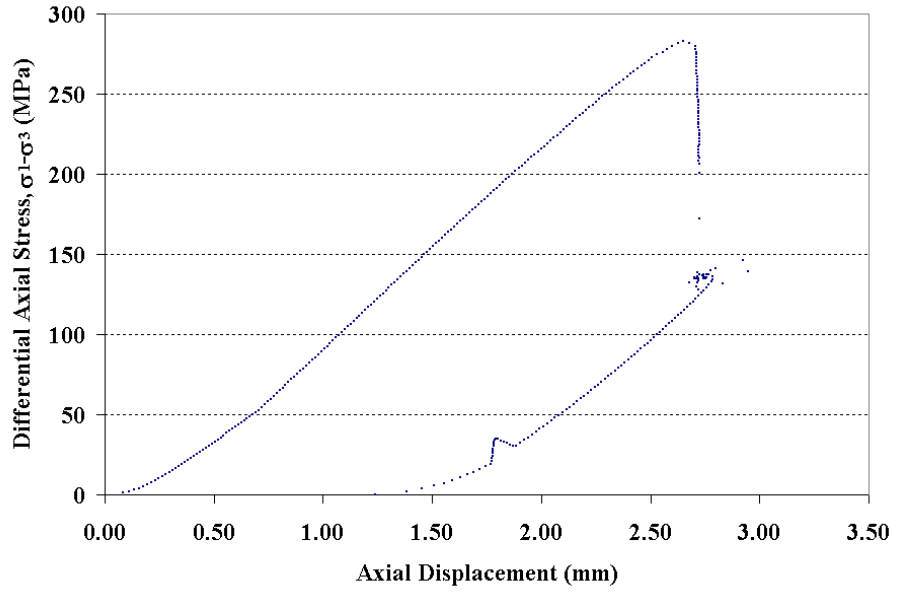

Figure 1.2.14 Axial force-axial displacement curve for specimen 01026543-1-T, Confining pressure = 20 MPa, Axial stress at failure = 303.15 MPa, Displacement rate = 0.016 mm

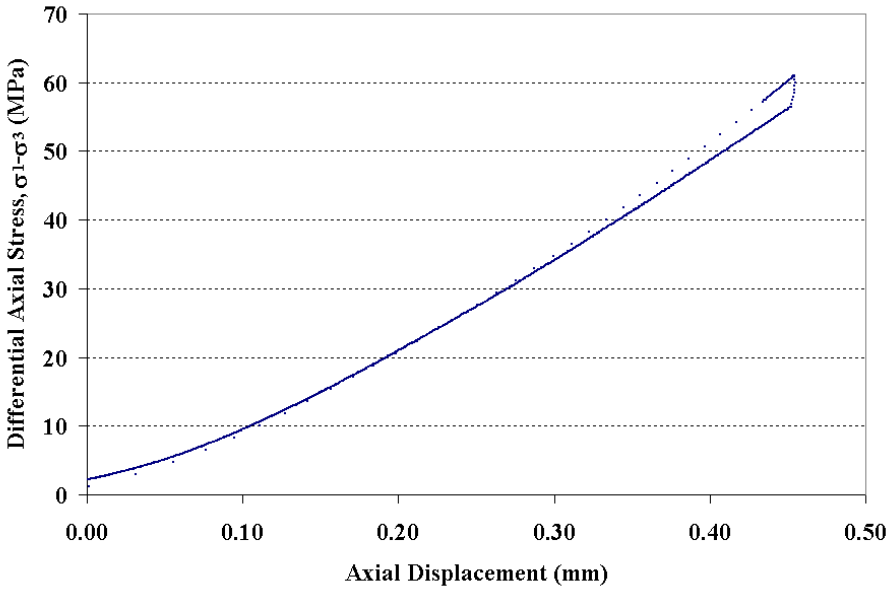

Figure 1.2.15 Axial force-axial displacement curve for specimen 01026174-1-T, Confining pressure = 5 MPa, Axial stress at failure= 279.29 MPa, Displacement rate = 0.16 mm

1.3 Stress-Strain Graphs

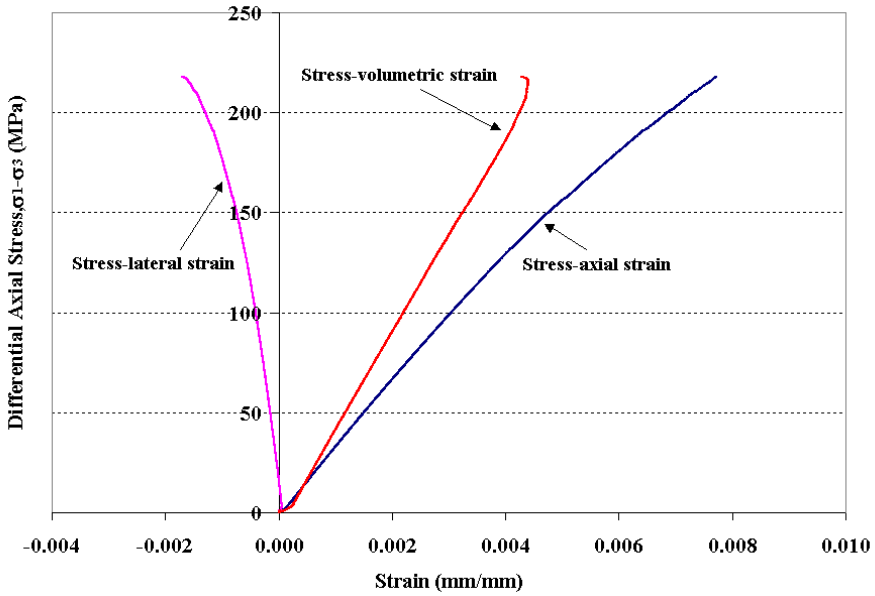

Figure 1.3.1 Stress-strain curves for specimen 01026241-1-T, Confining pressure = 5 MPa, Axial stress at failure = 222.67 MPa, Stress rate = 0.0035 MPa/s

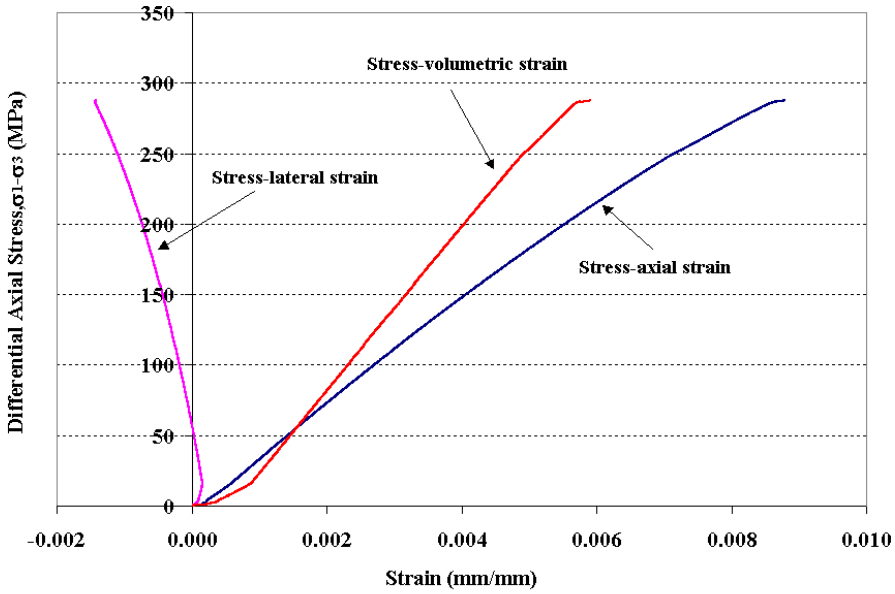

Figure 1.3.2 Stress-strain curves for specimen 01026145-1-T, Confining pressure = 10 MPa, Axial stress at failure = 297.62 MPa, Stress rate = 0.0037 MPa/s

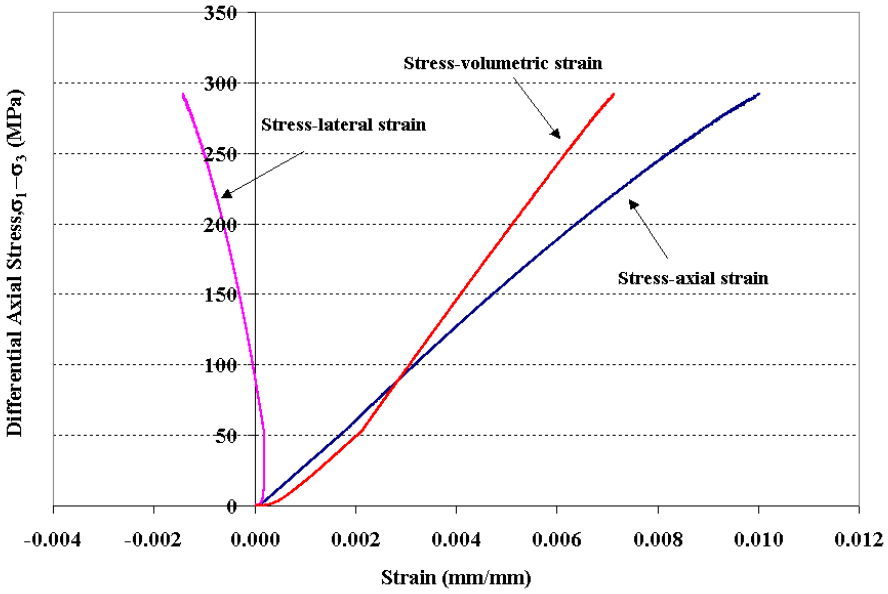

Figure 1.3.3 Stress-strain curves for specimen 01026146-1-T, Confining pressure = 20 MPa, Axial stress at failure = 312.23 MPa, Stress rate = 0.0035 MPa/s

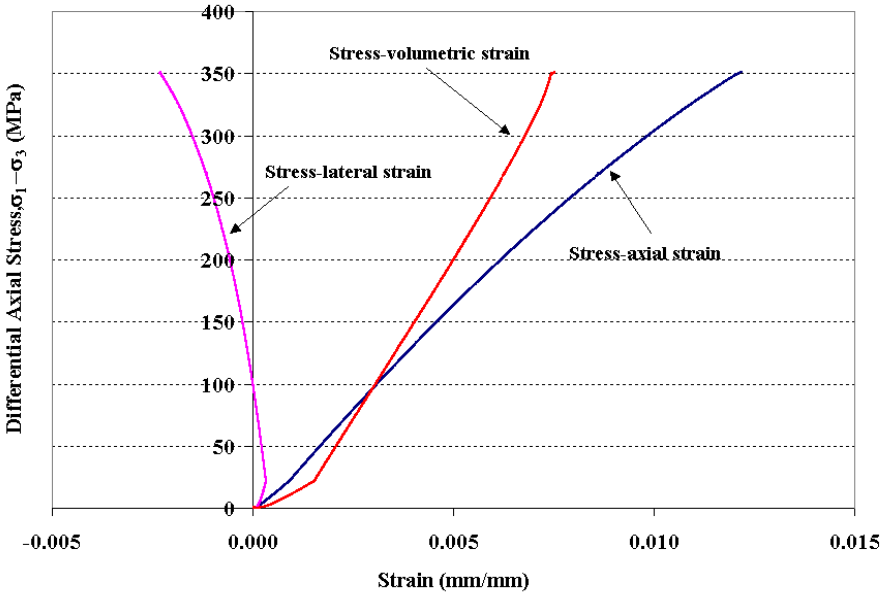

Figure 1.3.4 Stress-strain curves for specimen 01026255-1-T, Confining pressure = 20 MPa, Axial stress at failure = 370.88 MPa, Stress rate = 0.0036 MPa/s

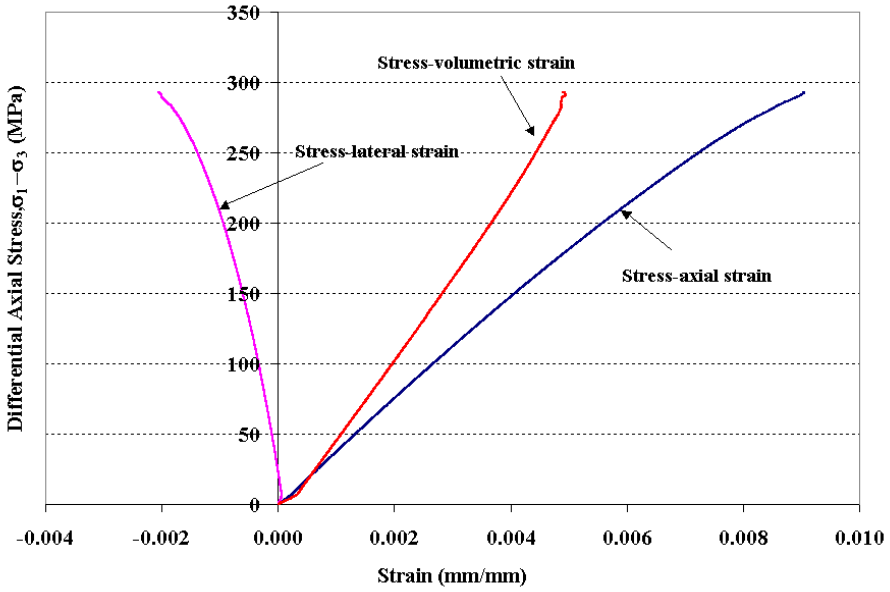

Figure 1.3.5 Stress-strain curves for specimen 01026258-4-T, Confining pressure = 5 MPa, Axial stress at failure = 297.54 MPa, Stress rate = 0.0038 MPa/s

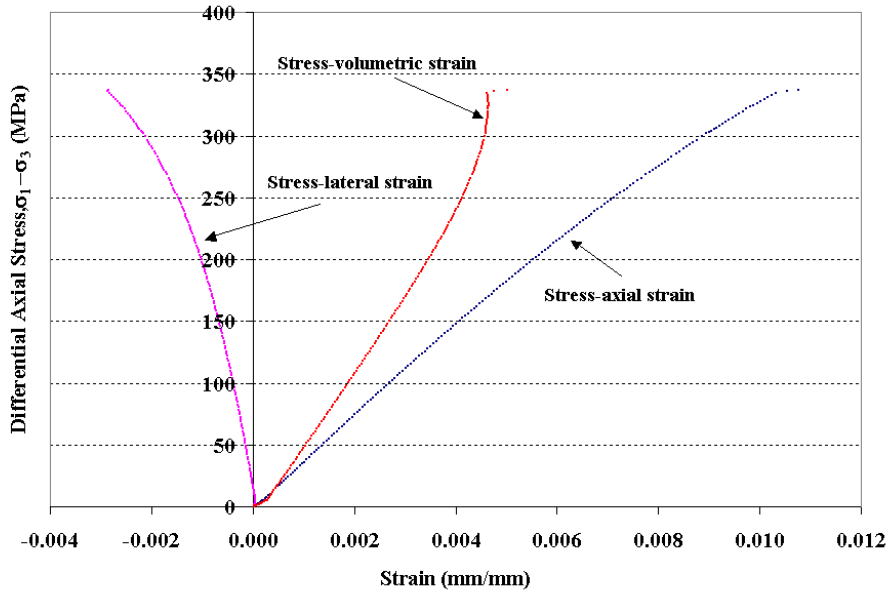

Figure 1.3.6 Stress-strain curves for specimen 01026153-1-T, Confining pressure = 5 MPa, Axial stress at failure = 342.13 MPa, Stress rate = 0.3772 MPa/s

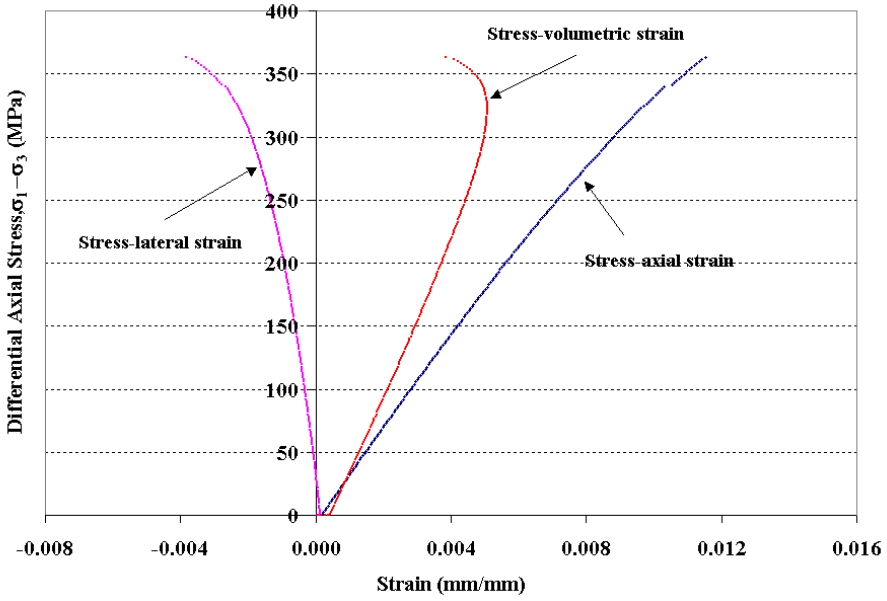

Figure 1.3.7 Stress-strain curves for specimen 01026144-1-T, Confining pressure = 10 MPa, Axial stress at failure = 373.76 MPa, Stress rate = 0.3743 MPa/s

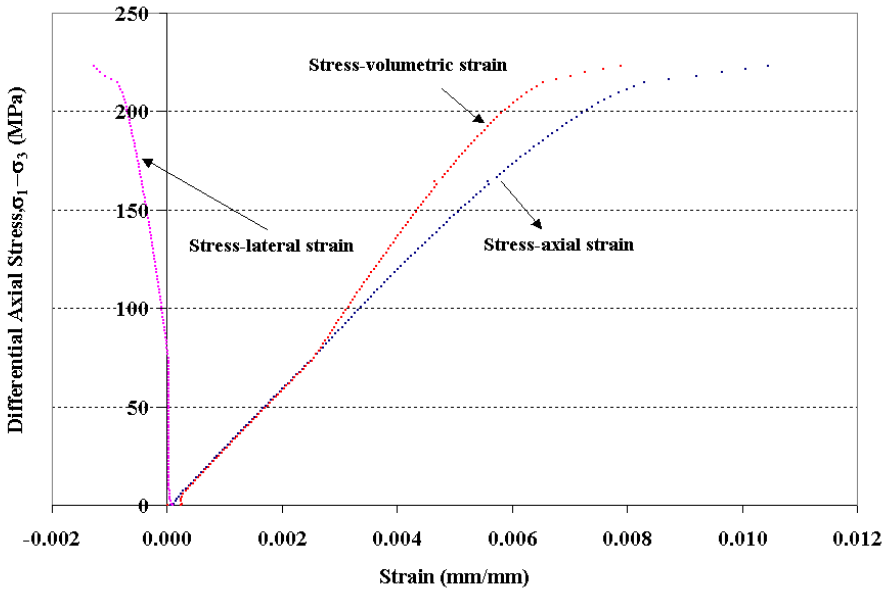

Figure 1.3.8 Stress-strain curves for specimen 01026253-1-T, Confining pressure = 20 MPa, Axial stress at failure = 243.21 MPa, Stress rate = 0.3560 MPa/s

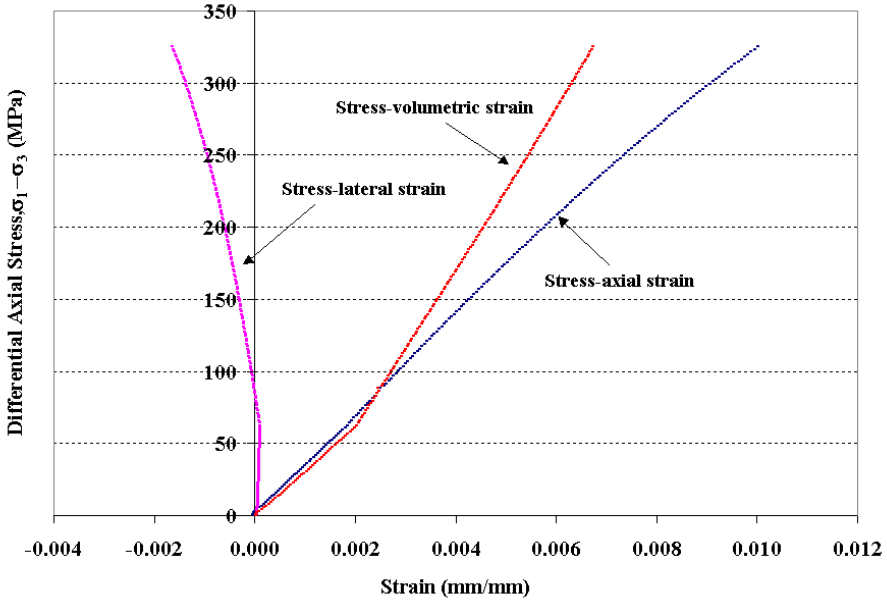

Figure 1.3.9 Stress-strain curves for specimen 01026145-2-T, Confining pressure = 20 MPa, Axial stress at failure = 344.98 MPa, Stress rate = 0.3952 MPa/s

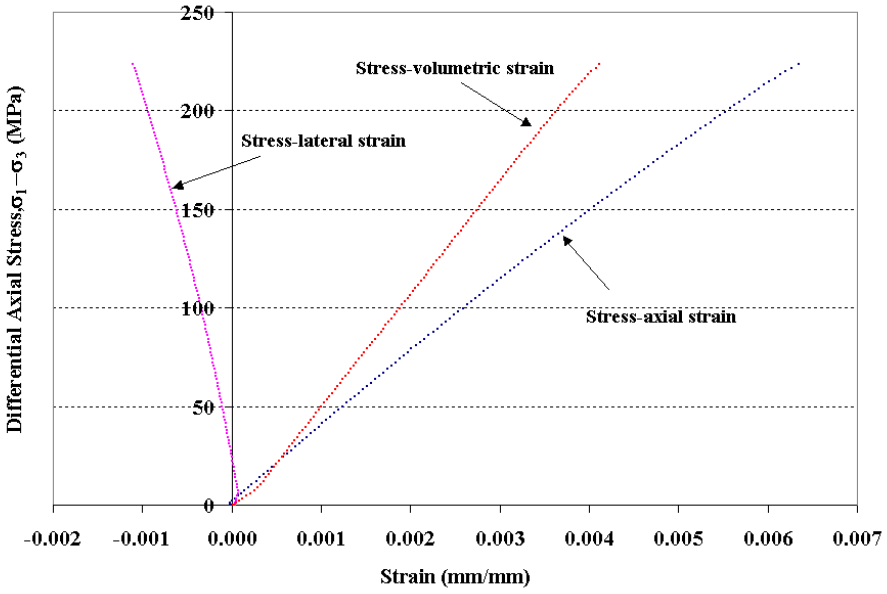

Figure 1.3.10 Stress-strain curves for specimen 01026541-2-T, Confining pressure = 5 MPa, Axial stress at failure = 228.3 MPa, Stress rate = 0.3748 MPa/s

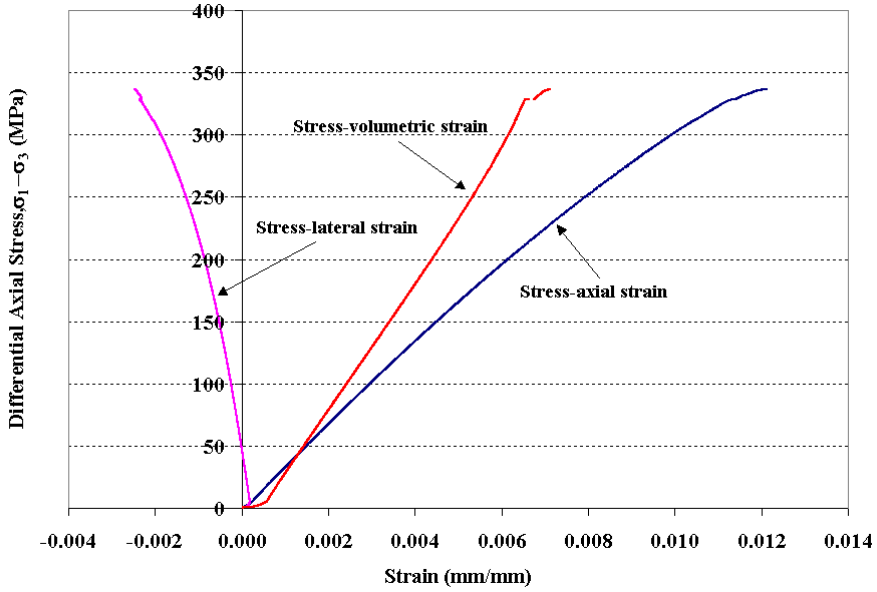

Figure 1.3.11 Stress-strain curves for specimen 01026225-6-T, Confining pressure = 10 MPa, Axial stress at failure = 346.46 MPa, Stress rate = 0.0375 MPa/s

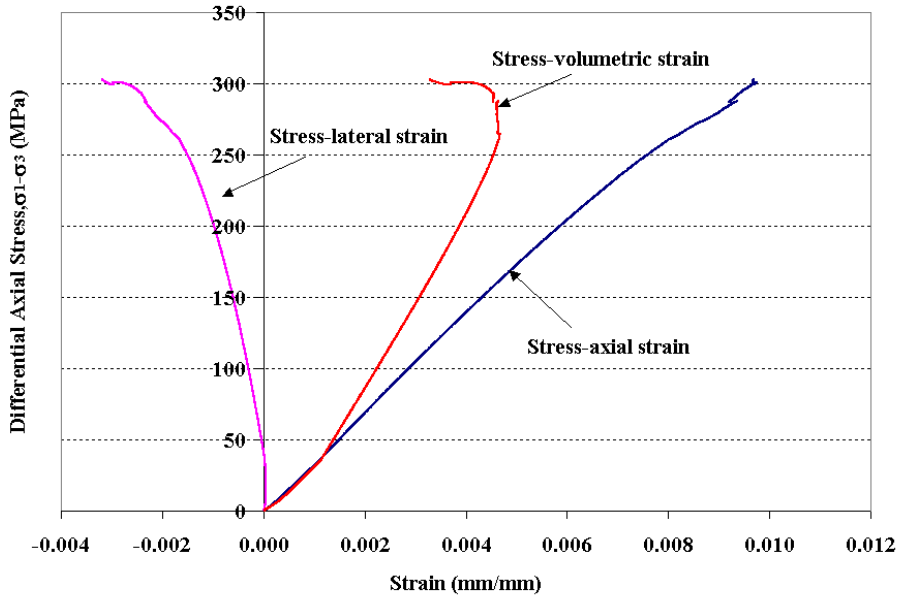

Figure 1.3.12 Stress-strain curves for specimen 01026227-2-T, Confining pressure = 10 MPa, Axial stress at failure = 312.55 MPa, Stress rate = 0.0396 MPa/s

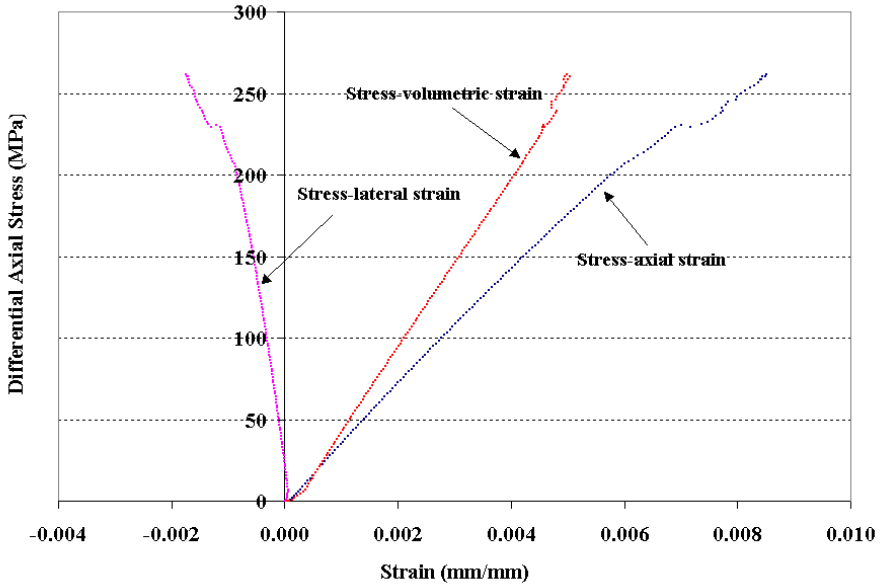

Figure 1.3.13 Stress-strain curves for specimen 01026226-1-T, Confining pressure = 5 MPa, Axial stress at failure = 266.74 MPa, Stress rate = 0.3647 MPa/s

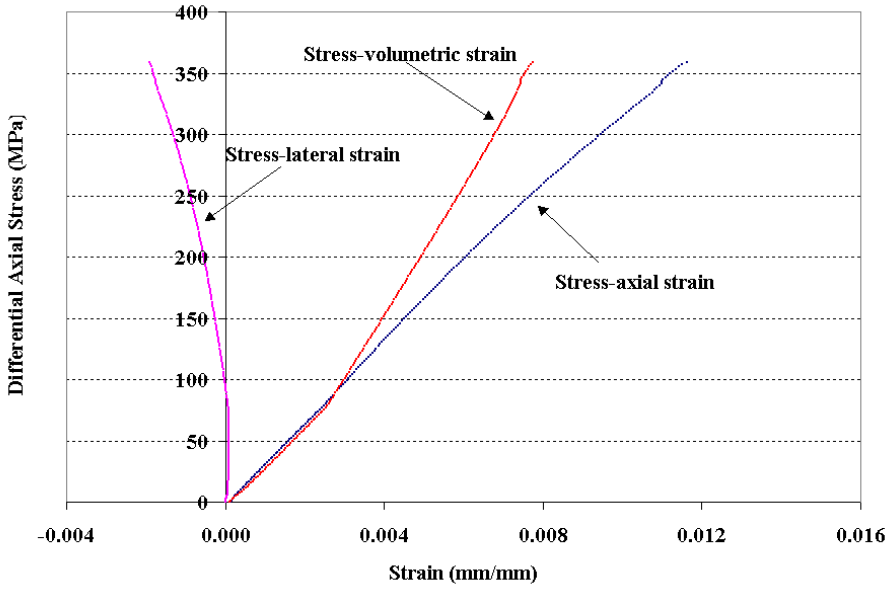

Figure 1.3.14 Stress-strain curves for specimen 01026229-2-T, Confining pressure = 20 MPa, Axial stress at failure = 378.43 MPa, Stress rate = 0.3872 MPa/s

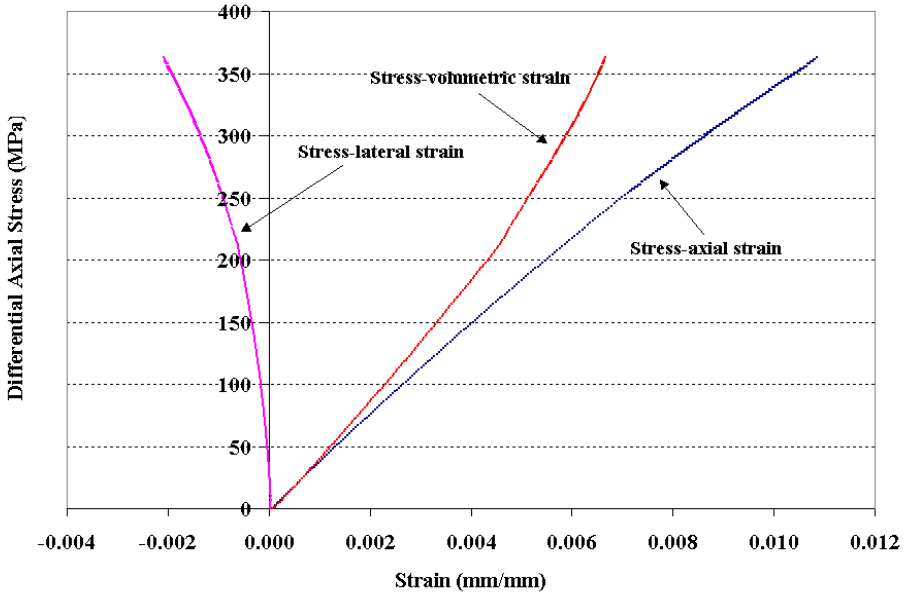

Figure 1.3.15 Stress-strain curves for specimen 01026227-1-T, Confining pressure = 20 MPa, Axial stress at failure = 382.66 MPa, Stress rate = 0.0040 MPa/s

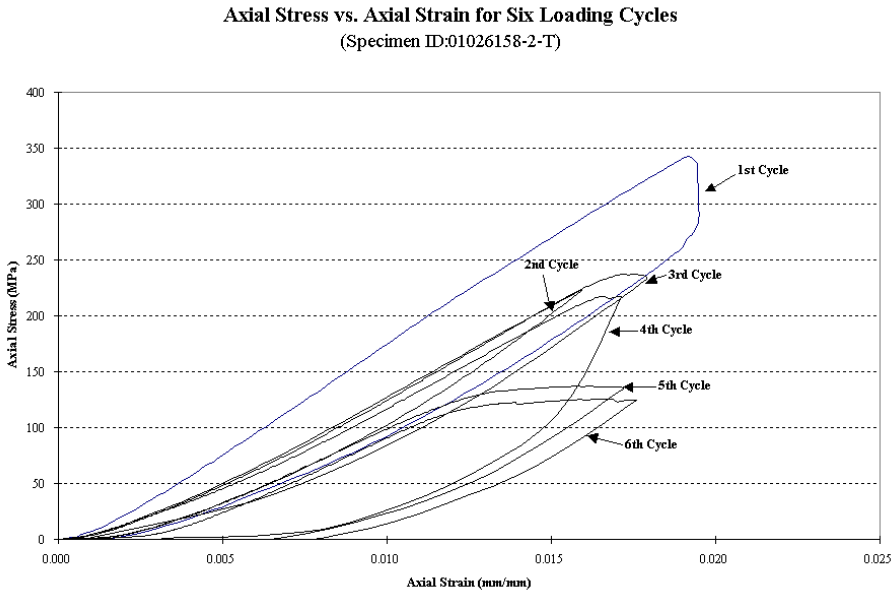

Figure 1.3.16 Axial stress vs. axial strain for six loading cycles, specimen ID 01026158-2-T, the confining pressure for these tests was 10 MPa

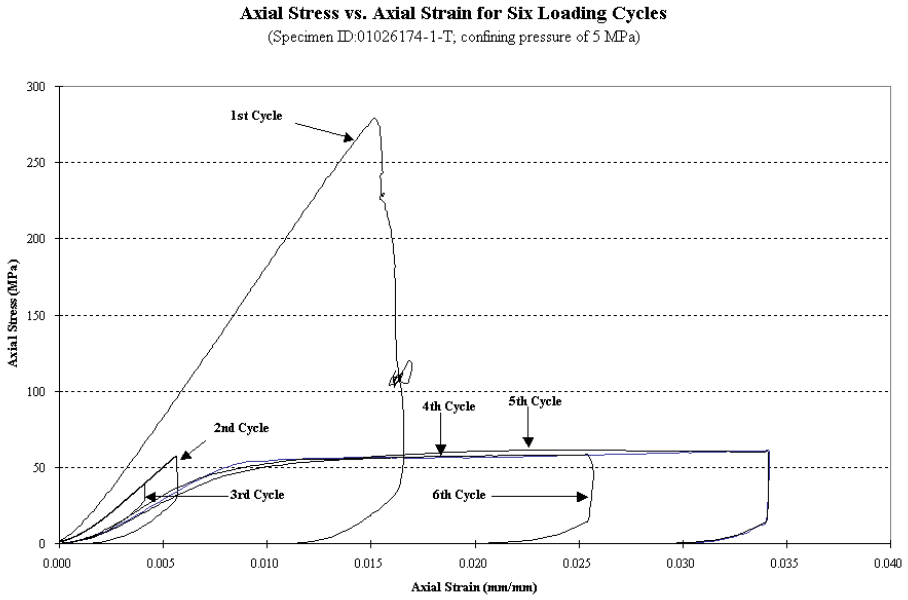

Figure 1.3.17 Axial stress vs axial strain for six loading cycles, specimen ID 01026174-1-T, the confining pressure for these tests was 5 MPa

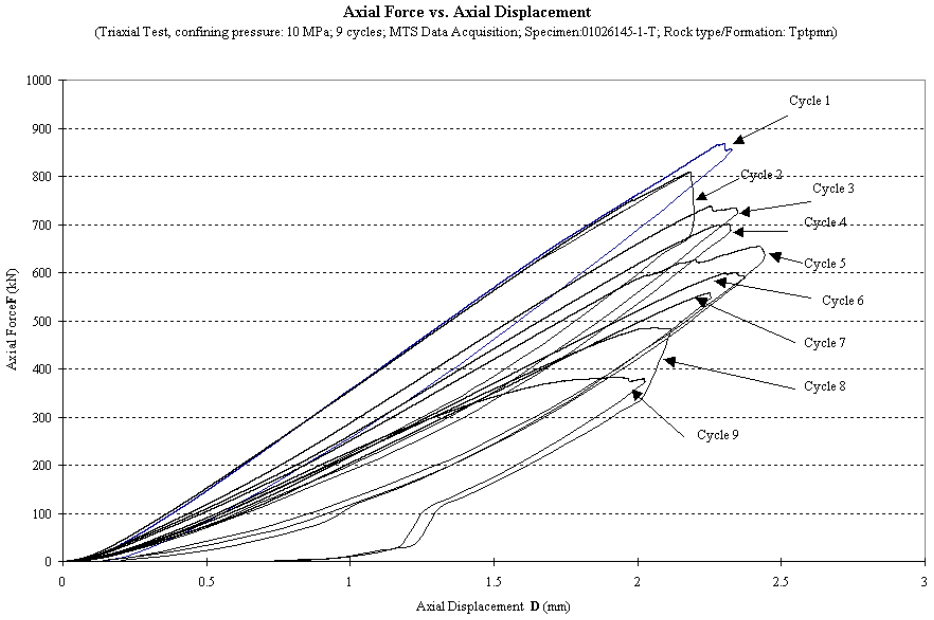

Figure 1.3.18 Axial force vs axial displacement for six loading cycles, specimen ID 01026145-1-T, the confining pressure for these tests was 10 MPa

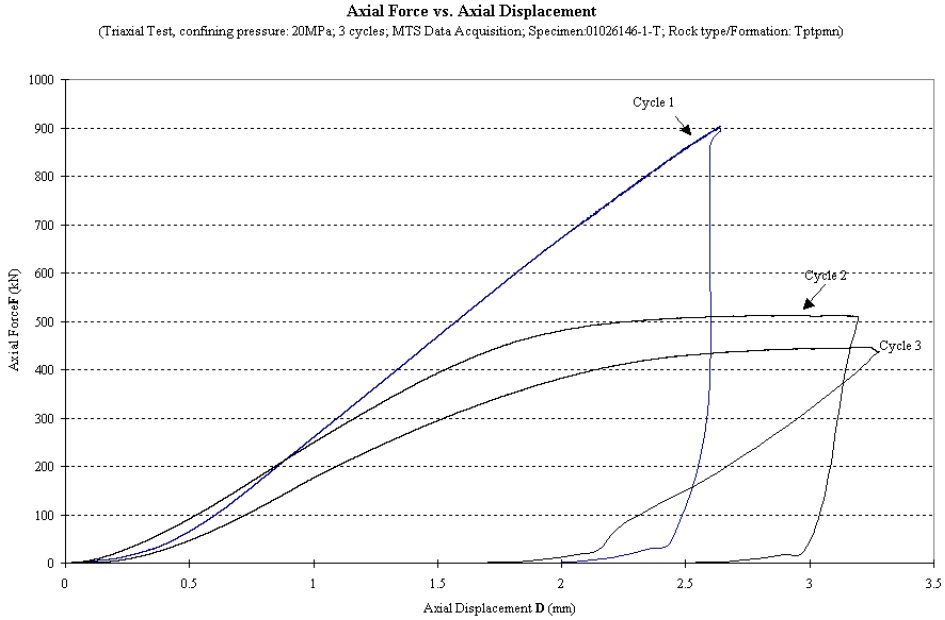

Figure 1.3.19 Axial force vs axial displacement for six loading cycles, specimen ID 01026146-1-T, the confining pressure for these tests was 20 MPa

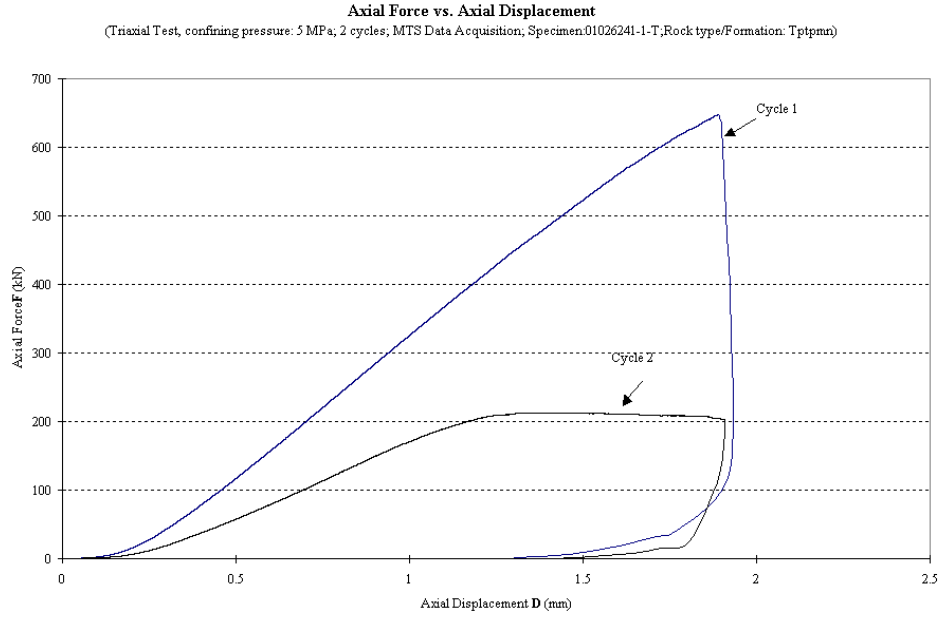

Figure 1.3.20 Axial force vs axial displacement for six loading cycles, specimen ID 01026241-1-T, the confining pressure for these tests was 5 MPa

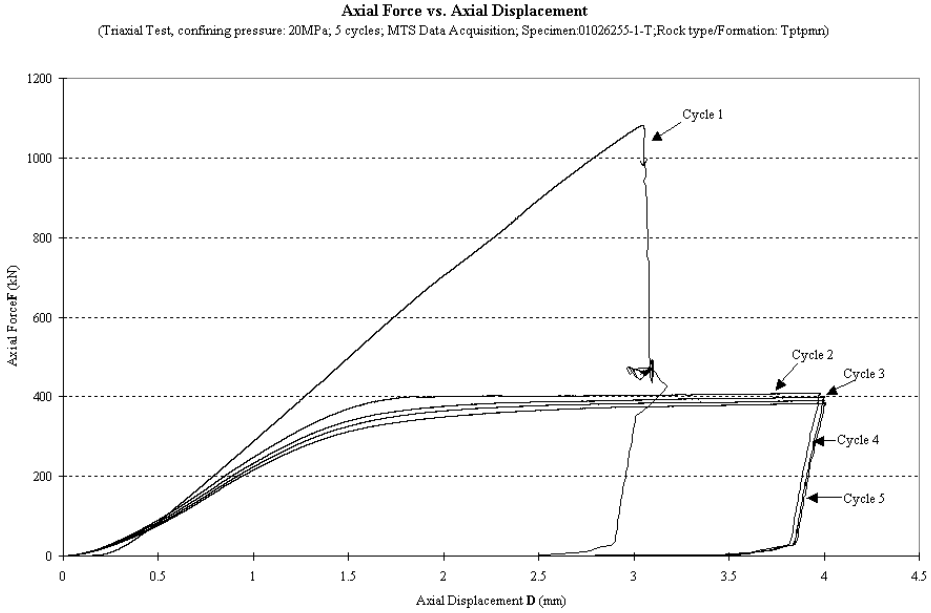

Figure 1.3.21 Axial force vs axial displacement for six loading cycles, specimen ID 01026255-1-T, the confining pressure for these tests was 20 MPa

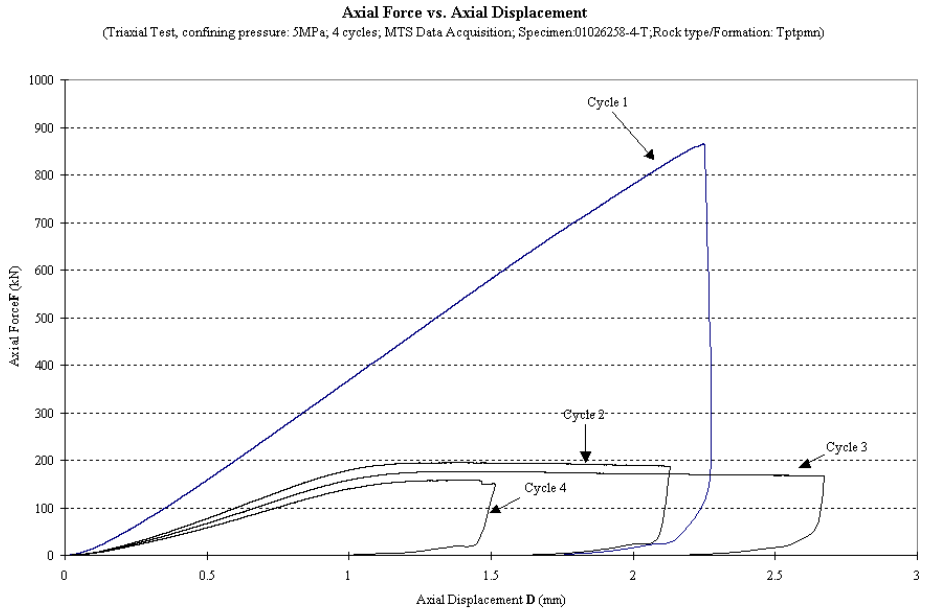

Figure 1.3.22 Axial force vs axial displacement for six loading cycles, specimen ID 01026258-4-T, the confining pressure for these tests was 5 MPa

1.4 Failure Envelopes

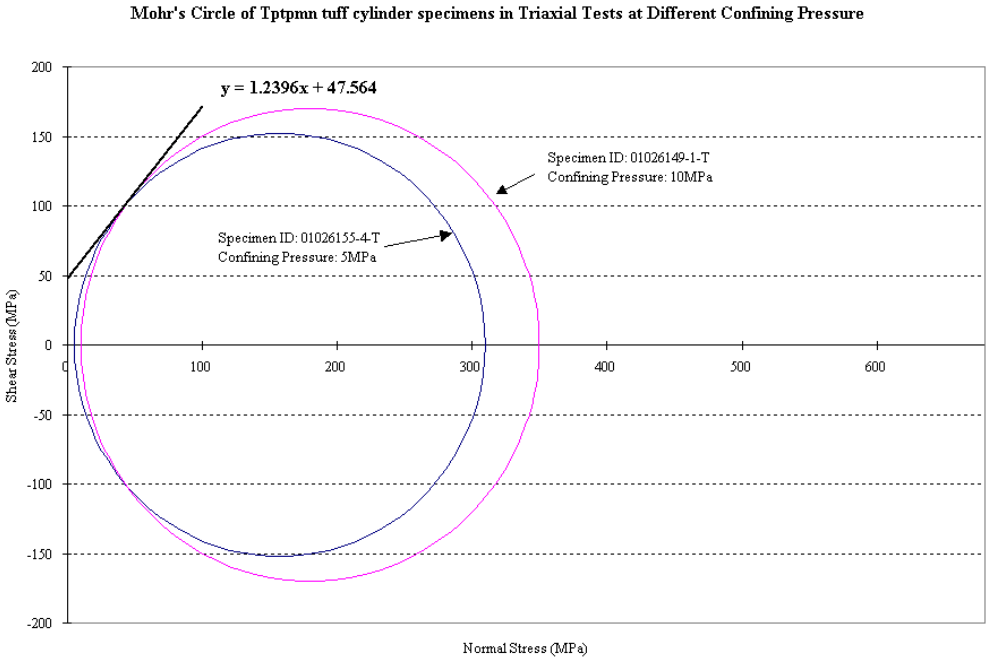

Figure 1.4.1 Strength envelope

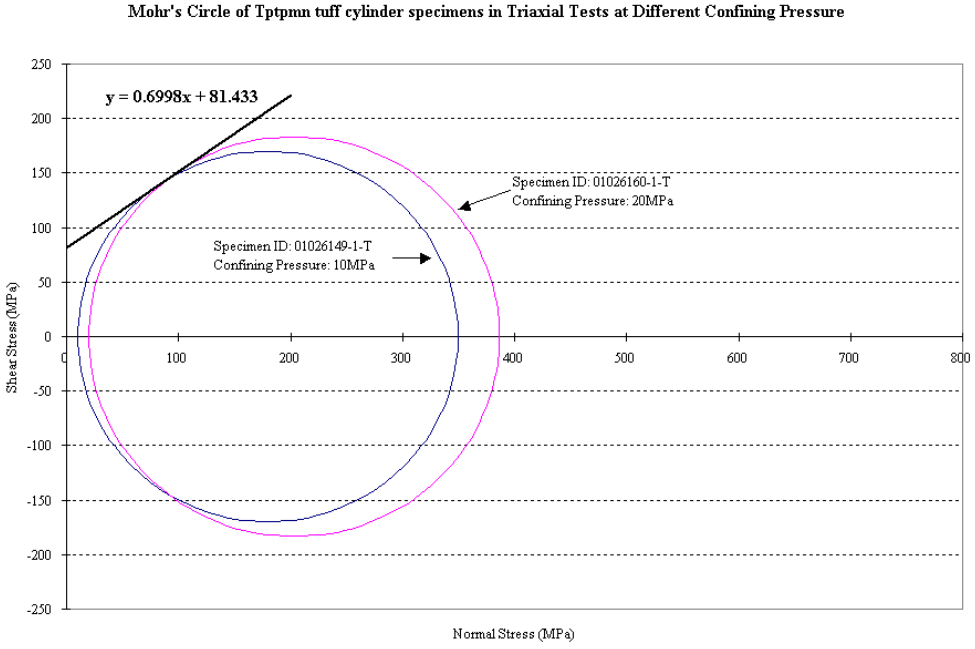

Figure 1.4.2 Strength envelope

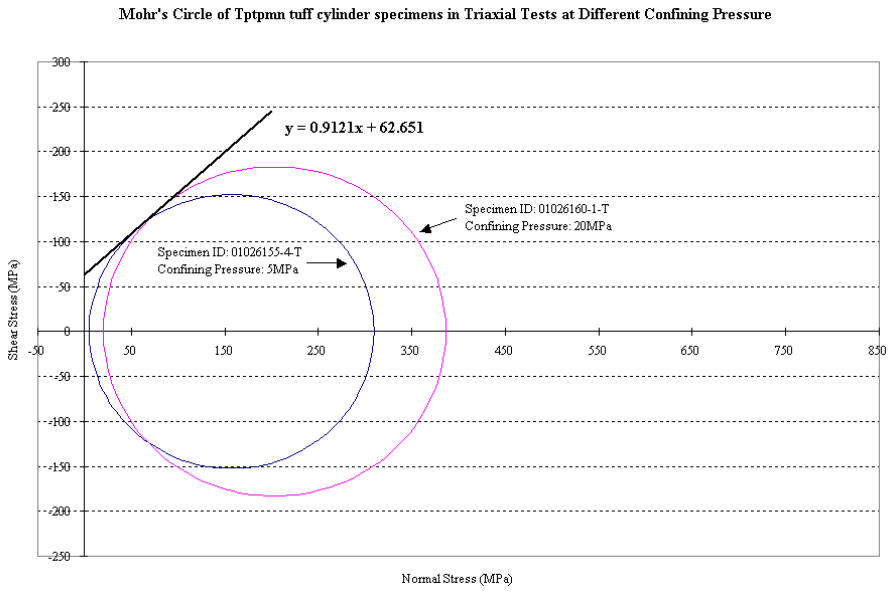

Figure 1.4.3 Strength envelope

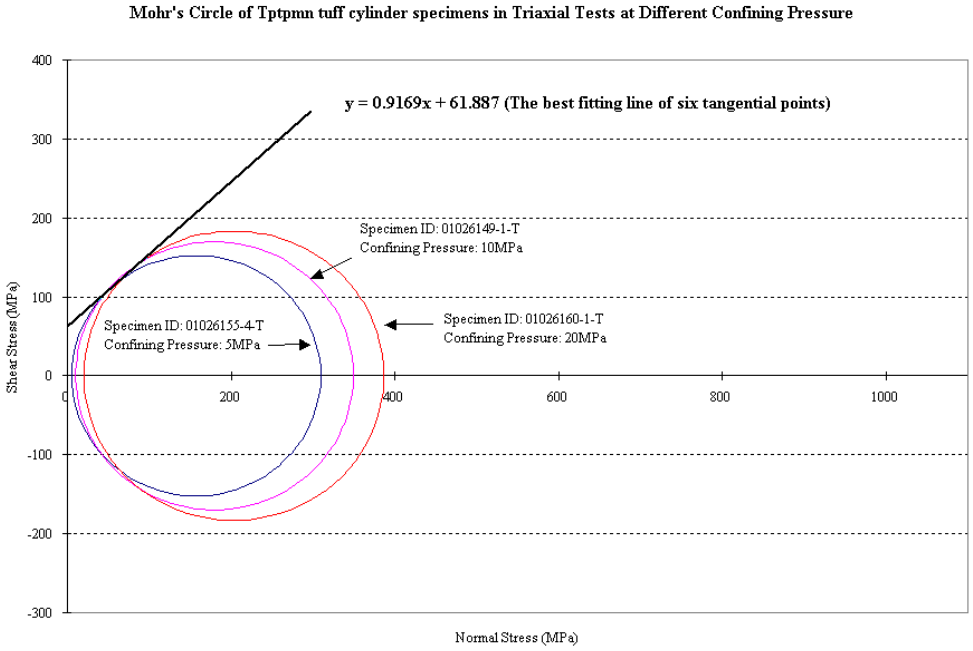

Figure 1.4.4 Strength envelope

1.5 Specimen Photographs

Figure 1.5.1 Specimen after triaxial test, specimen ID 01026144-1-T

Figure 1.5.2 Specimen after triaxial test, specimen ID 01026145-1-T

Figure 1.5.3 Specimen after triaxial test, specimen ID 01026145-2-T

Figure 1.5.4 Specimen after triaxial test, specimen ID 01026153-1-T

Figure 1.5.5 Specimen after triaxial test, specimen ID 01026225-6-T

Figure 1.5.6 Specimen after triaxial test, specimen ID 01026229-2-T

Figure 1.5.7 Specimen after triaxial test, specimen ID 01026241-1-T

Figure 1.5.8 Specimen after triaxial test, specimen ID 01026258-4-T

Appendix 2 - Indirect Tensile Splitting “Brazilian” Tests

2.1 Summary of results

By Feb. 17th, 2006, all together 111 indirect tensile splitting ("Brazilian") tests were performed. Among them, there are 99 valid tests, which mean the primary fracture of these tests is diametrical or nearly diametrical. The maximum tensile strength is 23.69 MPa, the minimum tensile strength is 7.71MPa, and the average tensile strength is 16.45MPa.

Most of the specimens used in these tests are with the diameter of approximate 60.96 mm, some smaller ones with diameter of approximate 44.96 mm were also used.

The specimen characteristics of valid tests and corresponding test results are summarized in Table 2.1.

2.2 The influence factors of tensile strength

From table 2.1 we can see that the tensile strength is very scattering. This is caused by multi -factors. The main influence factors are summarized as follows:

2.2.1 Geological formations

All the specimens are from the two geological formations: Topopah Spring crystal-poor middle nonlithphysal zone (Tptpmn) and Topopah Spring crystal-poor lower nonlithphysal zone (Tptpln). It seems that the rock cores from the different formations are made up from the different grains, and their appearances are much different, see Fig. 2.1 and 2.2. According to test results, their strength is also different: for specimens from Tptpmn formations, the mean tensile strength is 17.03 MPa, which is 21.7% higher than that of the ones from Tptpln (13.99 MPa).

2.2.2 Flaws

Here flaws mainly refer to a kind of special weak spot in specimen: the vapor-phase altered spot, which is a region of tuff matrix altered by gases in the early stage of tuff emplacement and is common in Yucca mountain tuffs. The flaw's influence on tensile strength mainly depends on two aspects:

1) Flaw quantity

Because the vapor-phase altered spots have lower density, the density of specimen will decreased along with the increasing of the flaws. Thus we can use the average density of the specimen as the indicator of the quantity of the flaws.
In order to find the influence of the flaw quantity on tensile strength, the specimen tensile strength-density distribution plot was generated and the trend line was added (See Figure 2.3).

Table 2.1 Brazilian test samples, source, rock type, geometry, density, strength and imposed test machine displacement rate

Serial #	Specimen ID	Borehole	Geological Formation	Diameter (mm)	Thickness (mm)	Density (kg/m^3)	Strength (MPa)	Displ. Rate (mm/min)
1	01026261-2-B	UE-25 UZ#16	Tptpln	60.81	23.19	2287.42	12.60	0.200000
2	01026143-3-B	ESF-HD-CHE-8	Tptpmn	60.83	29.18	2257.76	16.84	0.200000
3	01026154-3-B	ESF-HD-CHE-8	Tptpmn	60.88	21.08	2263.73	17.82	0.200000
4	01026159-3-B	ESF-HD-CHE-8	Tptpmn	60.93	29.79	2279.31	16.75	0.200000
5	01026243-1-B	ESF-HD-WH-46	Tptpmn	60.88	26.31	2289.74	21.52	0.200000
6	01026261-1-B	UE-25 UZ#16	Tptpln	60.76	23.57	2261.17	11.89	0.200000
7	01026264-1-B	UE-25 UZ#16	Tptpln	60.81	26.75	2053.87	8.57	0.200000
8	01026264-2-B	UE-25 UZ#16	Tptpln	60.76	21.79	2151.37	10.14	0.200000
9	01026315-1-B	UE-25 UZ#16	Tptpln	60.71	31.29	2325.50	16.42	0.200000
10	01026315-2-B	UE-25 UZ#16	Tptpln	60.66	25.88	2326.35	16.12	0.200000
11	01026316-1-B	UE-25 UZ#16	Tptpln	60.35	26.14	2185.63	14.59	0.200000
12	01026321-1-B	UE-25 UZ#16	Tptpln	60.78	28.12	2341.04	17.73	0.200000
13	01026378-1-B	UE-25 UZ#16	Tptpln	60.63	26.42	2339.62	12.71	0.200000
14	01026378-2-B	UE-25 UZ#16	Tptpln	60.60	26.42	2290.84	16.69	0.200000
15	01026378-3-B	UE-25 UZ#16	Tptpln	60.60	26.24	2304.38	19.04	0.200000
16	01026143-1-B	ESF-HD-CHE-8	Tptpmn	60.88	28.09	2250.02	12.70	0.200000
17	01026143-2-B	ESF-HD-CHE-8	Tptpmn	60.86	27.25	2258.66	19.34	0.200000
18	01026147-1-B	ESF-HD-CHE-8	Tptpmn	60.60	30.58	2279.29	17.80	0.200000
19	01026147-2-B	ESF-HD-CHE-8	Tptpmn	60.63	24.03	2277.83	23.69	0.200000
20	01026155-3-B	ESF-HD-CHE-8	Tptpmn	60.88	22.05	2442.08	20.47	0.200000
21	01026156-1-B	ESF-HD-CHE-8	Tptpmn	60.88	28.85	2273.65	16.30	0.200000

Serial #	Specimen ID	Borehole	Geological Formation	Diameter (mm)	Thickness (mm)	Density (kg/m^3)	Strength (MPa)	Displ. Rate (mm/min)
22	01026157-2-B	ESF-HD-CHE-8	Tptpmn	60.91	28.42	2274.85	17.58	0.200000
23	01026160-3-B	ESF-HD-CHE-8	Tptpmn	60.91	19.69	2267.86	20.89	0.200000
24	01026241-2-B	ESF-HD-WH-46	Tptpmn	60.86	27.23	2285.18	15.89	0.200000
25	01026249-1-B	ESF-HD-WH-47	Tptpmn	60.86	28.88	2236.86	12.22	0.200000
26	01026251-1-B	ESF-HD-WH-47	Tptpmn	60.91	26.75	2297.08	12.64	0.200000
27	01026251-2-B	ESF-HD-WH-47	Tptpmn	60.96	27.08	2297.13	18.51	0.200000
28	01026251-3-B	ESF-HD-WH-47	Tptpmn	60.96	24.64	2302.46	22.04	0.200000
29	01026254-1-B	ESF-HD-WH-41	Tptpmn	60.83	25.63	2295.45	13.77	0.200000
30	01026257-3-B	ESF-HD-WH-41	Tptpmn	60.96	25.63	2292.76	18.99	0.200000
31	01026258-2-B	ESF-HD-WH-41	Tptpmn	60.68	23.95	2274.67	19.18	0.200000
32	01026143-4-B	ESF-HD-CHE-8	Tptpmn	60.86	29.34	2267.07	13.99	0.020000
33	01026157-1-B	ESF-HD-CHE-8	Tptpmn	60.88	33.71	2282.92	12.86	0.020000
34	01026159-1-B	ESF-HD-CHE-8	Tptpmn	60.86	30.56	2272.12	11.62	0.020000
35	01026159-2-B	ESF-HD-CHE-8	Tptpmn	60.91	26.01	2248.04	7.71	0.020000
36	01026241-3-B	ESF-HD-WH-46	Tptpmn	60.81	29.62	2195.91	10.96	0.020000
37	01026245-1-B	ESF-HD-WH-46	Tptpmn	60.83	29.26	2246.20	11.29	0.020000
38	01026254-2-B	ESF-HD-WH-41	Tptpmn	60.83	27.89	2299.72	18.74	0.020000
39	01026544-2-B	ESF-HD-CHE-8	Tptpmn	60.83	27.61	2261.55	17.52	0.200000
40	01026266-1-B	UE-25 UZ#16	Tptpln	60.73	22.71	2317.85	13.28	0.020000
41	01026309-1-B	UE-25 UZ#16	Tptpln	60.83	23.80	2326.76	11.19	2.000000
42	01026234-2-B	ESF-HD-WH-44	Tptpmn	60.73	26.21	2251.33	17.43	2.000000
43	01026245-2-B	ESF-HD-WH-46	Tptpmn	60.88	26.64	2243.08	15.13	2.000000
44	01026256-2-B	ESF-HD-WH-41	Tptpmn	60.96	24.46	2292.02	20.89	0.020000

Serial #	Specimen ID	Borehole	Geological Formation	Diameter (mm)	Thickness (mm)	Density (kg/m^3)	Strength (MPa)	Displ. Rate (mm/min)
45	01026257-2-B	ESF-HD-WH-41	Tptpmn	60.93	25.55	2289.43	20.86	2.000000
46	01026149-2-B	ESF-HD-CHE-8	Tptpmn	60.86	29.87	2239.84	13.69	2.000000
47	01026154-2-B	ESF-HD-CHE-8	Tptpmn	60.86	27.03	2250.87	12.91	0.002000
48	01026234-1-B	ESF-HD-WH-44	Tptpmn	60.76	26.72	2291.44	19.36	2.000000
49	01026242-1-B	ESF-HD-WH-46	Tptpmn	60.91	27.81	2265.13	16.67	2.000000
50	01026248-3-B	ESF-HD-WH-47	Tptpmn	60.93	27.56	2251.94	14.91	2.000000
51	01026249-2-B	ESF-HD-WH-47	Tptpmn	60.88	27.25	2269.80	18.26	2.000000
52	01026250-1-B	ESF-HD-WH-47	Tptpmn	60.93	27.74	2312.32	18.98	2.000000
53	01026256-1-B	ESF-HD-WH-41	Tptpmn	60.96	28.27	2284.98	22.05	2.000000
54	01026544-1-B	ESF-HD-CHE-8	Tptpmn	60.83	25.76	2245.75	22.53	2.000000
55	01026310-2-B	UE-25 UZ#16	Tptpln	60.20	26.97	2287.17	10.24	0.200000
56	01026144-2-B	ESF-HD-CHE-8	Tptpmn	60.86	31.72	2243.07	14.08	0.200000
57	01026145-4-B	ESF-HD-CHE-8	Tptpmn	60.83	21.62	2275.32	22.91	0.200000
58	01026145-5-B	ESF-HD-CHE-8	Tptpmn	60.86	25.96	2223.55	21.33	0.200000
59	01026148-1-B	ESF-HD-CHE-8	Tptpmn	60.81	27.74	2271.70	16.18	0.200000
60	01026148-2-B	ESF-HD-CHE-8	Tptpmn	60.83	28.27	2265.13	15.36	0.200000
61	01026148-3-B	ESF-HD-CHE-8	Tptpmn	60.81	26.44	2271.63	18.89	0.200000
62	01026541-1-B	ESF-HD-CHE-8	Tptpmn	60.86	28.32	2307.56	8.87	0.200000
63	01026155-2-B	ESF-HD-CHE-8	Tptpmn	60.88	23.95	2265.36	21.20	0.200000
64	01026160-4-B	ESF-HD-CHE-8	Tptpmn	60.91	21.54	2237.53	11.69	0.200000
65	01026248-2-B	ESF-HD-WH-47	Tptpmn	60.93	25.73	2220.68	15.87	0.200000
66	01026258-1-B	ESF-HD-WH-41	Tptpmn	60.58	26.06	2276.57	10.70	0.200000
67	01026259-2-B	ESF-HD-WH-41	Tptpmn	60.91	25.73	2280.40	18.92	0.200000

Serial #	Specimen ID	Borehole	Geological Formation	Diameter (mm)	Thickness (mm)	Density (kg/m^3)	Strength (MPa)	Displ. Rate (mm/min)
68	01026248-1-B	ESF-HD-WH-47	Tptpmn	60.96	29.42	2247.81	18.84	0.200000
69	01026297-1-B	ESF-HD-CHE-1	Tptpmn	60.96	35.00	2246.57	12.58	0.200000
70	01026374-1-B	UE-25 UZ#16	Tptpln	60.96	34.62	2349.78	10.44	0.200000
71	01026163-1-B	ESF-HD-CHE-2	Tptpmn	60.96	30.28	2285.54	12.46	0.200000
72	01026294-2-B	ESF-HD-CHE-1	Tptpmn	60.96	20.52	2303.28	18.87	0.002000
73	01026294-3-B	ESF-HD-CHE-1	Tptpmn	60.96	32.23	2287.02	18.54	0.002000
74	01026294-1-B	ESF-HD-CHE-1	Tptpmn	60.96	20.74	2288.41	20.22	0.002000
75	01026165-2-B	ESF-HD-CHE-2	Tptpmn	60.96	29.74	2291.97	16.03	0.002000
76	01026310-1-B	UE-25 UZ#16	Tptpln	60.35	30.12	2304.60	11.52	0.002000
77	01026373-1-B	UE-25 UZ#16	Tptpln	60.96	28.55	2329.04	18.90	0.002000
78	01026374-2-B	UE-25 UZ#16	Tptpln	60.96	26.92	2347.00	10.94	0.002000
79	01026184-2-B	ESF-HD-CHE-1	Tptpmn	60.96	29.08	2245.06	13.90	0.000200
80	01026161-2-B	ESF-HD-CHE-2	Tptpmn	60.96	28.42	2247.80	12.85	0.000200
81	01026161-3-B	ESF-HD-CHE-2	Tptpmn	60.96	29.49	2266.02	18.75	0.000200
82	01026184-1-B	ESF-HD-CHE-1	Tptpmn	60.96	28.24	2274.08	18.34	0.000200
83	01026204-1-B	ESF-HD-CHE-6	Tptpmn	44.93	24.26	2239.92	21.24	0.145000
84	01026208-1-B	ESF-HD-CHE-6	Tptpmn	44.96	22.38	2265.66	18.22	0.145000
85	01026208-4-B	ESF-HD-CHE-6	Tptpmn	44.93	18.64	2266.61	17.63	0.145000
86	01026209-1-B	ESF-HD-CHE-6	Tptpmn	44.93	19.66	2293.03	22.74	0.001450
87	01026210-2-B	ESF-HD-CHE-6	Tptpmn	44.96	21.08	2270.31	15.14	0.145000
88	01026211-1-B	ESF-HD-CHE-6	Tptpmn	44.98	21.13	2279.46	20.46	0.145000
89	01026209-5-B	ESF-HD-CHE-6	Tptpmn	44.96	19.66	2281.88	16.93	0.001450
90	01026211-2-B	ESF-HD-CHE-6	Tptpmn	44.98	21.133	2256.85	19.81	0.001450

Serial #	Specimen ID	Borehole	Geological Formation	Diameter (mm)	Thickness (mm)	Density (kg/m^3)	Strength (MPa)	Displ. Rate (mm/min)
91	01026204-2-B	ESF-HD-CHE-6	Tptpmn	44.96	21.33	2260.02	18.51	0.001450
92	01026210-1-B	ESF-HD-CHE-6	Tptpmn	44.98	22.81	2246.95	13.47	0.001450
93	01026209-6-B	ESF-HD-CHE-6	Tptpmn	44.95	24.98	2283.49	18.15	0.000145
94	01026209-4-B	ESF-HD-CHE-6	Tptpmn	44.96	19.66	2293.06	18.25	0.000145
95	01026167-2-B	ESF-HD-CHE-2	Tptpmn	60.07	30.17	2263.29	16.49	0.000200
96	01026206-1-B	ESF-HD-CHE-6	Tptpmn	44.99	23.24	2205.90	17.92	0.145000
97	01026210-4-B	ESF-HD-CHE-6	Tptpmn	44.99	19.25	2287.16	20.11	0.145000
98	01026167-4-B	ESF-HD-CHE-2	Tptpmn	61.10	22.19	2259.56	16.97	0.000200
99	01026269-2-B	UE-25 UZ#16	Tptpln	60.54	27.60	2290.66	22.88	0.020000

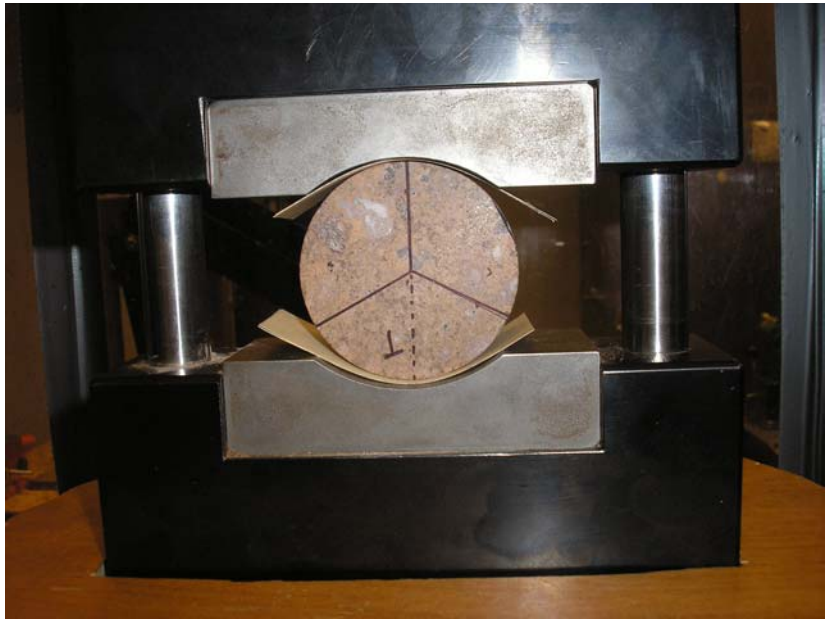

Fig. 2.1 Brazilian test arrangement (specimen diameter = 44.96 mm)

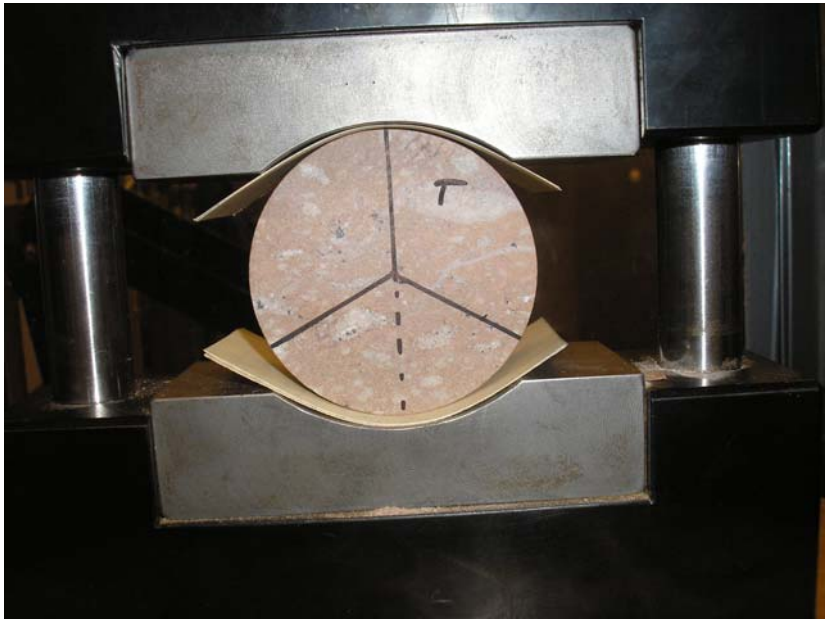

Fig.2.2 Brazilian test arrangement (specimen diameter = 60.96 mm)

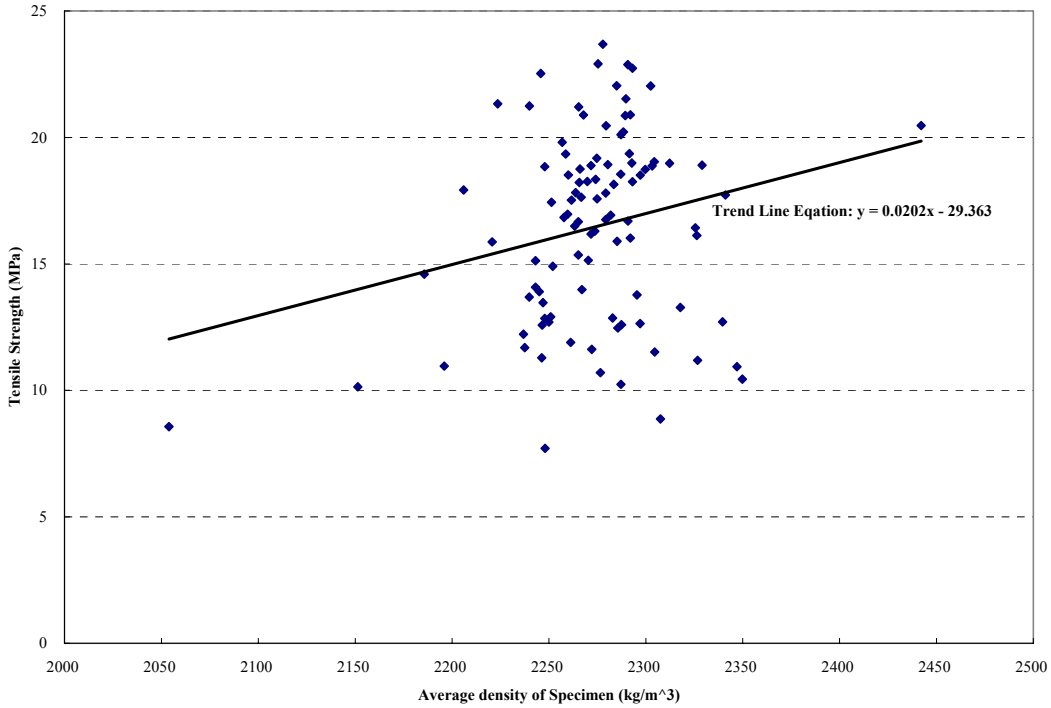

Fig. 2.3

From figure 2.3 we can see that the tensile strength increases along with the decreasing of the quantity of the vapor-phase altered spots (or: the increasing of the average density).

2) The location of flaws

If flaws are not along the loaded diameter, the specimen's mechanical characteristics will not be symmetrical, so the fracture of the specimen is no longer diametrical. This is a possible reason why most of the specimens' fracture is not exactly diametrical. If the fracture deviates from the center too much, the test will be invalid (see fig. 2.4). In the example in Fig. 2.2.4 it seems probable that the primary fracture has initiated in the vapor altered spot just to the right off center, and then has propagated along a tensile principal stress trajectory. The reported numerical value of the tensile strength probably more appropriately should be considered as a lower bound to the tensile strength? A "corrected" value could be obtained by estimating, preferably measuring, the location of the trajectory and adjusting the estimated strength accordingly. For example in Fig. 2.2.4, estimating that the primary fracture is at 0.36 R from the center, and using the (point load) stress contours in Hooper (1971, Fig. 8), we estimate the stress at the (assumed) initiation point along the horizontal diameter to have been 60% of the maximum tensile stress (at the center of the disk, horizontal).

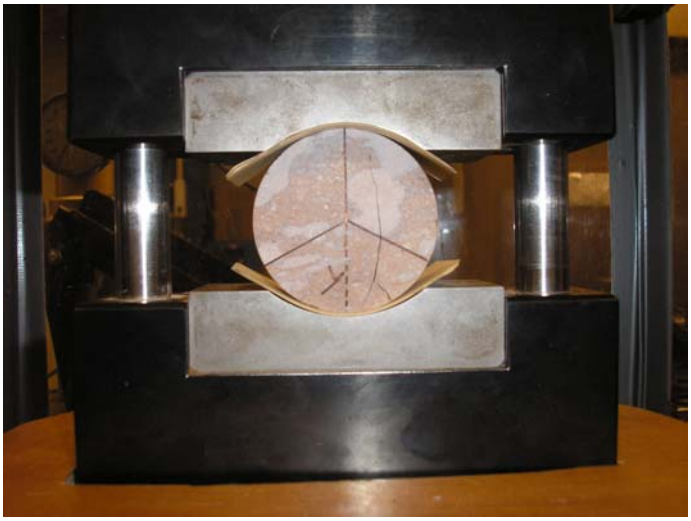

Fig. 2.4

If flaws are located on the loading diameter, they may significantly decrease the tensile strength. For example, the specimen 01026159-2-B has the lowest tensile stress (7.71MPa) of all samples, and there is an obvious flaw on the loading diameter (see fig. 2.5).

Fig. 2.5

2.2.3 Load rate

As a matter of fact, it should be displacement rate, because in our tests, load is applied by displacement control. For specimens with the diameter of about 60.96mm, the displacement rates vary from 0.0002mm/min to 2mm/min. For specimens with the diameter of about 44.96mm, the displacement rates vary from 0.000145 to 0.145mm/min.

Tensile strength-Displacement rate graph with trend line is shown in Fig. 2.6. The

figure indicates the tensile strength increases slightly with increasing load rate.

2.2.4 Contact pressure distribution

The tensile strength formula for Brazilian test is based on the assumption that the contact pressure between specimen and load platen is uniform. But because of the coarseness of specimen surface, the real contact pressure distribution is highly uneven, as discussed in detail in section 2.4: contact pressure experimental results.

To evaluate the influence of uneven pressure on the tensile strength, we conducted comparison tests: two groups of tests were performed in almost the same test conditions, and all specimens came from the same geological formation (Tptpmn). In group 1, one bearing strip (cardboard) was inserted between the specimen and load platen to distribute the pressure evenly; in group 2, two bearing strips were used to get more even pressure distribution. Test results are listed in Table 2.2.

From the table we can see that using two more bearing strips may increase the tensile strength. Because two bearing strips cause more even pressure distribution, we can draw the conclusion that uneven pressure distribution lowers the tensile strength. In all the subsequent Brazilian tests, the two bearing strips were used to attain the more precise result.

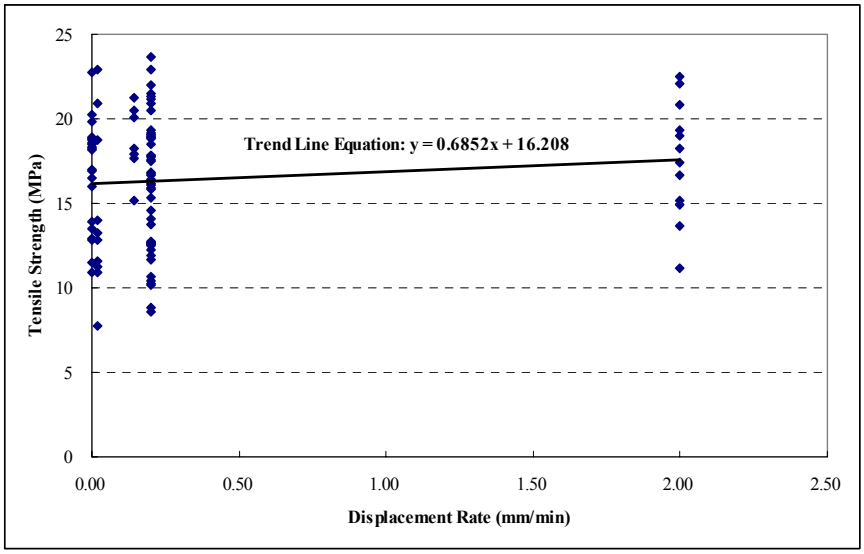

Fig. 2.6 Brazilian tensile strength as a function of imposed displacement rate

Table 2.2 Brazilian tensile strength as a function of number of cardboard inserts at each loading point. Group 1:1 insert; Group 2: 2 inserts.

Group 1		Group 2	
Specimen ID	Strength (MPa)	Specimen ID	Strength (MPa)
01026143-2-B	19.34	01026143-1-B	12.70
01026143-3-B	16.84	01026147-1-B	17.80
01026154-3-B	17.82	01026147-2-B	23.69
01026156-1-B	16.30	01026155-3-B	20.47
01026159-3-B	16.75	01026157-2-B	17.58
01026241-2-B	15.89	01026160-3-B	20.89
01026243-1-B	21.52	01026251-2-B	18.51
01026249-1-B	12.22	01026251-3-B	22.04
01026251-1-B	12.64	01026257-3-B	18.99
01026254-1-B	13.77	01026258-2-B	19.18
Average strength (MPa)	16.31	Average strength (MPa)	19.18

2.3 Calculation of radial displacement for indirect tensile splitting ("Brazilian") test

In this Appendix Section the radical displacement is calculated for indirect tensile splitting ("Brazilian") tests according to Jaeger and Cook, 1979, Section 10.7, equations (15) and (16), and according to an exact (closed form) solution derived in parallel with the formula (16) of section 10.6 of Jaeger and Cook (1979).

2.3.1. Introduction

The immediate objective of this analysis is to implement a method for calculating the radial displacements (which can readily be converted into diameter changes) of a specimen tested in tensile splitting ("Brazilian") test. The ultimate objective is to evaluate whether it might be possible to calculate the elastic properties of the rock tested from measurements of diameter changes. If such determination were possible, it would greatly expand the data base obtained of elastic properties of the rock tested.

2.3.2. Procedures

(1) Use Section 10.7, formula (15) in reference to calculate the displacements when $\theta = 0$, 45, 90, 135, 180, 215, 270, 315 degrees. The following parameters were adopted: Specimen radius R = 30.48mm, thickness t = 25mm, contact angle $2\alpha = 12$ degrees, load P = 50kN; Material properties: E = 35000MPa, $\upsilon = 0.16$. The first 30 terms of the infinite series were used to calculate the displacements.

(2) Use Section 10.7, formula (16) in Jaeger and Cook (1979) to calculate the results when $\theta = 90, 270$ degrees, then compared with the results in procedure (1).

(3) Use an exact formula derived in parallel to formulas (16) and (17) in Section 10.6 in Jaeger and Cook (1979) to calculate the results when $\theta = 0$, 90,180 and 270 degrees, then compare with the results in procedure (1).

The derived formula is:
If $\theta=0$, 180, then:

$$\frac{2\pi G u_r}{Rp} = \alpha(\chi - 1) + \chi\left[\frac{\pi}{2} - \alpha - \frac{\pi}{2}\cos\alpha + \sin\alpha \ln(\cot\frac{\alpha}{2})\right] + \frac{\pi}{2}\cos\alpha + \sin\alpha\ln(\cot\frac{\alpha}{2}) - \frac{\pi}{2} + \alpha$$

If $\theta = 90, 270$, then:

$$\frac{2\pi G u_r}{Rp} = \alpha(\chi - 1) - \chi\left[\alpha - \frac{\pi}{2}\sin\alpha + \cos\alpha\ln(\sec\alpha + \tan\alpha)\right] - \frac{\pi}{2}\sin\alpha - \cos\alpha\ln(\sec\alpha + \tan\alpha) + \alpha$$

(4) Use Section 10.7, formula (15) and derived formula to calculate the displacement of Specimen 01026209-6-B, then compared with the test result. Specimen characters: R = 22.48 mm, t = 24.98 mm, contact angle 2α = 16.514 degrees. The same material properties were adopted as for procedure (1).

2.3.3. Calculation Results

See tables/figures 2.3.1 through 2.3.14.

2.3.4. Conclusions and Discussion

1) In general, using the first 20-30 terms of infinite series in Section 10.7 formula (15) gives results having good agreement with the simplified and exact formulas.

2) The derived formula was verified using different α values, and the differences from the results calculated by formula (15) are less than 0.76%.

3) The computation result for specimen 01026209-6-B is much different from the test data. Possible causes are as follows:

   - All formulas are derived in linear elastic condition, but in test the specimen (force-displacement) shows strong non-linear character.

   - The load was taken as the uniform pressure, but in real contact problems, its distribution is very complicated.

   - Young's Modulus, Poisson's Ratio and contact angle 2α are all approximation.

   - Test result includes the deformation of the test machine.

   - The formulas are derived assuming linear elastic isotropic behavior. It is possible that the Young's modulus in tension is smaller than the Young's modulus in compression, and hence that the actual behavior is anisotropic.

Table / Fig. 2.3.1

$\theta=0^0$, $\alpha=6^0$						
Constants &Assumptions						
R (mm)	30.48	**υ**	0.16	**G (MPa)**	15086.2069	
χ	2.4482759	**P (N)**	50000	**t (mm)**	25	
α (degree)	6	**α (rad)**	0.104719755	**w (mm)**	6.383716272	
p (MPa)	313.29713	**θ (rad)**	0	**α(x −1)**	0.151663094	
Rp/2πG	0.1007422	**θ (degree**	0	**E (MPa)**	35000	
Calculation						
m	**cos2mθ**	**sin2mα**	**x Σ cos2mθ*sin2mα/(m*(2m+1))**	**Σ cos2mθ*sin2mα/(m*(2m-1))**	**sum of all m-terms**	**ur (mm)**
1	1	0.207912	0.169675058	0.207911691	0.377586749	0.053317796
2	1	0.406737	0.269255409	0.275701131	0.54495654	0.070178998
3	1	0.587785	0.337782096	0.314886815	0.652668911	0.08103018
4	1	0.743145	0.388321639	0.341427701	0.729749341	0.088795433
5	1	0.866025	0.426871986	0.36067271	0.787544697	0.094617864
6	1	0.951057	0.456723893	0.375082658	0.83180655	0.099076901
7	1	0.994522	0.479913073	0.38601147	0.865924543	0.102514023
8	1	0.994522	0.497816485	0.394299152	0.892115637	0.105152571
9	1	0.951057	0.511433144	0.400515208	0.911948352	0.107150563
10	1	0.866025	0.521529663	0.405073236	0.9266029	0.108626894
11	1	0.743145	0.528721061	0.408290313	0.937011374	0.109675467
12	1	0.587785	0.533517929	0.41041997	0.943937899	0.11037326
13	1	0.406737	0.536354976	0.411671467	0.948026443	0.110785149
14	1	0.207912	0.537608733	0.412221498	0.949830231	0.110966867
15	1	1.23E-16	0.537608733	0.412221498	0.949830231	0.110966867
16	1	-0.20791	0.53664467	0.411802322	0.948446991	0.110827516
17	1	-0.40674	0.53497105	0.411077301	0.946048351	0.110585872
18	1	-0.58779	0.532810299	0.410144308	0.942954607	0.110274201
19	1	-0.74314	0.530354937	0.409087203	0.93944214	0.109920348
20	1	-0.86603	0.527769243	0.407976914	0.935746157	0.109548006
21	1	-0.95106	0.525190673	0.406872319	0.932062992	0.109176956
22	1	-0.99452	0.522731214	0.405821027	0.928552241	0.108823275
23	1	-0.99452	0.520478796	0.404860137	0.925338933	0.108499559
24	1	-0.95106	0.518498822	0.404017002	0.922515824	0.108215153
25	1	-0.86603	0.516835866	0.403310042	0.920145908	0.107976403
26	1	-0.74314	0.51551553	0.402749601	0.918265131	0.107786929
27	1	-0.58779	0.514546466	0.40233885	0.916885315	0.107647923
28	1	-0.40674	0.513922529	0.402074735	0.915997264	0.107558459
29	1	-0.20791	0.513625027	0.401948957	0.915573984	0.107515817
30	1	-2.5E-16	0.513625027	0.401948957	0.915573984	0.107515817
Formula result			0.108328163	**Difference (%)**		0.755559304

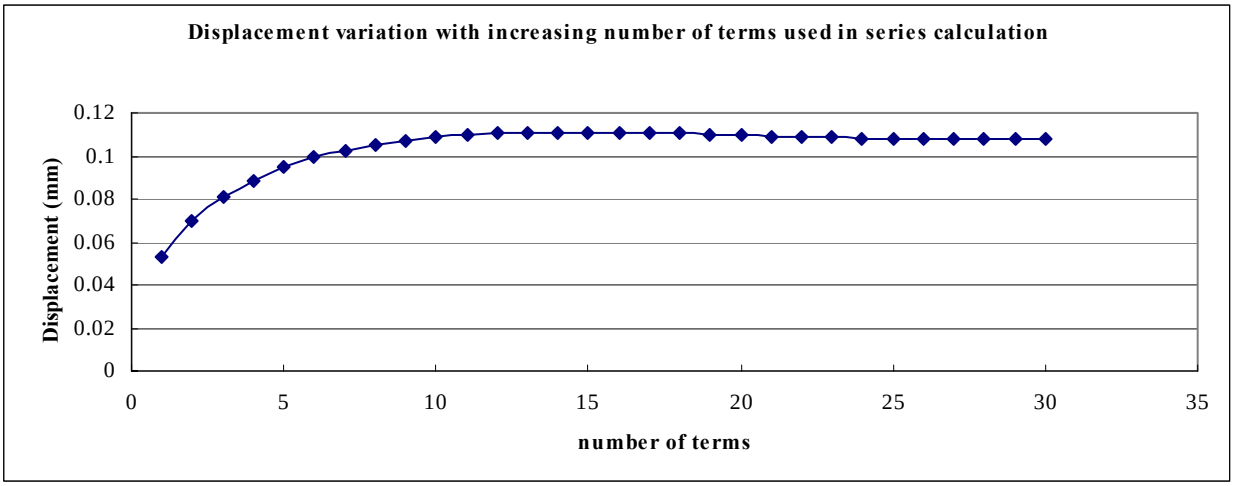

Table / Fig. 2.3.2

$\theta=0^0$, $\alpha=8^0$						
Constants &Assumptions						
R (mm)	30.48	**υ**	0.16	**G (MPa)**	15086.2069	
χ	2.4482759	**P (N)**	50000	**t (mm)**	25	
α (degree)	8	**α (rad)**	0.13962634	**w (mm)**	8.511621696	
p (MPa)	234.97285	**θ (rad)**	0	**α(x –1)**	0.202217458	
Rp/2πG	0.0755567	**θ (degree)**	0	**E (MPa)**	35000	
Calculation						
m	**cos2mθ**	**sin2mα**	**x Σ cos2mθ*sin2mα/(m*(2m+1))**	**Σ cos2mθ*sin2mα/(m*(2m-1))**	**sum of all m-terms**	**ur (mm)**
1	1	0.275637	0.224945428	0.275637356	0.500582784	0.053101235
2	1	0.529919	0.354684283	0.363957233	0.718641516	0.069577023
3	1	0.743145	0.441323499	0.413500222	0.85482372	0.079866495
4	1	0.898794	0.502448381	0.445600009	0.94804839	0.086910239
5	1	0.984808	0.546286219	0.467484626	1.013770844	0.091876008
6	1	0.994522	0.577502423	0.482553139	1.060055562	0.095373126
7	1	0.927184	0.599121488	0.492741973	1.091863461	0.097776424
8	1	0.788011	0.61330728	0.499308729	1.112616009	0.099344417
9	1	0.587785	0.621722838	0.503150463	1.124873301	0.100270537
10	1	0.34202	0.625710265	0.504950569	1.130660834	0.100707824
11	1	0.069756	0.626385297	0.505252545	1.131637842	0.100781644
12	1	-0.207912	0.624688547	0.504499242	1.129187788	0.100596526
13	1	-0.469472	0.621413915	0.503054714	1.124468628	0.100239962
14	1	-0.694658	0.617224961	0.501216993	1.118441954	0.099784606
15	1	-0.866025	0.612665242	0.49922613	1.111891372	0.099289666
16	1	-0.970296	0.608166091	0.497269889	1.10543598	0.098801919
17	1	-0.999391	0.604053849	0.495488443	1.099542292	0.098356611
18	1	-0.951057	0.600557679	0.49397883	1.094536509	0.097978391
19	1	-0.829038	0.597818526	0.492799545	1.090618071	0.097682327
20	1	-0.642788	0.595899353	0.491975458	1.087874811	0.097475055
21	1	-0.406737	0.594796581	0.491503058	1.086299639	0.097356041
22	1	-0.139173	0.594452405	0.49135594	1.085808345	0.09731892
23	1	0.139173	0.594767608	0.491490407	1.086258015	0.097352896
24	1	0.406737	0.59561438	0.491850989	1.087465369	0.097444119
25	1	0.642788	0.596848671	0.492375714	1.089224385	0.097577025
26	1	0.829038	0.598321612	0.493000931	1.091322542	0.097735554
27	1	0.951057	0.599889591	0.49366554	1.093555131	0.097904241
28	1	0.999391	0.601422664	0.494314495	1.095737159	0.098069108
29	1	0.970296	0.602811063	0.494901486	1.097712549	0.098218362
30	1	0.866025	0.60396968	0.495390766	1.099360446	0.098342871
Formula result			0.09813599	**Difference (%)**		-0.210367639

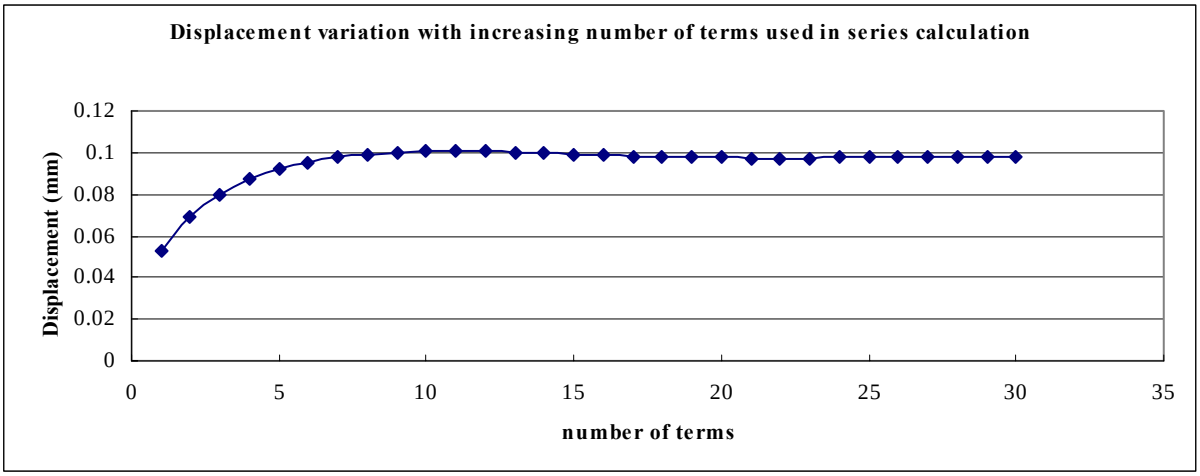

Table / Fig. 2.3.3

$\theta=0^0$, $\alpha=10^0$						
Constants &Assumptions						
R (mm)	30.48	**υ**	0.16	**G (MPa)**	15086.2069	
χ	2.4482759	**P (N)**	50000	**t (mm)**	25	
α (degree)	10	**α (rad)**	0.174532925	**w (mm)**	10.63952712	
p (MPa)	187.97828	**θ (rad)**	0	**α(x –1)**	0.252771823	
Rp/2πG	0.0604453	**θ (degree)**	0	**E (MPa)**	35000	
Calculation						
m	**cos2mθ**	**sin2mα**	**x Σ cos2mθ*sin2mα/(m*(2m+1))**	**Σ cos2mθ*sin2mα/(m*(2m-1))**	**sum of all m-terms**	**ur (mm)**
1	1	0.34202	0.279119887	0.342020143	0.62114003	0.052823884
2	1	0.642788	0.436492026	0.449151412	0.885643438	0.068811878
3	1	0.866025	0.537457221	0.506886439	1.044343659	0.078404565
4	1	0.984808	0.604431694	0.542058144	1.146489838	0.084578823
5	1	0.984808	0.648269532	0.563942761	1.212212292	0.088551438
6	1	0.866025	0.675452469	0.577064358	1.252516827	0.090987659
7	1	0.642788	0.690440292	0.584127958	1.274568249	0.092320564
8	1	0.34202	0.696597348	0.586978126	1.283575474	0.092865009
9	1	1.23E-16	0.696597348	0.586978126	1.283575474	0.092865009
10	1	-0.34202	0.692609921	0.58517802	1.277787941	0.09251518
11	1	-0.642788	0.686389678	0.582395389	1.268785068	0.091970998
12	1	-0.866025	0.679322115	0.579257616	1.258579731	0.091354133
13	1	-0.984808	0.672452938	0.576227438	1.248680376	0.090755764
14	1	-0.984808	0.666514315	0.573622127	1.240136442	0.090239323
15	1	-0.866025	0.661954596	0.571631264	1.23358586	0.089843371
16	1	-0.642788	0.658974063	0.570335321	1.229309384	0.089584878
17	1	-0.34202	0.657566736	0.56972566	1.227292396	0.08946296
18	1	-2.45E-16	0.657566736	0.56972566	1.227292396	0.08946296
19	1	0.34202	0.658696776	0.570212175	1.228908951	0.089560673
20	1	0.642788	0.660615949	0.571036261	1.23165221	0.089726491
21	1	0.866025	0.662963976	0.572042098	1.235006074	0.089929216
22	1	0.984808	0.665399412	0.573083121	1.238482533	0.090139352
23	1	0.984808	0.667629829	0.574034626	1.241664455	0.090331684
24	1	0.866025	0.669432779	0.574802379	1.244235158	0.090487071
25	1	0.642788	0.67066707	0.575327104	1.245994174	0.090593395
26	1	0.34202	0.671274733	0.575585038	1.246859771	0.090645716
27	1	3.68E-16	0.671274733	0.575585038	1.246859771	0.090645716
28	1	-0.34202	0.670750072	0.575362947	1.246113018	0.090600579
29	1	-0.642788	0.669830305	0.574974085	1.24480439	0.090521478
30	1	-0.866025	0.668671688	0.574484805	1.243156493	0.090421871
Formula result			0.09026624	**Difference (%)**		-0.172116674

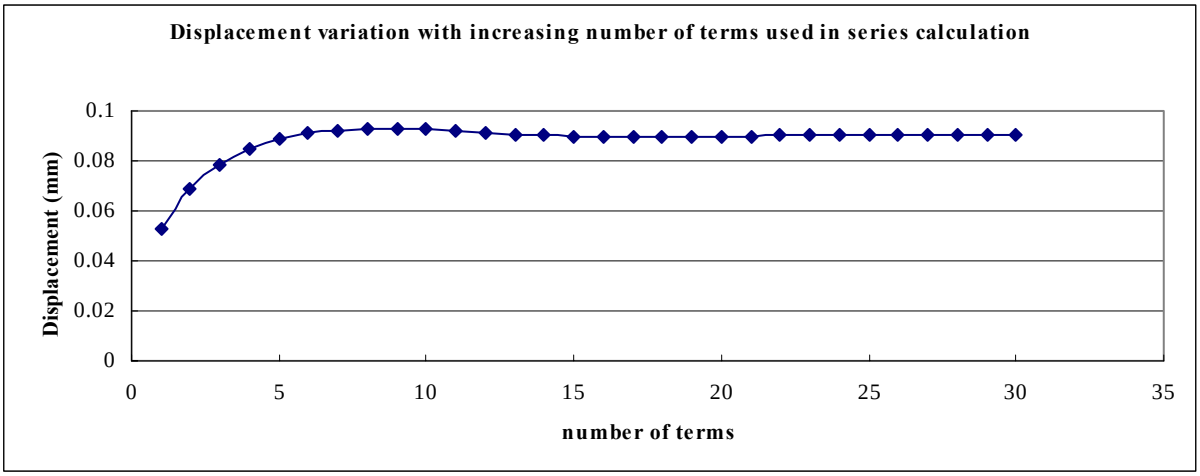

Table / Fig. 2.3.4

$\theta=0^0$, $\alpha=12^0$						
Constants &Assumptions						
R (mm)	30.48	**υ**	0.16	**G (MPa)**	15086.2069	
χ	2.4482759	**P (N)**	50000	**t (mm)**	25	
α (degree)	12	**α (rad)**	0.20943951	**w (mm)**	12.76743254	
p (MPa)	156.64857	**θ (rad)**	0	**α(x –1)**	0.303326187	
Rp/2πG	0.0503711	**θ (degree)**	0	**E (MPa)**	35000	
Calculation						
m	**cos2mθ**	**sin2mα**	**x Σ cos2mθ*sin2mα/(m*(2m+1))**	**Σ cos2mθ*sin2mα/(m*(2m-1))**	**sum of all m-terms**	**ur (mm)**
1	1	0.406737	0.331934502	0.406736643	0.738671145	0.052486555
2	1	0.743145	0.513876856	0.530594114	1.04447097	0.067890029
3	1	0.951057	0.624755366	0.593997882	1.218753247	0.07666882
4	1	0.994522	0.692390475	0.629516521	1.321906996	0.081864788
5	1	0.866025	0.730940823	0.64876153	1.379702352	0.084776003
6	1	0.587785	0.749390316	0.657667367	1.407057683	0.086153922
7	1	0.207912	0.754238174	0.659952111	1.414190285	0.086513199
8	1	-0.207912	0.750495342	0.658219513	1.408714856	0.086237395
9	1	-0.587785	0.742079784	0.65437778	1.396457564	0.085619982
10	1	-0.866025	0.731983265	0.649819751	1.381803016	0.084881816
11	1	-0.994522	0.722359296	0.645514462	1.367873758	0.084180184
12	1	-0.951057	0.714597801	0.642068605	1.356666405	0.083615657
13	1	-0.743145	0.709414258	0.639782005	1.349196263	0.083239378
14	1	-0.406737	0.70696154	0.638705982	1.345667522	0.083061632
15	1	-2.45E-16	0.70696154	0.638705982	1.345667522	0.083061632
16	1	0.406737	0.708847531	0.639526016	1.348373547	0.083197937
17	1	0.743145	0.711905386	0.640850695	1.352756081	0.08341869
18	1	0.951057	0.715401555	0.642360308	1.357761864	0.083670837
19	1	0.994522	0.718687471	0.643774991	1.362462462	0.083907611
20	1	0.866025	0.721273165	0.64488528	1.366158445	0.084093782
21	1	0.587785	0.722866809	0.645567957	1.368434767	0.084208443
22	1	0.207912	0.723380976	0.645787737	1.369168713	0.084245412
23	1	-0.207912	0.722910093	0.645586856	1.368496949	0.084211575
24	1	-0.587785	0.721686402	0.64506577	1.366752172	0.084123689
25	1	-0.866025	0.720023446	0.644358811	1.364382256	0.084004313
26	1	-0.994522	0.718256491	0.643608794	1.361865285	0.083877531
27	1	-0.951057	0.716688512	0.642944184	1.359632696	0.083765073
28	1	-0.743145	0.715548522	0.642461623	1.358010145	0.083683343
29	1	-0.406737	0.714966521	0.642215563	1.357182084	0.083641633
30	1	-4.9E-16	0.714966521	0.642215563	1.357182084	0.083641633
Formula result			0.08385934	**Difference (%)**		0.260286194

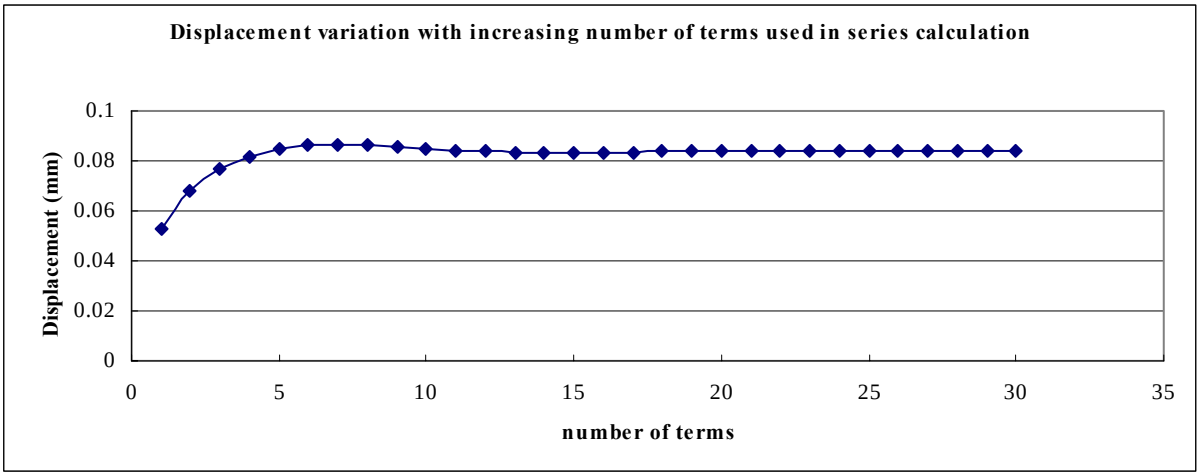

Table / Fig. 2.3.5

$\theta=45^0$, $\alpha=6^0$						
Constants &Assumptions						
R (mm)	30.48	**υ**	0.16	**G (MPa)**	15086.2069	
χ	2.4482759	**P (N)**	50000	**t (mm)**	25	
α (degree)	6	**α (rad)**	0.104719755	**w (mm)**	6.383716272	
p (MPa)	313.29713	**θ (rad)**	0.785398163	**α(x –1)**	0.151663094	
Rp/2πG	0.1007422	**θ (degree)**	45	**E (MPa)**	35000	
Calculation						
m	**cos2mθ**	**sin2mα**	**x Σ cos2mθ*sin2mα/(m*(2m+1))**	**Σ cos2mθ*sin2mα/(m*(2m-1))**	**sum of all m-terms**	**ur (mm)**
1	0	0.207912	0	0	0	0.015278875
2	-1	0.406737	-0.099580351	-0.067789441	-0.167369791	-0.001582327
3	0	0.587785	-0.099580351	-0.067789441	-0.167369791	-0.001582327
4	1	0.743145	-0.049040808	-0.041248554	-0.090289362	0.006182925
5	0	0.866025	-0.049040808	-0.041248554	-0.090289362	0.006182925
6	-1	0.951057	-0.078892714	-0.055658501	-0.134551215	0.001723888
7	0	0.994522	-0.078892714	-0.055658501	-0.134551215	0.001723888
8	1	0.994522	-0.060989303	-0.047370819	-0.108360122	0.004362437
9	0	0.951057	-0.060989303	-0.047370819	-0.108360122	0.004362437
10	-1	0.866025	-0.071085822	-0.051928847	-0.12301467	0.002886105
11	0	0.743145	-0.071085822	-0.051928847	-0.12301467	0.002886105
12	1	0.587785	-0.066288954	-0.04979919	-0.116088145	0.003583899
13	0	0.406737	-0.066288954	-0.04979919	-0.116088145	0.003583899
14	-1	0.207912	-0.067542711	-0.050349221	-0.117891932	0.003402181
15	0	1.23E-16	-0.067542711	-0.050349221	-0.117891932	0.003402181
16	1	-0.207912	-0.068506774	-0.050768398	-0.119275172	0.003262831
17	0	-0.406737	-0.068506774	-0.050768398	-0.119275172	0.003262831
18	-1	-0.587785	-0.066346022	-0.049835406	-0.116181428	0.003574501
19	0	-0.743145	-0.066346022	-0.049835406	-0.116181428	0.003574501
20	1	-0.866025	-0.068931716	-0.050945695	-0.119877411	0.00320216
21	0	-0.951057	-0.068931716	-0.050945695	-0.119877411	0.00320216
22	-1	-0.994522	-0.066472258	-0.049894403	-0.116366661	0.00355584
23	0	-0.994522	-0.066472258	-0.049894403	-0.116366661	0.00355584
24	1	-0.951057	-0.068452231	-0.050737538	-0.119189769	0.003271434
25	0	-0.866025	-0.068452231	-0.050737538	-0.119189769	0.003271434
26	-1	-0.743145	-0.067131895	-0.050177097	-0.117308992	0.003460908
27	0	-0.587785	-0.067131895	-0.050177097	-0.117308992	0.003460908
28	1	-0.406737	-0.067755832	-0.050441212	-0.118197044	0.003371444
29	0	-0.207912	-0.067755832	-0.050441212	-0.118197044	0.003371444
30	-1	-2.45E-16	-0.067755832	-0.050441212	-0.118197044	0.003371444

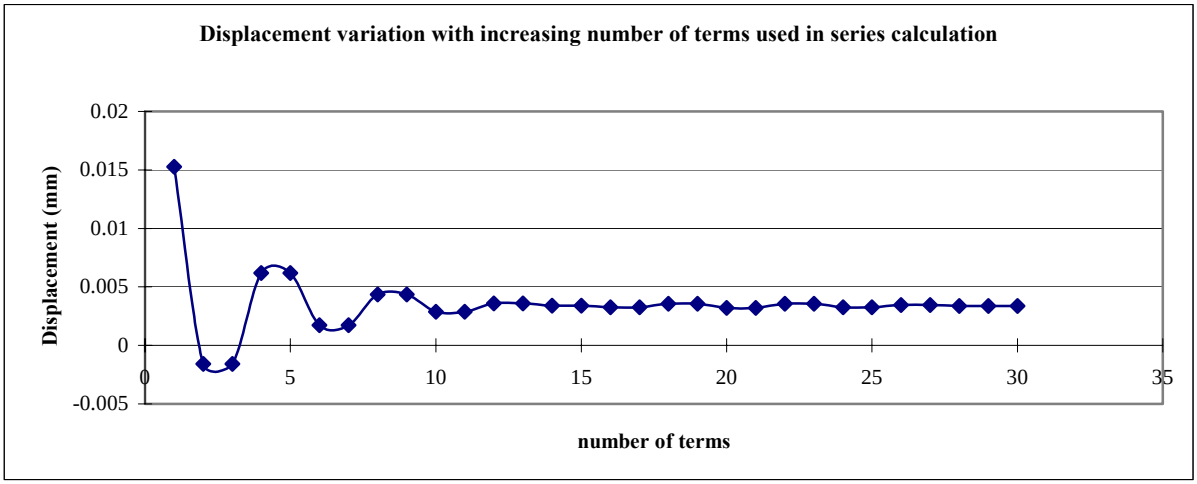

Table / Fig. 2.3.6

$\theta=90^0$, $\alpha=6^0$						
Constants &Assumptions						
R (mm)	30.48	**υ**	0.16	**G (MPa)**	15086.2069	
χ	2.4482759	**P (N)**	50000	**t (mm)**	25	
α (degree)	6	**α (rad)**	0.104719755	**w (mm)**	6.383716272	
p (MPa)	313.29713	**θ (rad)**	1.570796327	**α(x –1)**	0.151663094	
Rp/2πG	0.1007422	**θ (degree)**	90	**E (MPa)**	35000	
Calculation						
m	**cos2mθ**	**sin2mα**	**x Σ cos2mθ*sin2mα/(m*(2m+1))**	**Σ cos2mθ*sin2mα/(m*(2m-1))**	**sum of all m-terms**	**ur (mm)**
1	-1	0.207912	-0.169675058	-0.207911691	-0.377586749	-0.022760047
2	1	0.406737	-0.070094707	-0.14012225	-0.210216958	-0.005898845
3	-1	0.587785	-0.138621395	-0.179307934	-0.317929329	-0.016750027
4	1	0.743145	-0.088081853	-0.152767047	-0.2408489	-0.008984775
5	-1	0.866025	-0.1266322	-0.172012056	-0.298644256	-0.014807206
6	1	0.951057	-0.096780293	-0.157602109	-0.254382402	-0.01034817
7	-1	0.994522	-0.119969474	-0.168530921	-0.288500395	-0.013785291
8	1	0.994522	-0.102066062	-0.160243238	-0.262309301	-0.011146743
9	-1	0.951057	-0.115682721	-0.166459294	-0.282142016	-0.013144734
10	1	0.866025	-0.105586202	-0.161901266	-0.267487468	-0.011668403
11	-1	0.743145	-0.112777599	-0.165118343	-0.277895942	-0.012716976
12	1	0.587785	-0.107980731	-0.162988686	-0.270969417	-0.012019182
13	-1	0.406737	-0.110817778	-0.164240184	-0.275057962	-0.012431071
14	1	0.207912	-0.109564022	-0.163690153	-0.273254174	-0.012249354
15	-1	1.23E-16	-0.109564022	-0.163690153	-0.273254174	-0.012249354
16	1	-0.207912	-0.110528084	-0.164109329	-0.274637414	-0.012388704
17	-1	-0.406737	-0.108854465	-0.163384309	-0.272238774	-0.01214706
18	1	-0.587785	-0.111015216	-0.164317301	-0.275332518	-0.012458731
19	-1	-0.743145	-0.108559854	-0.163260196	-0.27182005	-0.012104877
20	1	-0.866025	-0.111145548	-0.164370485	-0.275516033	-0.012477218
21	-1	-0.951057	-0.108566978	-0.16326589	-0.271832868	-0.012106168
22	1	-0.994522	-0.111026437	-0.164317181	-0.275343618	-0.012459849
23	-1	-0.994522	-0.108774019	-0.163356291	-0.272130309	-0.012136133
24	1	-0.951057	-0.110753992	-0.164199426	-0.274953418	-0.012420539
25	-1	-0.866025	-0.109091036	-0.163492466	-0.272583502	-0.012181789
26	1	-0.743145	-0.110411372	-0.164052907	-0.27446428	-0.012371262
27	-1	-0.587785	-0.109442308	-0.163642156	-0.273084464	-0.012232257
28	1	-0.406737	-0.110066245	-0.163906271	-0.273972516	-0.012321721
29	-1	-0.207912	-0.109768743	-0.163780492	-0.273549236	-0.012279079
30	1	-2.45E-16	-0.109768743	-0.163780492	-0.273549236	-0.012279079
Simplified formula result			-0.012378273	**Difference (%)**		0.807828779
Formula result			-0.012289136	**Difference (%)**		0.081904969

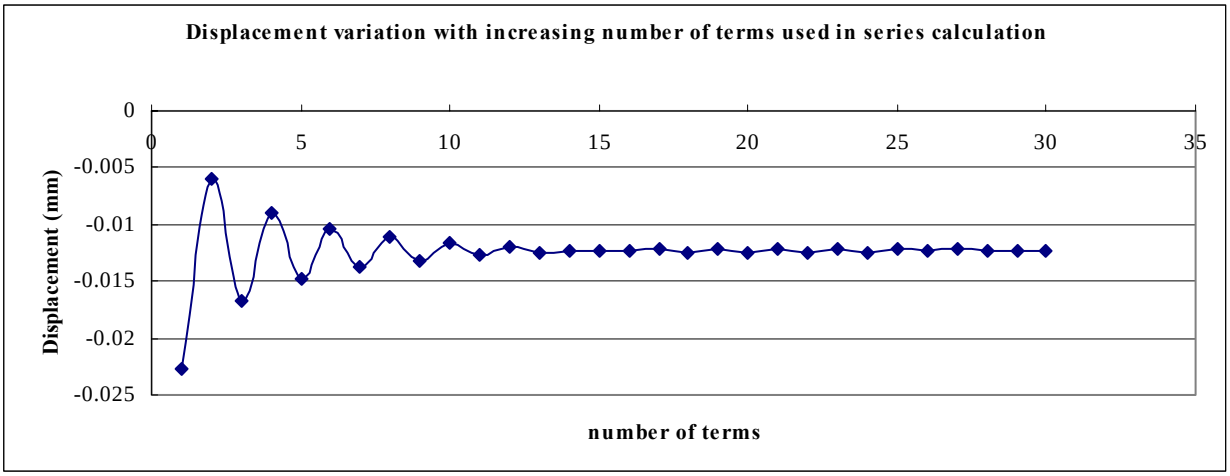

Table / Fig. 2.3.7

$\theta=90^0$, $\alpha=8^0$						
Constants &Assumptions						
R (mm)	30.48	**υ**	0.16	**G (MPa)**	15086.2069	
χ	2.4482759	**P (N)**	50000	**t (mm)**	25	
α (degree)	8	**α (rad)**	0.13962634	**w (mm)**	8.511621696	
p (MPa)	234.97285	**θ (rad)**	1.570796327	**α(x –1)**	0.202217458	
Rp/2πG	0.0755567	**θ (degree)**	90	**E (MPa)**	35000	
Calculation						
m	**cos2mθ**	**sin2mα**	**x Σ cos2mθ*sin2mα/(m*(2m+1))**	**Σ cos2mθ*sin2mα/(m*(2m-1))**	**sum of all m-terms**	**ur (mm)**
1	-1	0.275637	-0.224945428	-0.275637356	-0.500582784	-0.022543486
2	1	0.529919	-0.095206574	-0.187317478	-0.282524052	-0.006067698
3	-1	0.743145	-0.18184579	-0.236860467	-0.418706257	-0.016357169
4	1	0.898794	-0.120720908	-0.204760679	-0.325481587	-0.009313425
5	-1	0.984808	-0.164558745	-0.226645296	-0.391204041	-0.014279194
6	1	0.994522	-0.13334254	-0.211576783	-0.344919323	-0.010782075
7	-1	0.927184	-0.154961606	-0.221765616	-0.376727222	-0.013185374
8	1	0.788011	-0.140775814	-0.21519886	-0.355974674	-0.011617381
9	-1	0.587785	-0.149191372	-0.219040594	-0.368231965	-0.012543501
10	1	0.34202	-0.145203945	-0.217240488	-0.362444432	-0.012106214
11	-1	0.069756	-0.145878977	-0.217542464	-0.36342144	-0.012180034
12	1	-0.207912	-0.147575727	-0.218295767	-0.365871494	-0.012365151
13	-1	-0.469472	-0.144301095	-0.216851239	-0.361152334	-0.012008587
14	1	-0.694658	-0.148490049	-0.21868896	-0.367179009	-0.012463943
15	-1	-0.866025	-0.143930331	-0.216698097	-0.360628427	-0.011969003
16	1	-0.970296	-0.148429482	-0.218654338	-0.367083819	-0.012456751
17	-1	-0.999391	-0.144317239	-0.216872893	-0.361190131	-0.012011443
18	1	-0.951057	-0.147813408	-0.218382506	-0.366195914	-0.012389663
19	-1	-0.829038	-0.145074255	-0.217203221	-0.362277475	-0.012093599
20	1	-0.642788	-0.146993427	-0.218027307	-0.365020735	-0.012300871
21	-1	-0.406737	-0.145890655	-0.217554907	-0.363445562	-0.012181856
22	1	-0.139173	-0.146234831	-0.217702025	-0.363936855	-0.012218977
23	-1	0.139173	-0.146550033	-0.217836491	-0.364386525	-0.012252952
24	1	0.406737	-0.145703262	-0.217475909	-0.363179171	-0.012161728
25	-1	0.642788	-0.146937553	-0.218000634	-0.364938187	-0.012294634
26	1	0.829038	-0.145464612	-0.217375417	-0.362840029	-0.012136104
27	-1	0.951057	-0.147032591	-0.218040027	-0.365072617	-0.012304791
28	1	0.999391	-0.145499518	-0.217391072	-0.362890589	-0.012139924
29	-1	0.970296	-0.146887917	-0.217978062	-0.36486598	-0.012289178
30	1	0.866025	-0.1457293	-0.217488782	-0.363218083	-0.012164669
Simplified formula result			-0.012378273	**Difference (%)**		1.755939328
Formula result			-0.012219774	**Difference (%)**		0.452992477

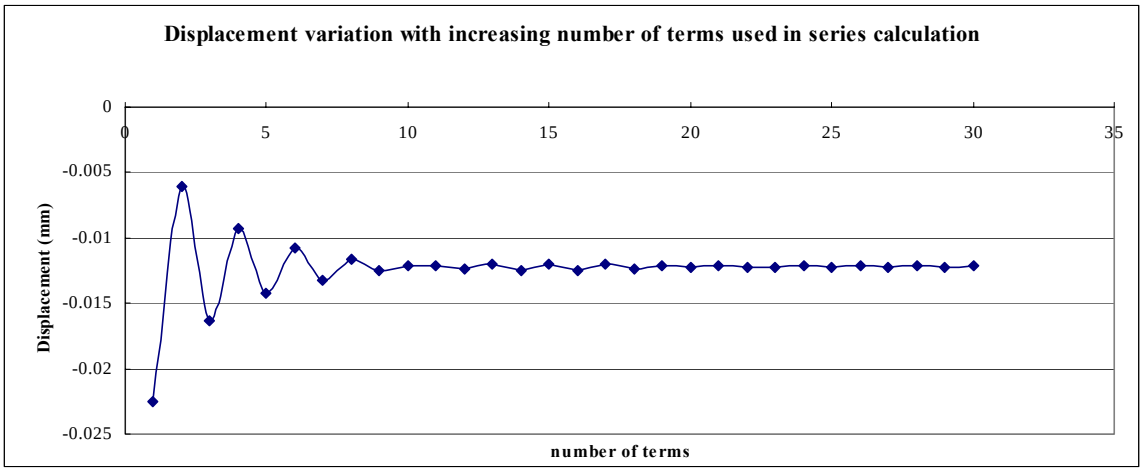

Table / Fig. 2.3.8

$\theta=90^0$, $\alpha=10^0$						
Constants &Assumptions						
R (mm)	30.48	**υ**	0.16	**G (MPa)**	15086.2069	
χ	2.4482759	**P (N)**	50000	**t (mm)**	25	
α (degree)	10	**α (rad)**	0.174532925	**w (mm)**	10.63952712	
p (MPa)	187.97828	**θ (rad)**	1.570796327	**α(x –1)**	0.252771823	
Rp/2πG	0.0604453	**θ (degree)**	90	**E (MPa)**	35000	
Calculation						
m	**cos2mθ**	**sin2mα**	**x Σ cos2mθ*sin2mα/(m*(2m+1))**	**Σ cos2mθ*sin2mα/(m*(2m-1))**	**sum of all m-terms**	**ur (mm)**
1	-1	0.34202	-0.279119887	-0.342020143	-0.62114003	-0.022266135
2	1	0.642788	-0.121747748	-0.234888875	-0.356636623	-0.006278141
3	-1	0.866025	-0.222712943	-0.292623902	-0.515336845	-0.015870828
4	1	0.984808	-0.155738469	-0.257452196	-0.413190666	-0.009696569
5	-1	0.984808	-0.199576307	-0.279336813	-0.47891312	-0.013669184
6	1	0.866025	-0.17239337	-0.266215216	-0.438608586	-0.011232963
7	-1	0.642788	-0.187381192	-0.273278816	-0.460660009	-0.012565869
8	1	0.34202	-0.181224136	-0.270428648	-0.451652784	-0.012021424
9	-1	1.23E-16	-0.181224136	-0.270428648	-0.451652784	-0.012021424
10	1	-0.34202	-0.185211563	-0.272228754	-0.457440317	-0.012371253
11	-1	-0.642788	-0.17899132	-0.269446124	-0.448437444	-0.011827072
12	1	-0.866025	-0.186058884	-0.272583897	-0.458642781	-0.012443937
13	-1	-0.984808	-0.179189707	-0.26955372	-0.448743427	-0.011845567
14	1	-0.984808	-0.18512833	-0.272159031	-0.457287362	-0.012362008
15	-1	-0.866025	-0.180568612	-0.270168168	-0.45073678	-0.011966056
16	1	-0.642788	-0.183549145	-0.271464111	-0.455013256	-0.012224549
17	-1	-0.34202	-0.182141818	-0.270854449	-0.452996267	-0.012102631
18	1	-2.45E-16	-0.182141818	-0.270854449	-0.452996267	-0.012102631
19	-1	0.34202	-0.183271858	-0.271340964	-0.454612822	-0.012200344
20	1	0.642788	-0.181352685	-0.270516878	-0.451869563	-0.012034527
21	-1	0.866025	-0.183700713	-0.271522714	-0.455223428	-0.012237253
22	1	0.984808	-0.181265278	-0.270481692	-0.451746969	-0.012027117
23	-1	0.984808	-0.183495695	-0.271433197	-0.454928892	-0.012219449
24	1	0.866025	-0.181692745	-0.270665444	-0.452358189	-0.012064062
25	-1	0.642788	-0.182927036	-0.271190168	-0.454117205	-0.012170387
26	1	0.34202	-0.182319373	-0.270932234	-0.453251608	-0.012118065
27	-1	3.68E-16	-0.182319373	-0.270932234	-0.453251608	-0.012118065
28	1	-0.34202	-0.182844035	-0.271154325	-0.45399836	-0.012163203
29	-1	-0.642788	-0.181924268	-0.270765464	-0.452689732	-0.012084103
30	1	-0.866025	-0.183082885	-0.271254744	-0.454337629	-0.01218371
Simplified formula result			-0.012378273	**Difference (%)**		1.596905965
Formula result			-0.012130549	**Difference (%)**		-0.436330329

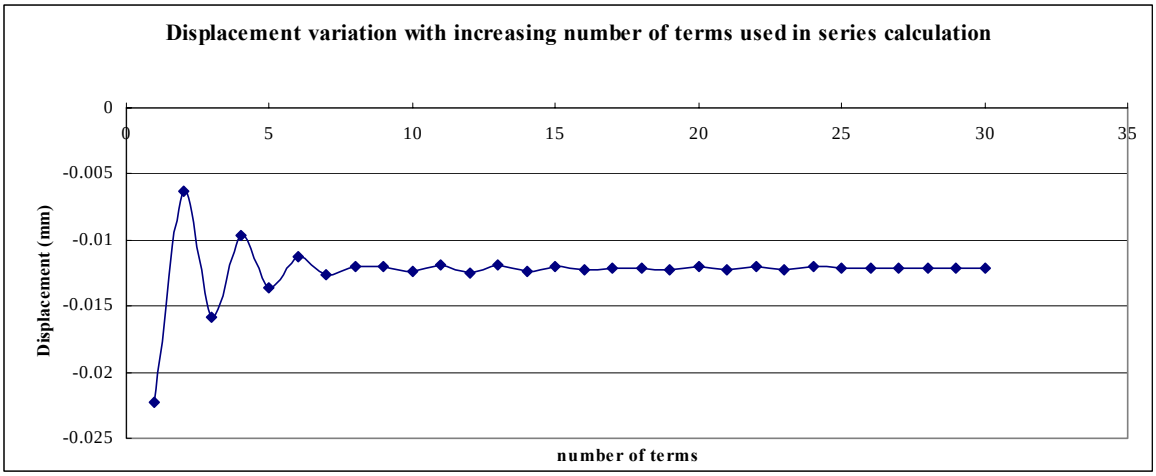

Table / Fig. 2.3.9

$\theta=90^0$, $\alpha=12^0$						
Constants &Assumptions						
R (mm)	30.48	**υ**	0.16	**G (MPa)**	15086.2069	
χ	2.4482759	**P (N)**	50000	**t (mm)**	25	
α (degree)	12	**α (rad)**	0.20943951	**w (mm)**	12.76743254	
p (MPa)	156.64857	**θ (rad)**	1.570796327	**α(x –1)**	0.303326187	
Rp/2πG	0.0503711	**θ (degree)**	90	**E (MPa)**	35000	
Calculation						
m	**cos2mθ**	**sin2mα**	**x Σ cos2mθ*sin2mα/(m*(2m+1))**	**Σ cos2mθ*sin2mα/(m*(2m-1))**	**sum of all m-terms**	**ur (mm)**
1	-1	0.406737	-0.331934502	-0.406736643	-0.738671145	-0.021928806
2	1	0.743145	-0.149992148	-0.282879172	-0.43287132	-0.006525331
3	-1	0.951057	-0.260870658	-0.34628294	-0.607153598	-0.015304122
4	1	0.994522	-0.193235548	-0.310764301	-0.503999849	-0.010108154
5	-1	0.866025	-0.231785895	-0.33000931	-0.561795205	-0.013019369
6	1	0.587785	-0.213336403	-0.321103473	-0.534439875	-0.011641451
7	-1	0.207912	-0.218184261	-0.323388216	-0.541572478	-0.012000728
8	1	-0.207912	-0.221927094	-0.325120814	-0.547047907	-0.012276532
9	-1	-0.587785	-0.213511535	-0.32127908	-0.534790616	-0.011659118
10	1	-0.866025	-0.223608055	-0.325837109	-0.549445164	-0.012397284
11	-1	-0.994522	-0.213984087	-0.321531819	-0.535515906	-0.011695652
12	1	-0.951057	-0.221745582	-0.324977676	-0.546723258	-0.012260179
13	-1	-0.743145	-0.21656204	-0.322691077	-0.539253116	-0.0118839
14	1	-0.406737	-0.219014758	-0.323767099	-0.542781857	-0.012061646
15	-1	-2.45E-16	-0.219014758	-0.323767099	-0.542781857	-0.012061646
16	1	0.406737	-0.217128766	-0.322947066	-0.540075832	-0.011925341
17	-1	0.743145	-0.220186621	-0.324271745	-0.544458365	-0.012146094
18	1	0.951057	-0.216690452	-0.322762131	-0.539452583	-0.011893947
19	-1	0.994522	-0.219976368	-0.324176814	-0.544153182	-0.012130721
20	1	0.866025	-0.217390674	-0.323066525	-0.540457199	-0.011944551
21	-1	0.587785	-0.218984318	-0.323749202	-0.54273352	-0.012059211
22	1	0.207912	-0.218470151	-0.323529422	-0.541999573	-0.012022242
23	-1	-0.207912	-0.217999267	-0.323328542	-0.541327809	-0.011988404
24	1	-0.587785	-0.219222958	-0.323849628	-0.543072586	-0.01207629
25	-1	-0.866025	-0.217560002	-0.323142668	-0.54070267	-0.011956915
26	1	-0.994522	-0.219326957	-0.323892685	-0.543219642	-0.012083698
27	-1	-0.951057	-0.217758978	-0.323228075	-0.540987053	-0.01197124
28	1	-0.743145	-0.218898968	-0.323710637	-0.542609604	-0.01205297
29	-1	-0.406737	-0.218316967	-0.323464577	-0.541781544	-0.012011259
30	1	-4.9E-16	-0.218316967	-0.323464577	-0.541781544	-0.012011259
Simplified formula result			-0.012378273	**Difference (%)**		3.05557844
Formula result			-0.012021428	**Difference (%)**		0.084661789

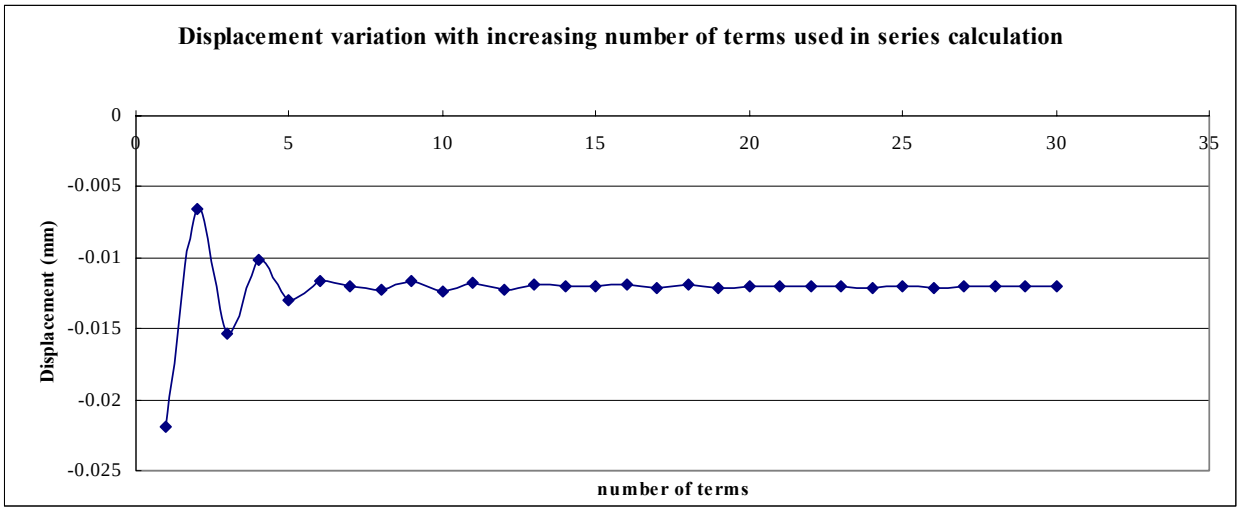

Table / Fig. 2.3.10

$\theta=135^0$, $\alpha=6^0$						
Constants &Assumptions						
R (mm)	30.48	**υ**	0.16	**G (MPa)**	15086.2069	
χ	2.4482759	**P (N)**	50000	**t (mm)**	25	
α (degree)	6	**α (rad)**	0.104719755	**w (mm)**	6.383716272	
p (MPa)	313.29713	**θ (rad)**	2.35619449	**α(x –1)**	0.151663094	
Rp/2πG	0.1007422	**θ (degree)**	135	**E (MPa)**	35000	
Calculation						
m	**cos2mθ**	**sin2mα**	**x Σ cos2mθ*sin2mα/(m*(2m+1))**	**Σ cos2mθ*sin2mα/(m*(2m-1))**	**sum of all m-terms**	**ur (mm)**
1	0	0.207912	0	0	0	0.015278875
2	-1	0.406737	-0.099580351	-0.067789441	-0.167369791	-0.001582327
3	0	0.587785	-0.099580351	-0.067789441	-0.167369791	-0.001582327
4	1	0.743145	-0.049040808	-0.041248554	-0.090289362	0.006182925
5	0	0.866025	-0.049040808	-0.041248554	-0.090289362	0.006182925
6	-1	0.951057	-0.078892714	-0.055658501	-0.134551215	0.001723888
7	0	0.994522	-0.078892714	-0.055658501	-0.134551215	0.001723888
8	1	0.994522	-0.060989303	-0.047370819	-0.108360122	0.004362437
9	0	0.951057	-0.060989303	-0.047370819	-0.108360122	0.004362437
10	-1	0.866025	-0.071085822	-0.051928847	-0.12301467	0.002886105
11	0	0.743145	-0.071085822	-0.051928847	-0.12301467	0.002886105
12	1	0.587785	-0.066288954	-0.04979919	-0.116088145	0.003583899
13	0	0.406737	-0.066288954	-0.04979919	-0.116088145	0.003583899
14	-1	0.207912	-0.067542711	-0.050349221	-0.117891932	0.003402181
15	0	1.23E-16	-0.067542711	-0.050349221	-0.117891932	0.003402181
16	1	-0.207912	-0.068506774	-0.050768398	-0.119275172	0.003262831
17	0	-0.406737	-0.068506774	-0.050768398	-0.119275172	0.003262831
18	-1	-0.587785	-0.066346022	-0.049835406	-0.116181428	0.003574501
19	0	-0.743145	-0.066346022	-0.049835406	-0.116181428	0.003574501
20	1	-0.866025	-0.068931716	-0.050945695	-0.119877411	0.00320216
21	0	-0.951057	-0.068931716	-0.050945695	-0.119877411	0.00320216
22	-1	-0.994522	-0.066472258	-0.049894403	-0.116366661	0.00355584
23	0	-0.994522	-0.066472258	-0.049894403	-0.116366661	0.00355584
24	1	-0.951057	-0.068452231	-0.050737538	-0.119189769	0.003271434
25	0	-0.866025	-0.068452231	-0.050737538	-0.119189769	0.003271434
26	-1	-0.743145	-0.067131895	-0.050177097	-0.117308992	0.003460908
27	0	-0.587785	-0.067131895	-0.050177097	-0.117308992	0.003460908
28	1	-0.406737	-0.067755832	-0.050441212	-0.118197044	0.003371444
29	0	-0.207912	-0.067755832	-0.050441212	-0.118197044	0.003371444
30	-1	-2.45E-16	-0.067755832	-0.050441212	-0.118197044	0.003371444

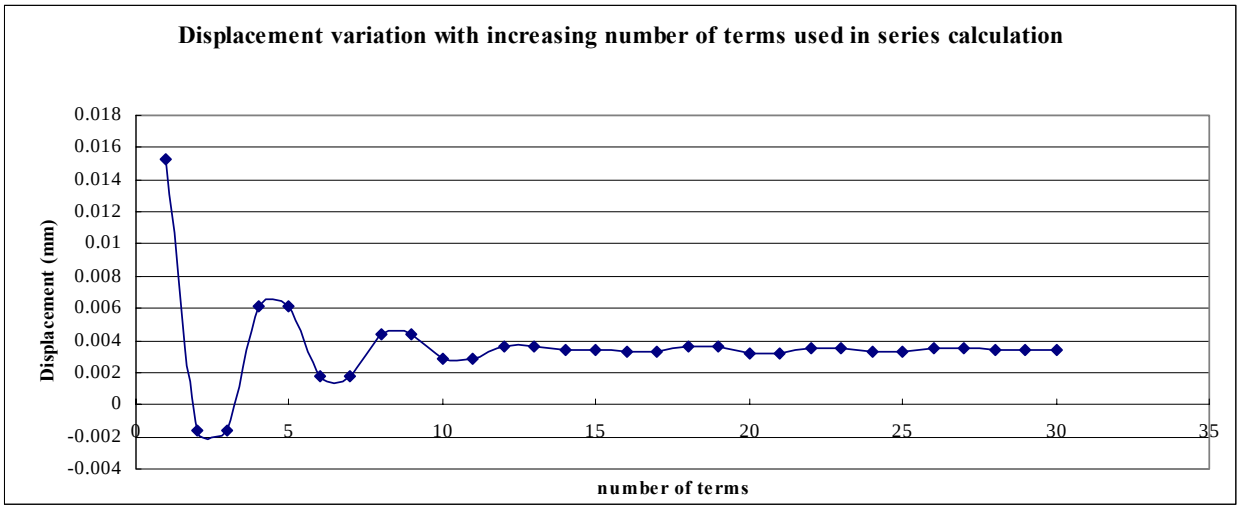

Table / Fig. 2.3.11

$\theta=180^0$, $\alpha=6^0$						
Constants &Assumptions						
R (mm)	30.48	**υ**	0.16	**G (MPa)**	15086.2069	
χ	2.4482759	**P (N)**	50000	**t (mm)**	25	
α (degree)	6	**α (rad)**	0.104719755	**w (mm)**	6.383716272	
p (MPa)	313.29713	**θ (rad)**	3.141592654	**α(x –1)**	0.151663094	
Rp/2πG	0.1007422	**θ (degree)**	180	**E (MPa)**	35000	
Calculation						
m	**cos2mθ**	**sin2mα**	**x Σ cos2mθ*sin2mα/(m*(2m+1))**	**Σ cos2mθ*sin2mα/(m*(2m-1))**	**sum of all m-terms**	**ur (mm)**
1	1	0.207912	0.169675058	0.207911691	0.377586749	0.053317796
2	1	0.406737	0.269255409	0.275701131	0.54495654	0.070178998
3	1	0.587785	0.337782096	0.314886815	0.652668911	0.08103018
4	1	0.743145	0.388321639	0.341427701	0.729749341	0.088795433
5	1	0.866025	0.426871986	0.36067271	0.787544697	0.094617864
6	1	0.951057	0.456723893	0.375082658	0.83180655	0.099076901
7	1	0.994522	0.479913073	0.38601147	0.865924543	0.102514023
8	1	0.994522	0.497816485	0.394299152	0.892115637	0.105152571
9	1	0.951057	0.511433144	0.400515208	0.911948352	0.107150563
10	1	0.866025	0.521529663	0.405073236	0.9266029	0.108626894
11	1	0.743145	0.528721061	0.408290313	0.937011374	0.109675467
12	1	0.587785	0.533517929	0.41041997	0.943937899	0.11037326
13	1	0.406737	0.536354976	0.411671467	0.948026443	0.110785149
14	1	0.207912	0.537608733	0.412221498	0.949830231	0.110966867
15	1	1.23E-16	0.537608733	0.412221498	0.949830231	0.110966867
16	1	-0.207912	0.53664467	0.411802322	0.948446991	0.110827516
17	1	-0.406737	0.53497105	0.411077301	0.946048351	0.110585872
18	1	-0.587785	0.532810299	0.410144308	0.942954607	0.110274201
19	1	-0.743145	0.530354937	0.409087203	0.93944214	0.109920348
20	1	-0.866025	0.527769243	0.407976914	0.935746157	0.109548006
21	1	-0.951057	0.525190673	0.406872319	0.932062992	0.109176956
22	1	-0.994522	0.522731214	0.405821027	0.928552241	0.108823275
23	1	-0.994522	0.520478796	0.404860137	0.925338933	0.108499559
24	1	-0.951057	0.518498822	0.404017002	0.922515824	0.108215153
25	1	-0.866025	0.516835866	0.403310042	0.920145908	0.107976403
26	1	-0.743145	0.51551553	0.402749601	0.918265131	0.107786929
27	1	-0.587785	0.514546466	0.40233885	0.916885315	0.107647923
28	1	-0.406737	0.513922529	0.402074735	0.915997264	0.107558459
29	1	-0.207912	0.513625027	0.401948957	0.915573984	0.107515817
30	1	-2.45E-16	0.513625027	0.401948957	0.915573984	0.107515817
Formula result			0.108328163	**Difference (%)**		0.755559304

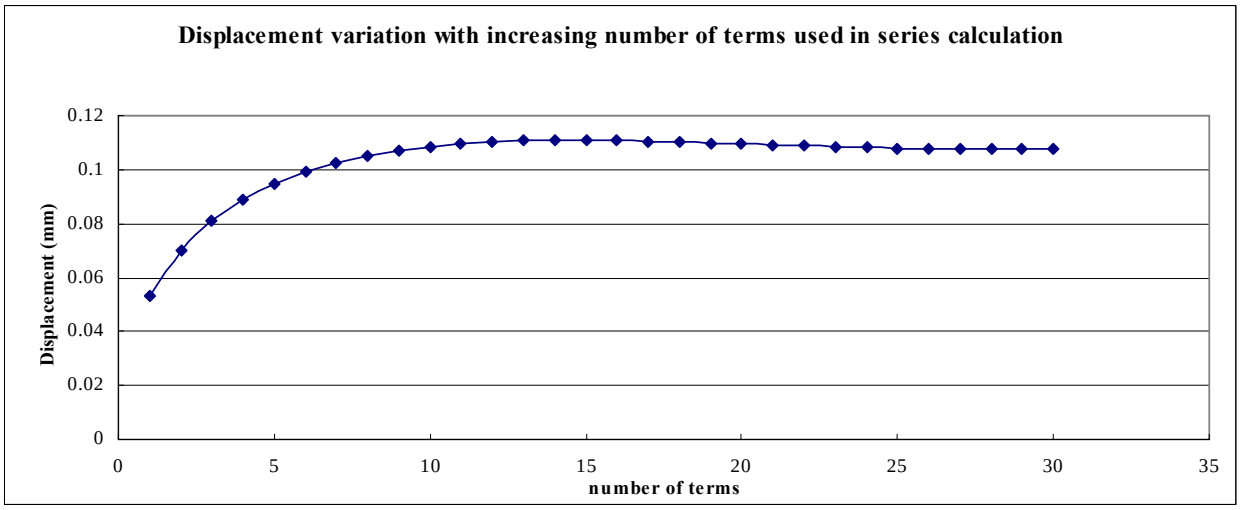

Table / Fig. 2.3.12

$\theta=225^0$, $\alpha=6^0$						
Constants &Assumptions						
R (mm)	30.48	**υ**	0.16	**G (MPa)**	15086.2069	
χ	2.4482759	**P (N)**	50000	**t (mm)**	25	
α (degree)	6	**α (rad)**	0.104719755	**w (mm)**	6.383716272	
p (MPa)	313.29713	**θ (rad)**	3.926990817	**α(x –1)**	0.151663094	
Rp/2πG	0.1007422	**θ (degree)**	225	**E (MPa)**	35000	
Calculation						
m	**cos2mθ**	**sin2mα**	**x Σ cos2mθ*sin2mα/(m*(2m+1))**	**Σ cos2mθ*sin2mα/(m*(2m-1))**	**sum of all m-terms**	**ur (mm)**
1	0	0.207912	0	0	0	0.015278875
2	-1	0.406737	-0.099580351	-0.067789441	-0.167369791	-0.001582327
3	0	0.587785	-0.099580351	-0.067789441	-0.167369791	-0.001582327
4	1	0.743145	-0.049040808	-0.041248554	-0.090289362	0.006182925
5	0	0.866025	-0.049040808	-0.041248554	-0.090289362	0.006182925
6	-1	0.951057	-0.078892714	-0.055658501	-0.134551215	0.001723888
7	0	0.994522	-0.078892714	-0.055658501	-0.134551215	0.001723888
8	1	0.994522	-0.060989303	-0.047370819	-0.108360122	0.004362437
9	0	0.951057	-0.060989303	-0.047370819	-0.108360122	0.004362437
10	-1	0.866025	-0.071085822	-0.051928847	-0.12301467	0.002886105
11	0	0.743145	-0.071085822	-0.051928847	-0.12301467	0.002886105
12	1	0.587785	-0.066288954	-0.04979919	-0.116088145	0.003583899
13	0	0.406737	-0.066288954	-0.04979919	-0.116088145	0.003583899
14	-1	0.207912	-0.067542711	-0.050349221	-0.117891932	0.003402181
15	0	1.23E-16	-0.067542711	-0.050349221	-0.117891932	0.003402181
16	1	-0.207912	-0.068506774	-0.050768398	-0.119275172	0.003262831
17	0	-0.406737	-0.068506774	-0.050768398	-0.119275172	0.003262831
18	-1	-0.587785	-0.066346022	-0.049835406	-0.116181428	0.003574501
19	0	-0.743145	-0.066346022	-0.049835406	-0.116181428	0.003574501
20	1	-0.866025	-0.068931716	-0.050945695	-0.119877411	0.00320216
21	0	-0.951057	-0.068931716	-0.050945695	-0.119877411	0.00320216
22	-1	-0.994522	-0.066472258	-0.049894403	-0.116366661	0.00355584
23	0	-0.994522	-0.066472258	-0.049894403	-0.116366661	0.00355584
24	1	-0.951057	-0.068452231	-0.050737538	-0.119189769	0.003271434
25	0	-0.866025	-0.068452231	-0.050737538	-0.119189769	0.003271434
26	-1	-0.743145	-0.067131895	-0.050177097	-0.117308992	0.003460908
27	0	-0.587785	-0.067131895	-0.050177097	-0.117308992	0.003460908
28	1	-0.406737	-0.067755832	-0.050441212	-0.118197044	0.003371444
29	0	-0.207912	-0.067755832	-0.050441212	-0.118197044	0.003371444
30	-1	-2.45E-16	-0.067755832	-0.050441212	-0.118197044	0.003371444

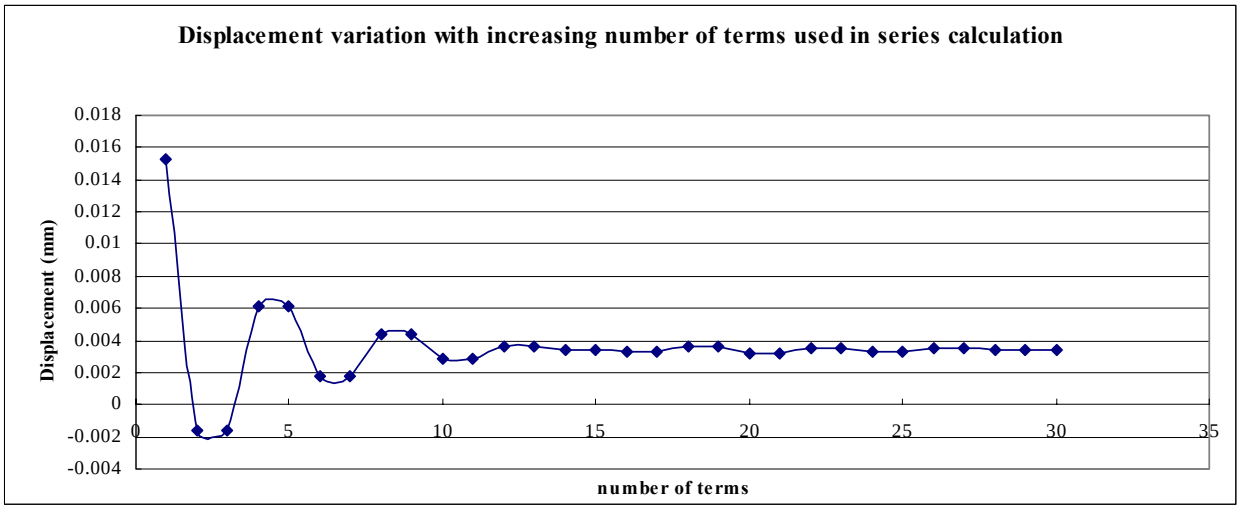

Table / Fig. 2.3.13

$\theta=270^0$, $\alpha=6^0$						
Constants &Assumptions						
R (mm)	30.48	**υ**	0.16	**G (MPa)**	15086.2069	
χ	2.4482759	**P (N)**	50000	**t (mm)**	25	
α (degree)	6	**α (rad)**	0.104719755	**w (mm)**	6.383716272	
p (MPa)	313.29713	**θ (rad)**	4.71238898	**α(x –1)**	0.151663094	
Rp/2πG	0.1007422	**θ (degree)**	270	**E (MPa)**	35000	
Calculation						
m	**cos2mθ**	**sin2mα**	**x Σ cos2mθ*sin2mα/(m*(2m+1))**	**Σ cos2mθ*sin2mα/(m*(2m-1))**	**sum of all m-terms**	**ur (mm)**
1	-1	0.207912	-0.169675058	-0.207911691	-0.377586749	-0.022760047
2	1	0.406737	-0.070094707	-0.14012225	-0.210216958	-0.005898845
3	-1	0.587785	-0.138621395	-0.179307934	-0.317929329	-0.016750027
4	1	0.743145	-0.088081853	-0.152767047	-0.2408489	-0.008984775
5	-1	0.866025	-0.1266322	-0.172012056	-0.298644256	-0.014807206
6	1	0.951057	-0.096780293	-0.157602109	-0.254382402	-0.01034817
7	-1	0.994522	-0.119969474	-0.168530921	-0.288500395	-0.013785291
8	1	0.994522	-0.102066062	-0.160243238	-0.262309301	-0.011146743
9	-1	0.951057	-0.115682721	-0.166459294	-0.282142016	-0.013144734
10	1	0.866025	-0.105586202	-0.161901266	-0.267487468	-0.011668403
11	-1	0.743145	-0.112777599	-0.165118343	-0.277895942	-0.012716976
12	1	0.587785	-0.107980731	-0.162988686	-0.270969417	-0.012019182
13	-1	0.406737	-0.110817778	-0.164240184	-0.275057962	-0.012431071
14	1	0.207912	-0.109564022	-0.163690153	-0.273254174	-0.012249354
15	-1	1.23E-16	-0.109564022	-0.163690153	-0.273254174	-0.012249354
16	1	-0.207912	-0.110528084	-0.164109329	-0.274637414	-0.012388704
17	-1	-0.406737	-0.108854465	-0.163384309	-0.272238774	-0.01214706
18	1	-0.587785	-0.111015216	-0.164317301	-0.275332518	-0.012458731
19	-1	-0.743145	-0.108559854	-0.163260196	-0.27182005	-0.012104877
20	1	-0.866025	-0.111145548	-0.164370485	-0.275516033	-0.012477218
21	-1	-0.951057	-0.108566978	-0.16326589	-0.271832868	-0.012106168
22	1	-0.994522	-0.111026437	-0.164317181	-0.275343618	-0.012459849
23	-1	-0.994522	-0.108774019	-0.163356291	-0.272130309	-0.012136133
24	1	-0.951057	-0.110753992	-0.164199426	-0.274953418	-0.012420539
25	-1	-0.866025	-0.109091036	-0.163492466	-0.272583502	-0.012181789
26	1	-0.743145	-0.110411372	-0.164052907	-0.27446428	-0.012371262
27	-1	-0.587785	-0.109442308	-0.163642156	-0.273084464	-0.012232257
28	1	-0.406737	-0.110066245	-0.163906271	-0.273972516	-0.012321721
29	-1	-0.207912	-0.109768743	-0.163780492	-0.273549236	-0.012279079
30	1	-2.45E-16	-0.109768743	-0.163780492	-0.273549236	-0.012279079
Simplified formula result			-0.012378273	**Difference (%)**		0.807828779
Formula result			-0.012289136	**Difference (%)**		0.081904969

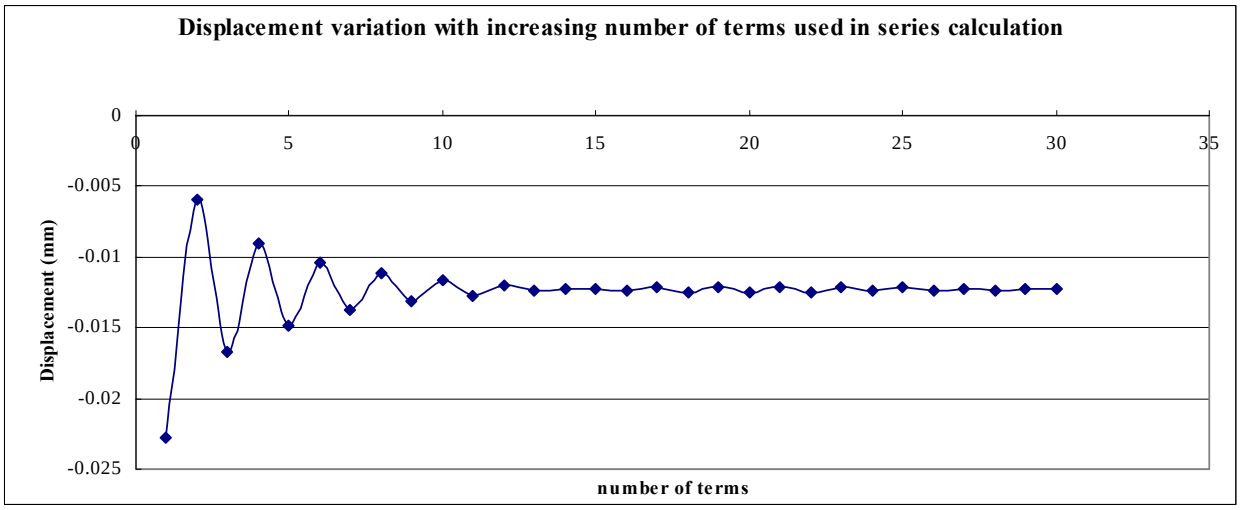

Table / Fig. 2.3.14

$\theta=315^0$, $\alpha=6^0$						
Constants &Assumptions						
R (mm)	30.48	**υ**	0.16	**G (MPa)**	15086.2069	
χ	2.4482759	**P (N)**	50000	**t (mm)**	25	
α (degree)	6	**α (rad)**	0.104719755	**w (mm)**	6.383716272	
p (MPa)	313.29713	**θ (rad)**	5.497787144	**α(x –1)**	0.151663094	
Rp/2πG	0.1007422	**θ (degree)**	315	**E (MPa)**	35000	
Calculation						
m	**cos2mθ**	**sin2mα**	**x Σ cos2mθ*sin2mα/(m*(2m+1))**	**Σ cos2mθ*sin2mα/(m*(2m-1))**	**sum of all m-terms**	**ur (mm)**
1	0	0.207912	0	0	0	0.015278875
2	-1	0.406737	-0.099580351	-0.067789441	-0.167369791	-0.001582327
3	0	0.587785	-0.099580351	-0.067789441	-0.167369791	-0.001582327
4	1	0.743145	-0.049040808	-0.041248554	-0.090289362	0.006182925
5	0	0.866025	-0.049040808	-0.041248554	-0.090289362	0.006182925
6	-1	0.951057	-0.078892714	-0.055658501	-0.134551215	0.001723888
7	0	0.994522	-0.078892714	-0.055658501	-0.134551215	0.001723888
8	1	0.994522	-0.060989303	-0.047370819	-0.108360122	0.004362437
9	0	0.951057	-0.060989303	-0.047370819	-0.108360122	0.004362437
10	-1	0.866025	-0.071085822	-0.051928847	-0.12301467	0.002886105
11	0	0.743145	-0.071085822	-0.051928847	-0.12301467	0.002886105
12	1	0.587785	-0.066288954	-0.04979919	-0.116088145	0.003583899
13	0	0.406737	-0.066288954	-0.04979919	-0.116088145	0.003583899
14	-1	0.207912	-0.067542711	-0.050349221	-0.117891932	0.003402181
15	0	1.23E-16	-0.067542711	-0.050349221	-0.117891932	0.003402181
16	1	-0.207912	-0.068506774	-0.050768398	-0.119275172	0.003262831
17	0	-0.406737	-0.068506774	-0.050768398	-0.119275172	0.003262831
18	-1	-0.587785	-0.066346022	-0.049835406	-0.116181428	0.003574501
19	0	-0.743145	-0.066346022	-0.049835406	-0.116181428	0.003574501
20	1	-0.866025	-0.068931716	-0.050945695	-0.119877411	0.00320216
21	0	-0.951057	-0.068931716	-0.050945695	-0.119877411	0.00320216
22	-1	-0.994522	-0.066472258	-0.049894403	-0.116366661	0.00355584
23	0	-0.994522	-0.066472258	-0.049894403	-0.116366661	0.00355584
24	1	-0.951057	-0.068452231	-0.050737538	-0.119189769	0.003271434
25	0	-0.866025	-0.068452231	-0.050737538	-0.119189769	0.003271434
26	-1	-0.743145	-0.067131895	-0.050177097	-0.117308992	0.003460908
27	0	-0.587785	-0.067131895	-0.050177097	-0.117308992	0.003460908
28	1	-0.406737	-0.067755832	-0.050441212	-0.118197044	0.003371444
29	0	-0.207912	-0.067755832	-0.050441212	-0.118197044	0.003371444
30	-1	-2.45E-16	-0.067755832	-0.050441212	-0.118197044	0.003371444

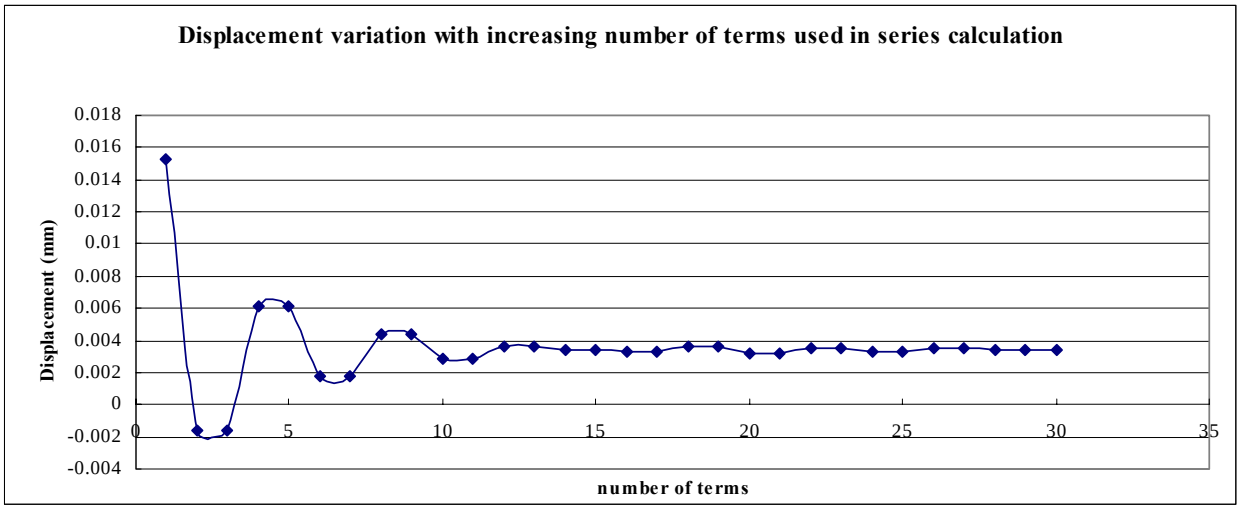

2.4 Contact pressure experimental results

The contact pressure distribution of the specimen and load platen in a Brazilian test is a typical contact problem, which had been solved by Hertz (1881) theoretically. But because it's impossible for the real test conditions to meet the needs of theory, for example, the surface of a real specimen can't be absolutely smooth, the real contact pressure distribution should be determined by experimental method.

The pressure film of SPI Corporation East Hanover, NS, was employed to measure the contact pressure distribution. The film can be inserted between the two contact surfaces. After testing, it can be processed and show the distribution of contact pressure. Unfortunately, the contact pressure in our Brazilian tests is very high. SPI Corporation can't process this type of film precisely: they can't give the numerical results, but only the outline of the pressure distribution.

The following are examples of the results (specimen 01026155-2-B):

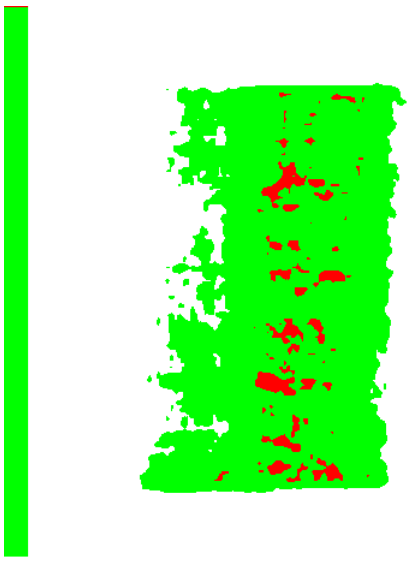

Fig. 1: Original film result of the top of specimen 01026155-2-B.

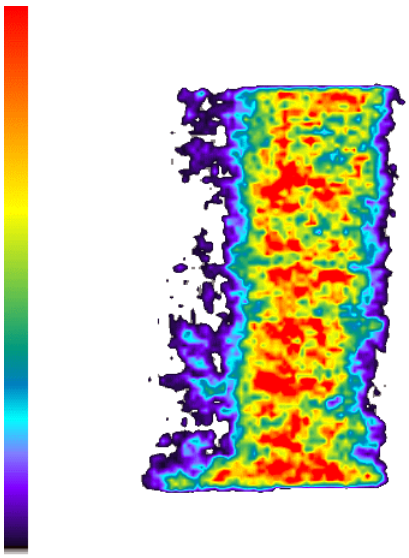

Fig. 2: Enhanced film result of the top of specimen 01026155-2-B (The left legend shows the pressures from low to high according to the colors from bottom to top).

The three-dimensional figure is also available:

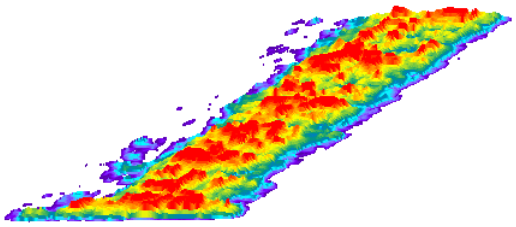

Fig. 3: Three-dimensional demonstration of pressure distribution of the top of specimen 01026155-2-B

More other results:

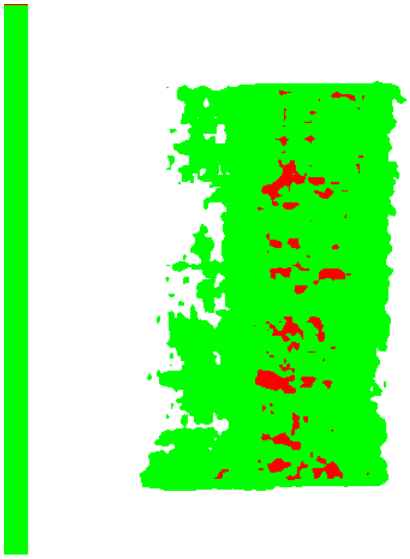

Fig. 4: Specimen 01026155-2-B (bottom) (1)

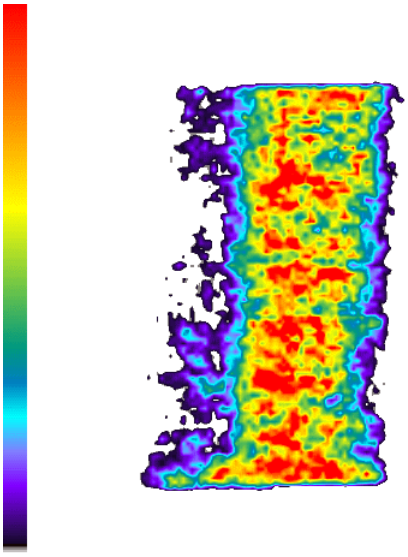

Fig. 5: Specimen 01026155-2-B (bottom) (2)

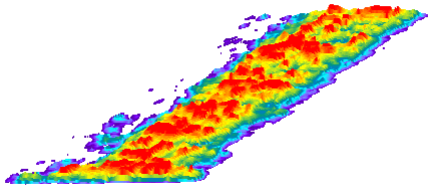

Fig. 6: Specimen 01026155-2-B (bottom) (3)

Fig. 7: Specimen 01026248-2-B (Top) (1)

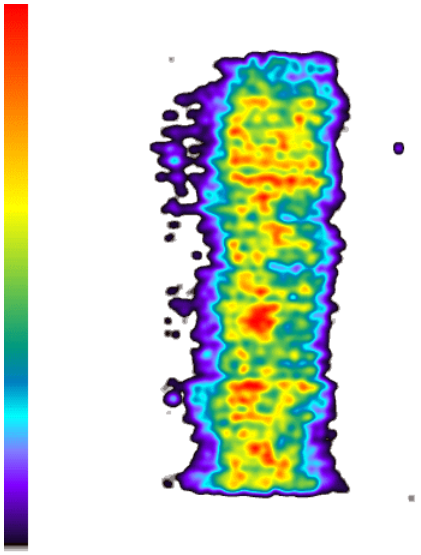

Fig. 8: Specimen 01026248-2-B (Top) (2)

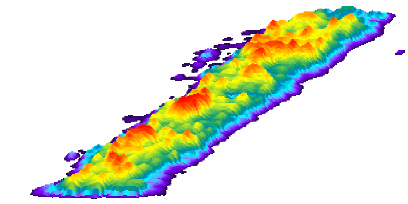

Fig. 9: Specimen 01026248-2-B (Top) (3)

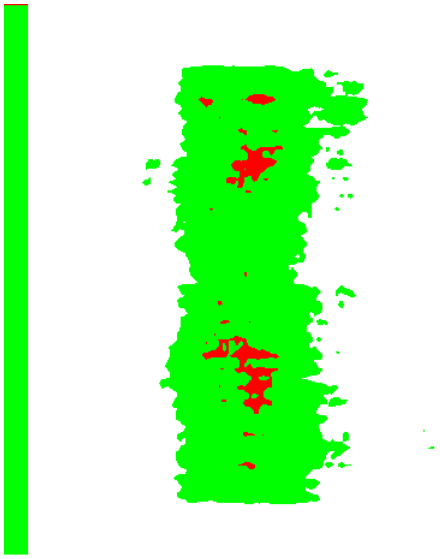

Fig. 10: Specimen 01026248-2-B (Bottom) (1)

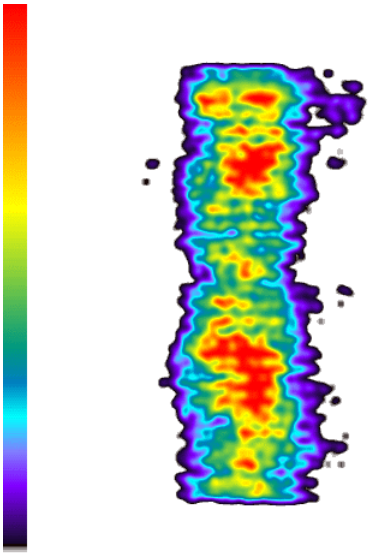

Fig. 11: Specimen 01026248-2-B (Bottom) (2)

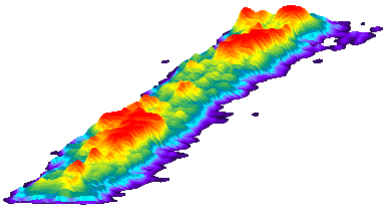

Fig. 12: Specimen 01026248-2-B (Bottom) (3)

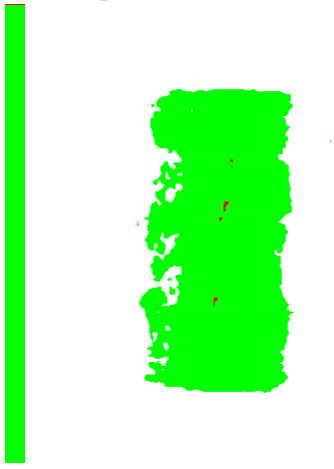

Fig. 13: Specimen 01026160-4-B (Top) (1)

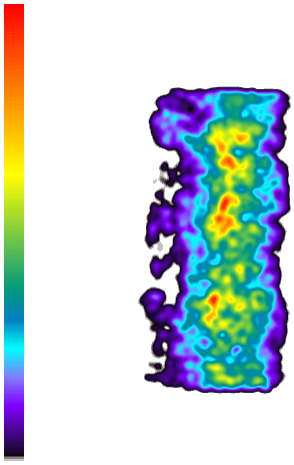

Fig. 14: Specimen 01026160-4-B (Top) (2)

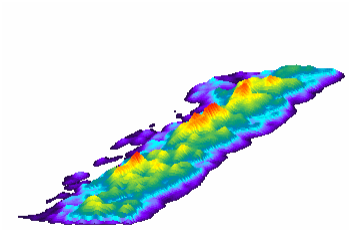

Fig. 15: Specimen 01026160-4-B (Top) (3)

Fig. 16: Specimen 01026160-4-B (Bottom) (1)

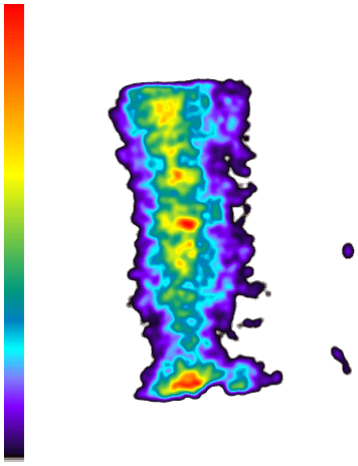

Fig. 17: Specimen 01026160-4-B (Bottom) (2)

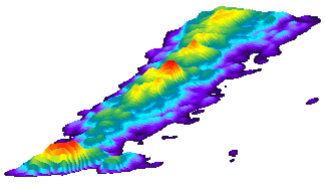

Fig. 18: Specimen 01026160-4-B (Bottom) (3)

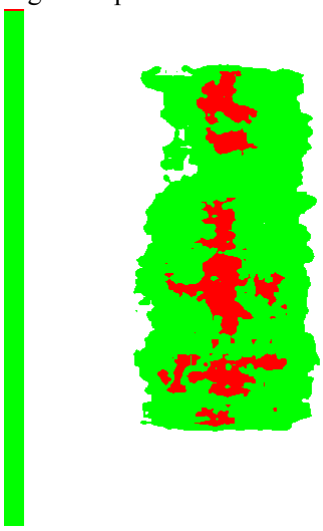

Fig. 19: Specimen 01026259-2-B (Top) (1)

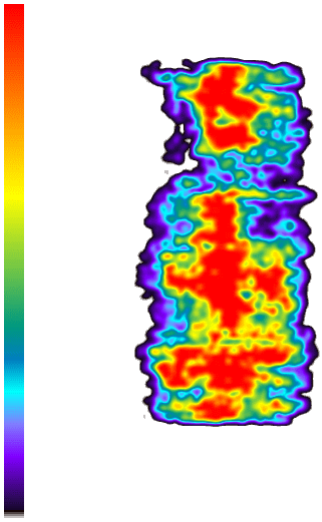

Fig. 20: Specimen 01026259-2-B (Top) (2)

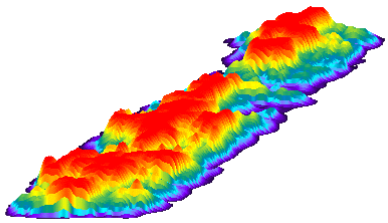

Fig. 21: Specimen 01026259-2-B (Top) (3)

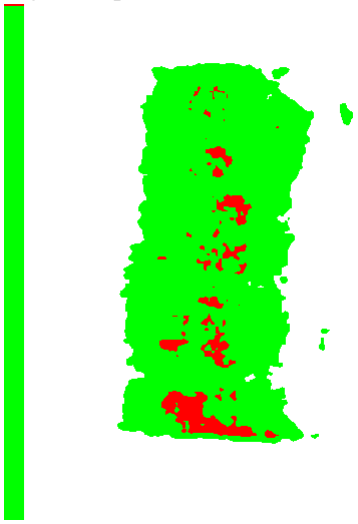

Fig. 22: Specimen 01026259-2-B (Bottom) (1)

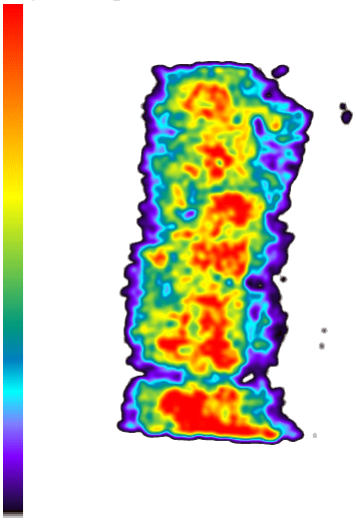

Fig. 23: Specimen 01026259-2-B (Bottom) (2)

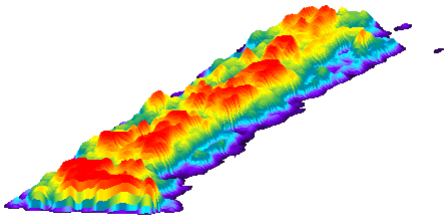

Fig. 24: Specimen 01026259-2-B (Bottom) (3)

Fig. 25: Specimen 01026258-1-B (Top) (1)

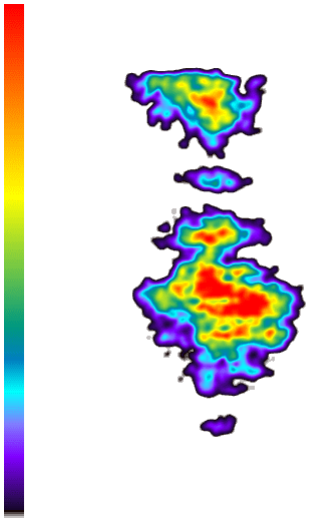

Fig. 26: Specimen 01026258-1-B (Top) (2)

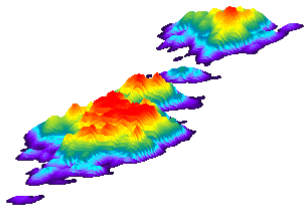

Fig. 27: Specimen 01026258-1-B (Top) (3)

Fig. 28: Specimen 01026258-1-B (Bottom) (1)

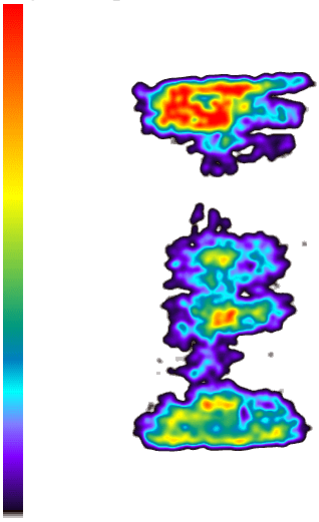

Fig. 29: Specimen 01026258-1-B (Bottom) (2)

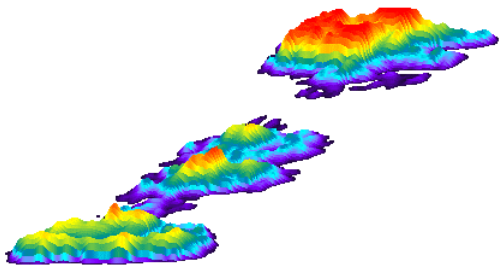

Fig. 30: Specimen 01026258-1-B (Bottom) (3)

These results show: **the contact pressure distribution is highly uneven and very different from the theoretical results**. The condition probably caused by the rough surface of specimen.

2.5 Force-displacement curves

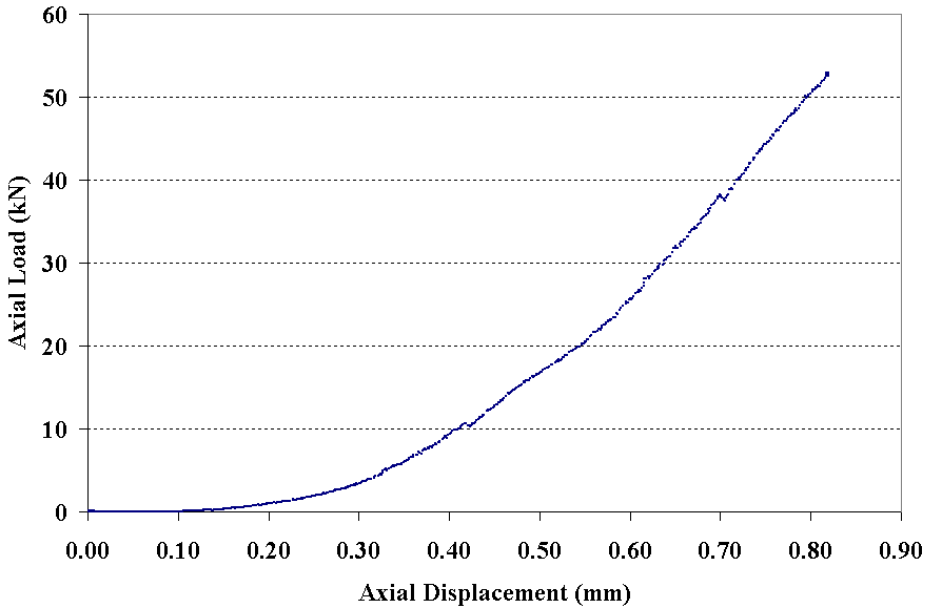

Figure 2.5.1 Force-displacement curves for specimen 01026161-3-B; displacement rate = 0.0002 mm/minute; tensile strength = 18.75 MPa

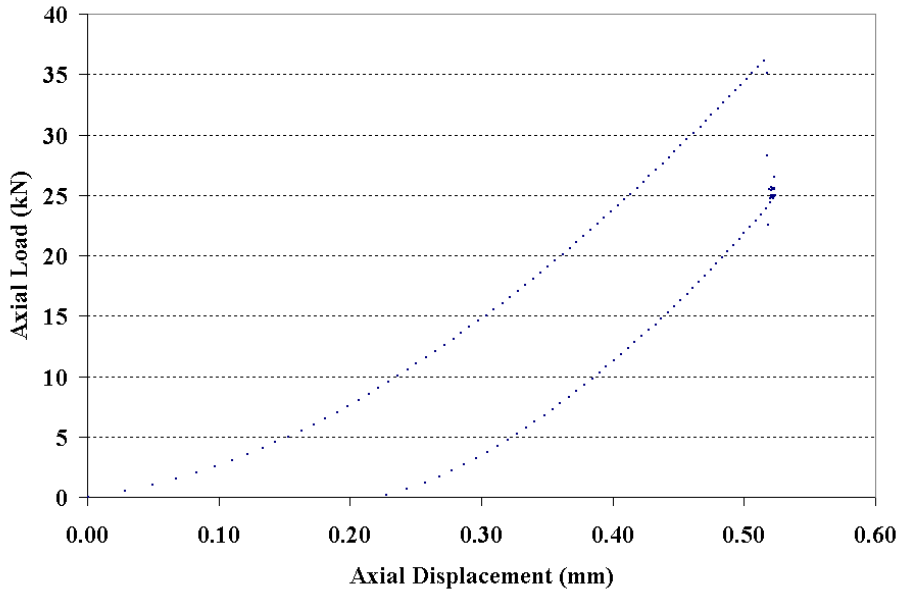

Figure 2.5.2 Force-displacement curves for specimen 01026163-1-B; displacement rate = 0.2 mm/minute; tensile strength = 12.46 MPa

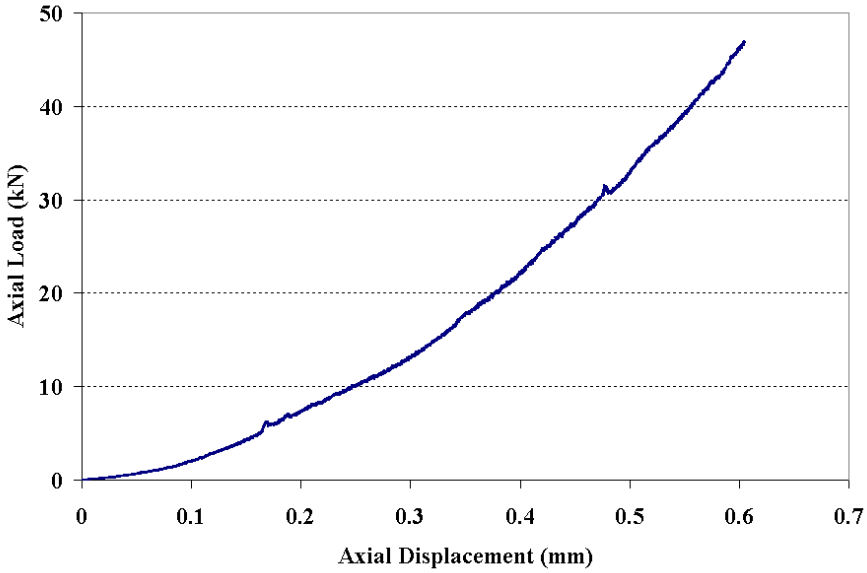

Figure 2.5.3 Force-displacement curves for specimen 01026167-2-B; displacement rate = 0.0002 mm/minute; tensile strength = 16.49 MPa

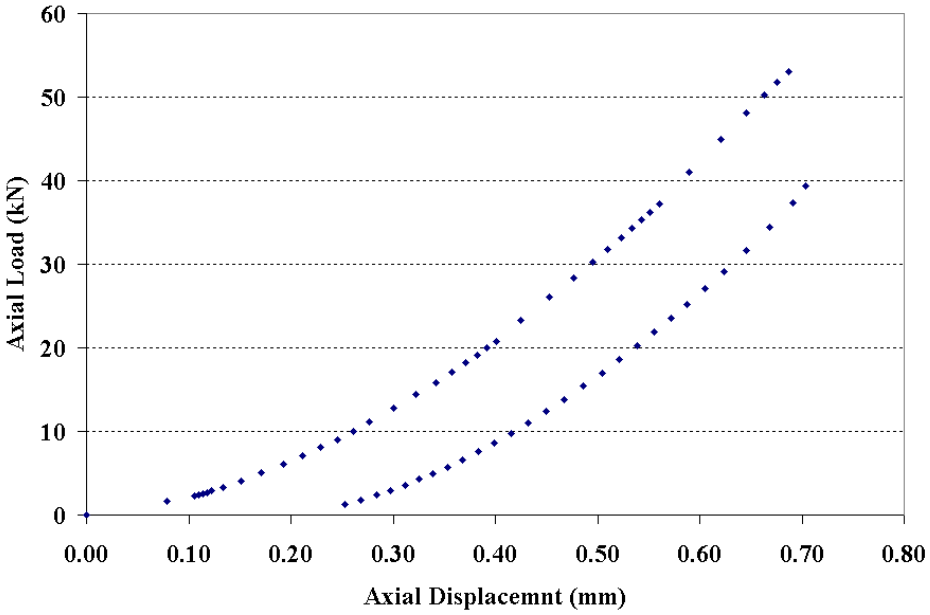

Figure 2.5.4 Force-displacement curves for specimen 01026248-1-B; displacement rate = 0.2 mm/minute; tensile strength = 18.84 MPa

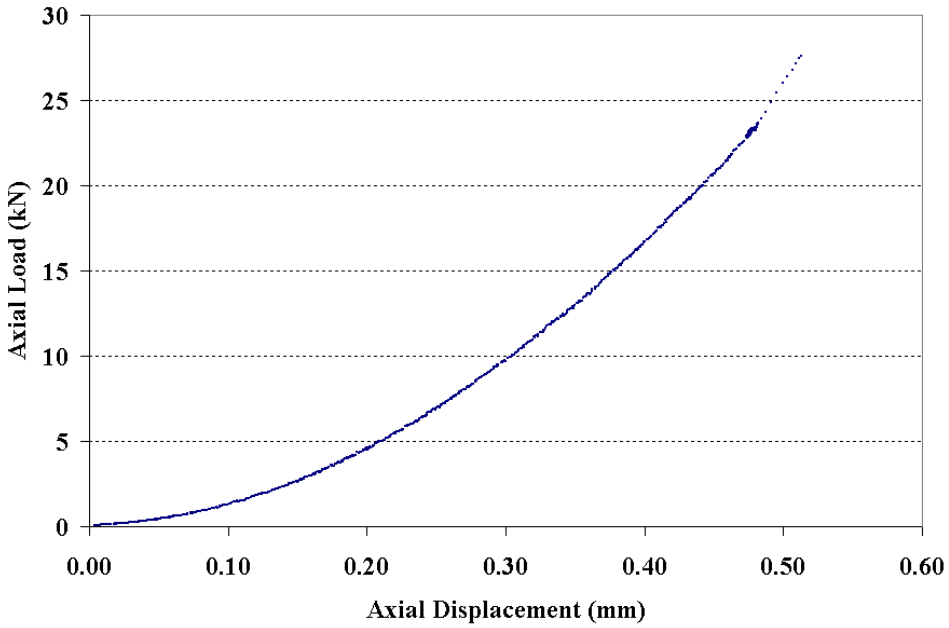

Figure 2.5.5 Force-displacement curves for specimen 01026294-1-B; displacement rate = 0.002 mm/minute; tensile strength = 20.22 MPa

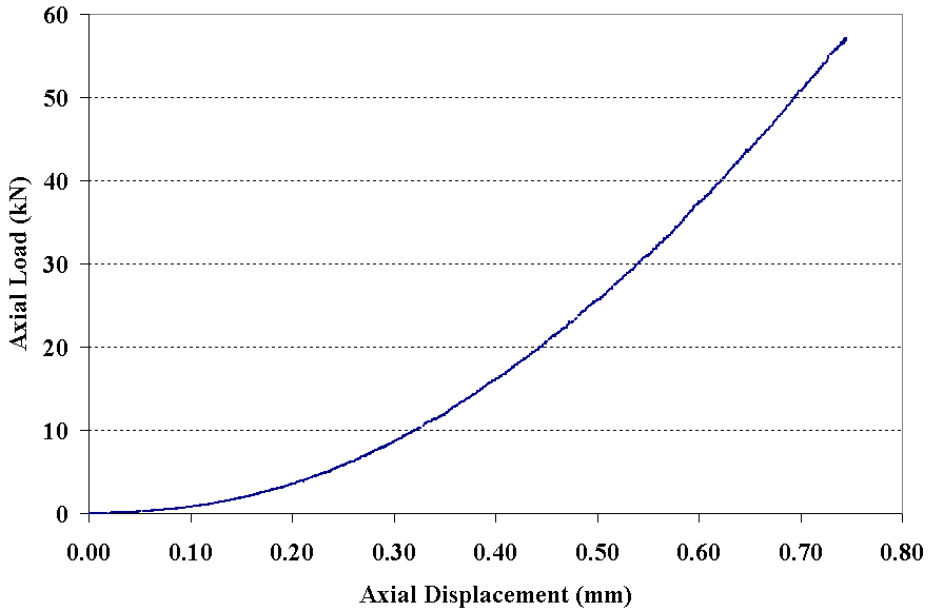

Figure 2.5.6 Force-displacement curves for specimen 01026294-3-B; displacement rate = 0.002 mm/minute; tensile strength = 18.54 MPa

2.6 Photographs

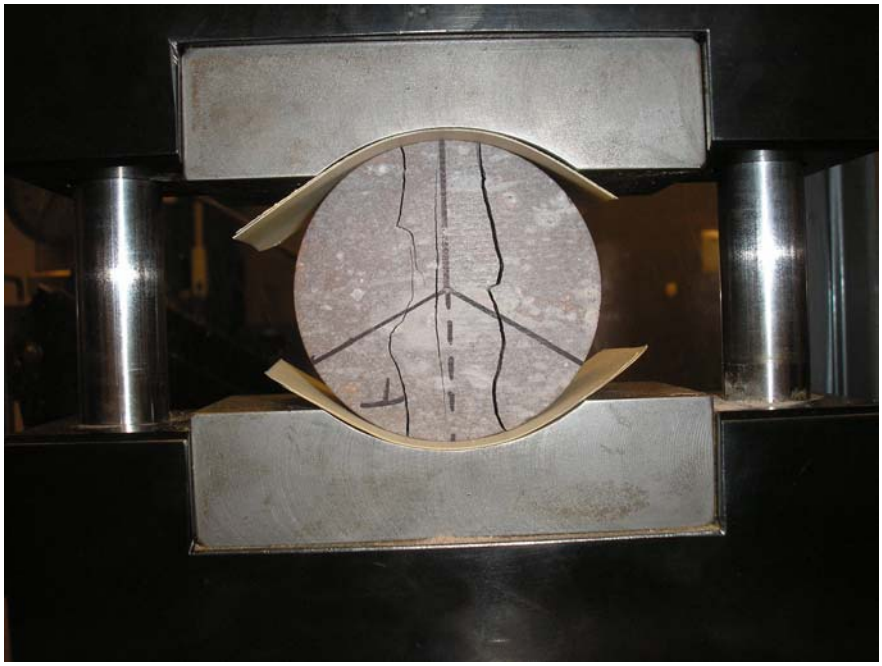

Figure 2.5.7 Specimen after Brazilian (indirect tensile strength) test, specimen ID 01026167-4-B

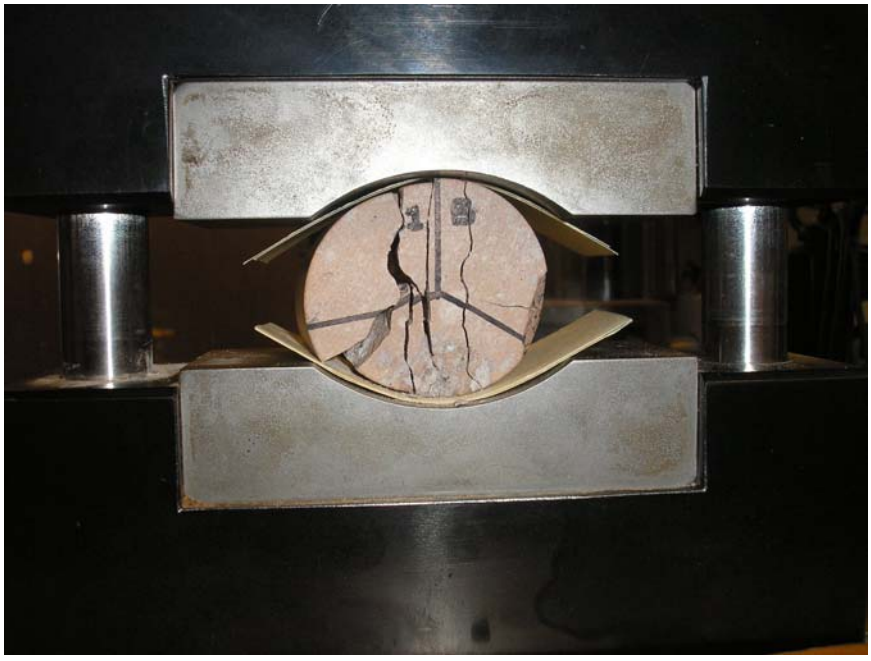

Figure 2.5.8 Specimen after Brazilian (indirect tensile strength) test, specimen ID 01026206-1-B

Figure 2.5.9 Specimen after Brazilian (indirect tensile strength) test, specimen ID 01026209-4-B

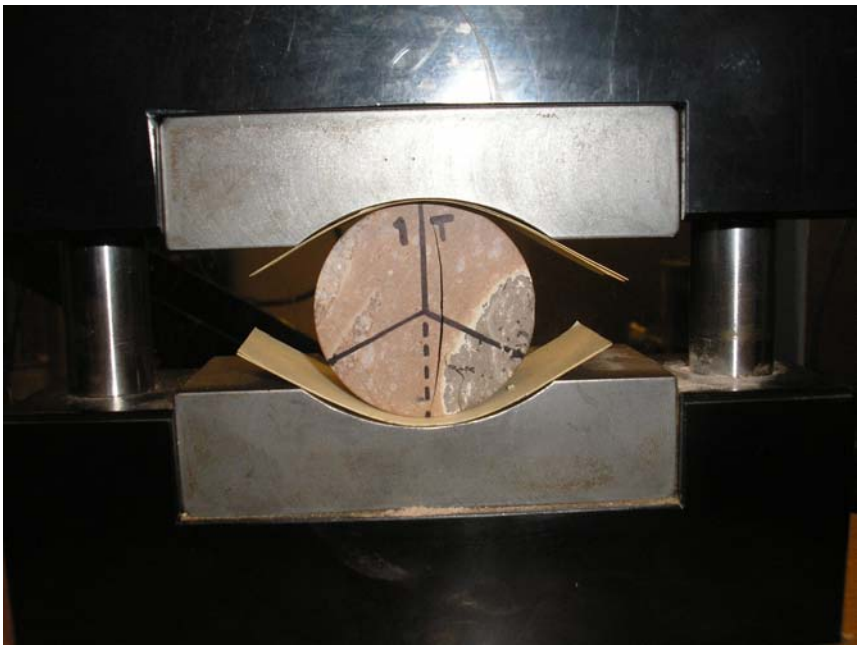

Figure 2.5.10 Specimen after Brazilian (indirect tensile strength) test, specimen ID 01026209-3-B

Appendix 3 - Uniaxial Compression Test

3.1 Specimen

Table 3.1 Specimen characteristics

Specimen ID	01026175-U	**Parent Specimen**	01026175
Specimen Borehole	UE-25 UZ#16	**Geological Formation**	Tptpln
Diameter (mm)	60.96	**Length(mm)**	118.62

3.2 Test Summary

Table 3.2 Test Summary

Peak Force (N)	190445	**Duration (s)**	406
Corresponding Displacement (mm)	1.079920	**Calculated Strength (MPa)**	62.25
Young's Modulus (MPa)	13578	**Poisson's Ratio**	0.3369

Note: Calculations of Young's Modulus and Poisson's ratio follow ASTM D3148-96 Standard Test Method for Elastic Moduli of Intact Rock Core Specimens in Uniaxial Compression. They are determined at 50% of the peak stress level.

3.3 Plots and Photos

3.3.1 Plots

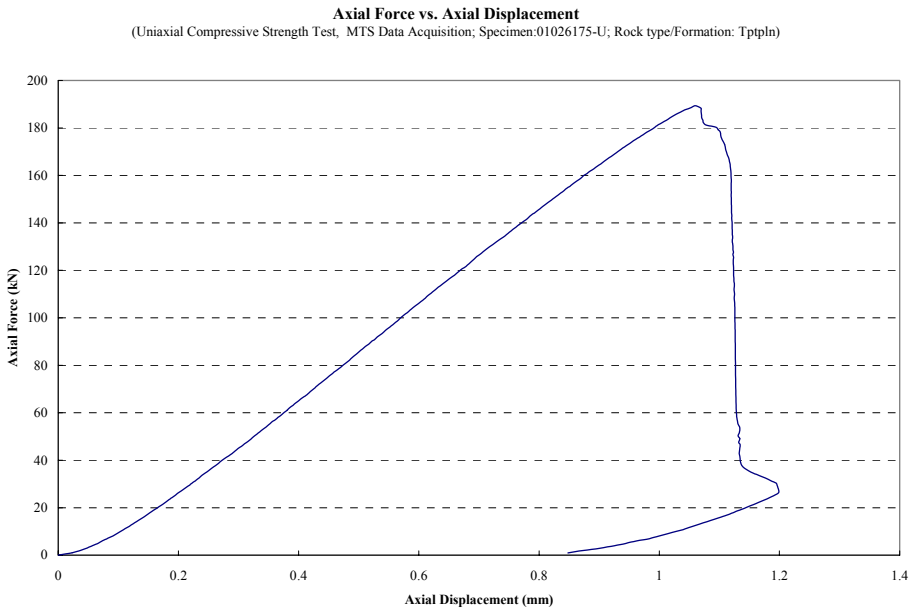

Fig. 3.1

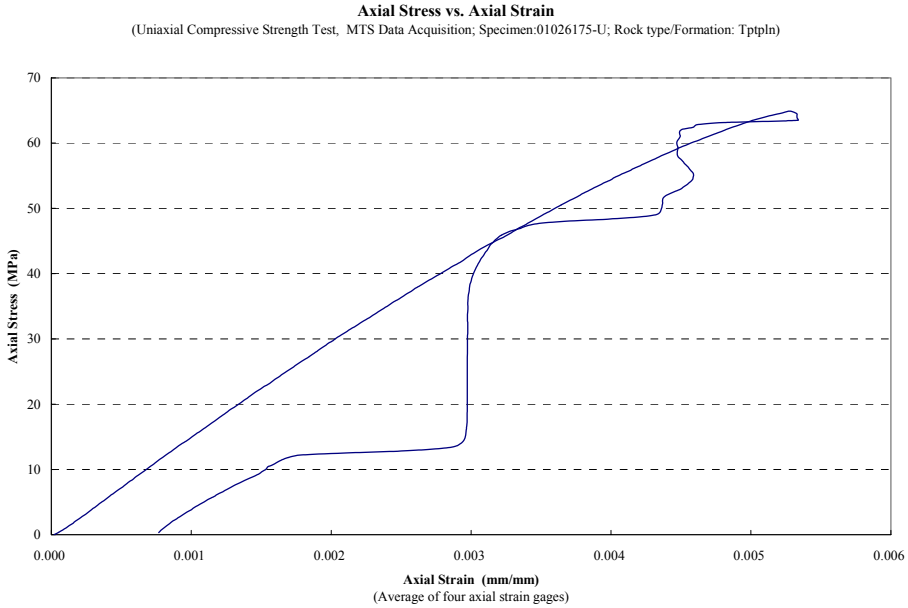

Fig. 3.2

3.3.2 Photos of failed specimen

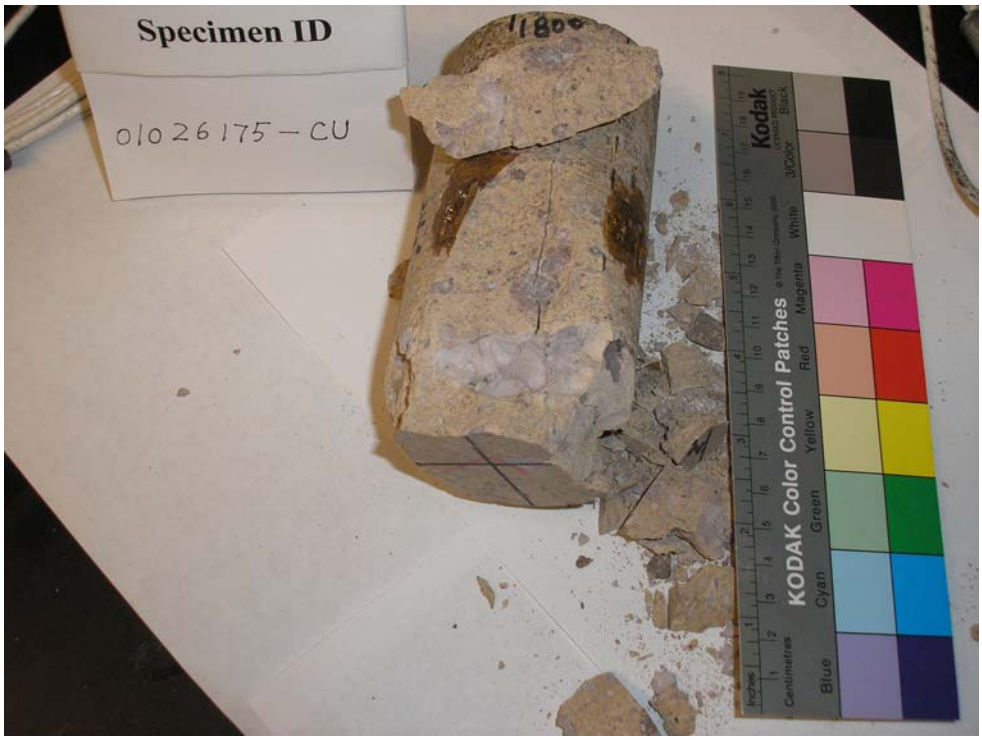

Fig. 3.3

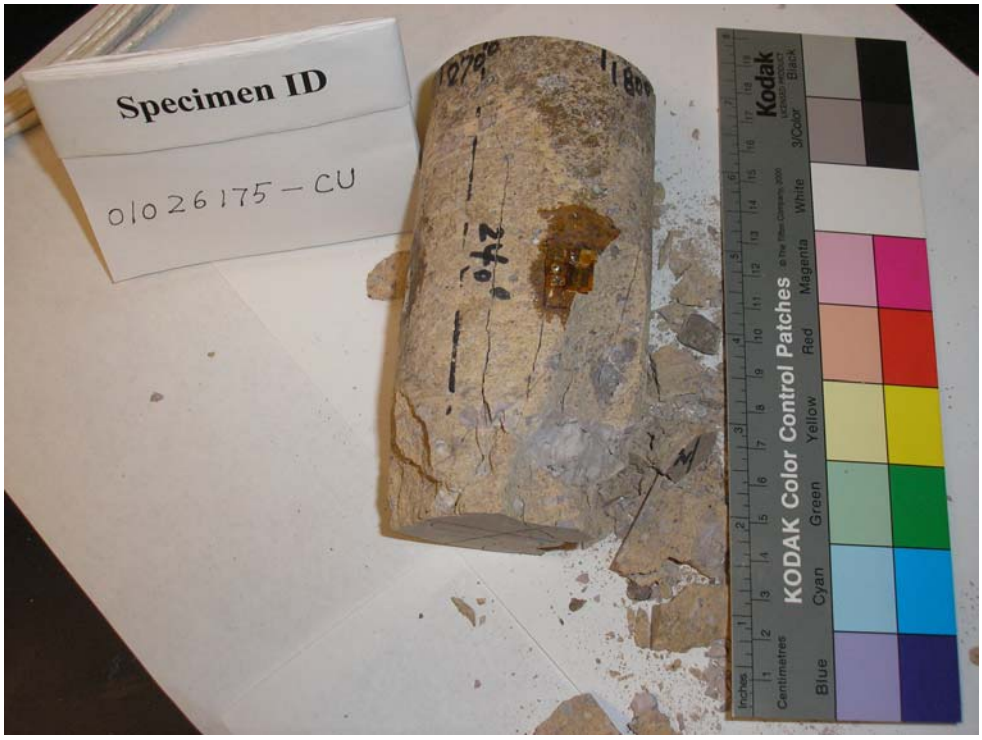
Specimen ID
010 26 175 – CU
KODAK Color Control Patches
Kodak

Fig. 3.4


Specimen ID
010 26 175 – CU
Kodak

Fig. 3.5


Specimen ID
0102 6175 – CU
Kodak
Color Control Patches
Blue
Cyan
Green
Yellow
Red
Magenta
White
Black

Fig. 3.6


Specimen ID
0102 6175 – CU
1800
Kodak
KODAK Color Control Patches
Blue
Cyan
Green
Yellow
Red
Magenta
White
Black

Fig. 3.7

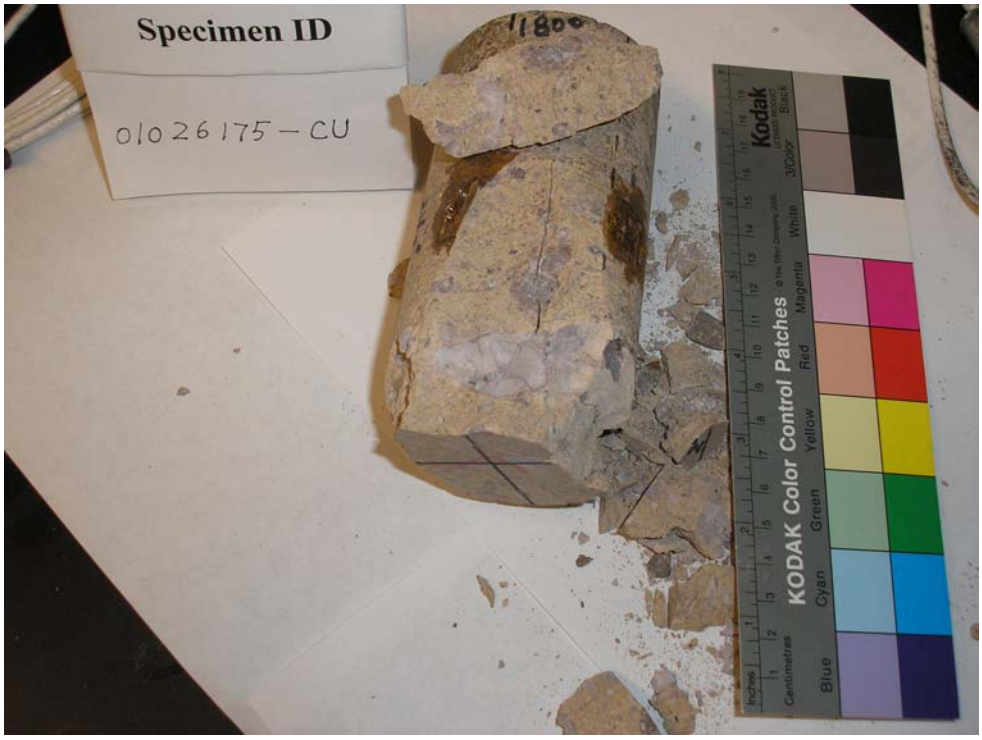
Specimen ID
0102617S – CU
KODAK Color Control Patches
Kodak

Fig. 3.8


Specimen ID
0102617S – CU
Kodak

Fig. 3.9

Appendix 4 - Uniaxial Compression Creep Test

4.1 Specimen

Table 4.1 Specimen Characteristics

Specimen ID	01026228-CU	**Parent Specimen**	01026228
Specimen Borehole	ESF-HD-WH-43	**Geological Formation**	Tptpmn
Diameter (mm)	60.73	**Length (mm)**	148.06

4.2 Test Summary

Table 4.2 Test Summary

First Level (MPa)	70	**Duration Per Level**	2 weeks
Stress Increment (MPa)	40	**Failure Stress (MPa)**	150
Young's Modulus (MPa)	43952	**Poisson's Ratio**	0.1479

Note: Young's Modulus and Poisson's ratio are determined at the 50% of first stress level (70MPa).

4.3 Plots and Photos

4.3.1 Plots

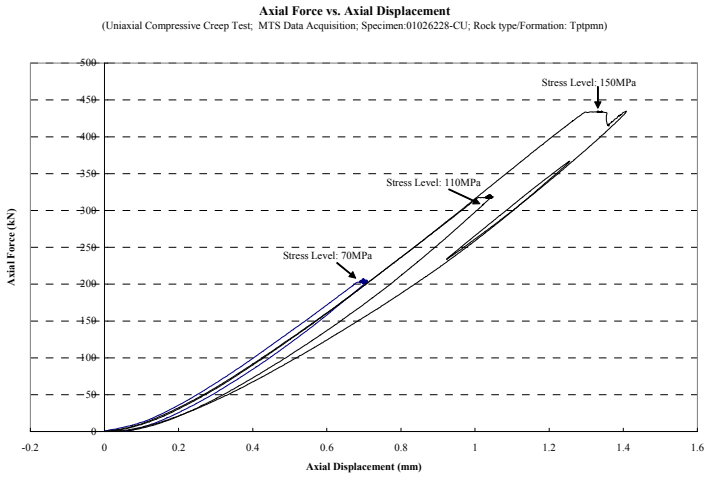

Fig 4.1

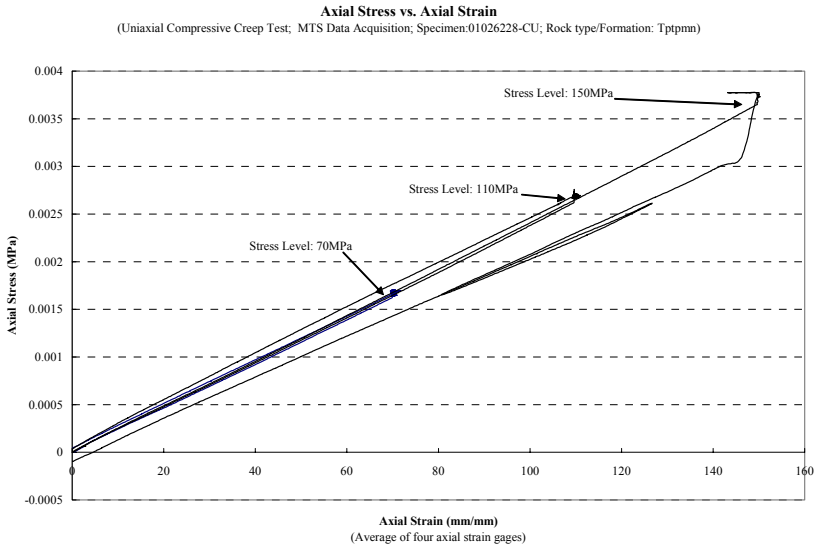
Axial Stress vs. Axial Strain
(Uniaxial Compressive Creep Test; MTS Data Acquisition; Specimen:01026228-CU; Rock type/Formation: Tptpmn)
Stress Level: 150MPa
Stress Level: 110MPa
Stress Level: 70MPa
Axial Stress (MPa)
0.004
0.0035
0.003
0.0025
0.002
0.0015
0.001
0.0005
0
-0.0005
0
20
40
60
80
100
120
140
160
Axial Strain (mm/mm)
(Average of four axial strain gages)

Fig 4.2

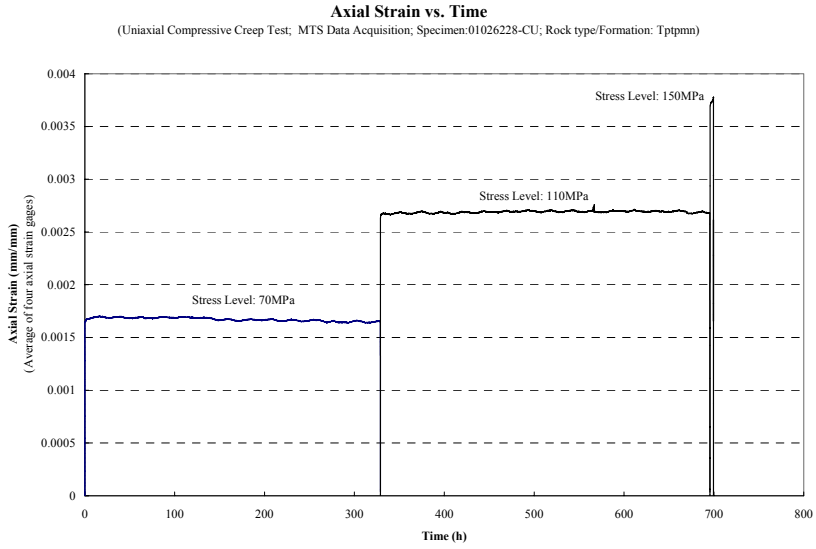
Axial Strain vs. Time
(Uniaxial Compressive Creep Test; MTS Data Acquisition; Specimen:01026228-CU; Rock type/Formation: Tptpmn)
Stress Level: 150MPa
Stress Level: 110MPa
Stress Level: 70MPa
Axial Strain (mm/mm)
(Average of four axial strain gages)
0.004
0.0035
0.003
0.0025
0.002
0.0015
0.001
0.0005
0
0
100
200
300
400
500
600
700
800
Time (h)

Fig 4.3

4.3.2 Photos of failed specimen

Fig. 4.4

Fig. 4.5

Fig. 4.6

Fig. 4.7

Fig. 4.8

Appendix 5 –

Particle Size Distribution of failed Tptpmn (Topopah Spring Middle Nonlithophysal) Tuff Cylinder Specimens Tested in Uniaxial Compression at Various Strain Rates

5.1. Introduction

The strain rate at which tests are performed impacts the strength of rock. Perhaps it will influence the crack pattern of the rock. In fact, in the more than 80 uniaxial tests performed to determine the strength of the Tptpmn Tuff, we observed it might be a rule that when the strain rate goes up, the size of the resulting particles gets smaller (Figures 5.1 and 5.2).

Fig. 5.1: Typical failure at low strain rate (Strain rate=1.10e-8)

Fig. 5.2: Typical failure at high strain rate (Strain rate=8.85e-3)

To verify our viewpoint, sieving was used to determine the particle size distribution.

5.2 Sieving

The sizes of the sieve openings we used are 1.5 in, 1.0 in, 0.75 in, 0.5 in, 0.375 in and 0.25 in. Because the failure of specimens under compressive load is predominately longitudinal, especially at low strain rates (Fig. 5.1), many particles are much larger in one dimension, so it is difficult to sieve them mechanically. Thus we manually sieved them to ensure that all the particles less than the sieve openings size in the two shorter dimensions can pass through the openings. The weights of particles retained on each sieve and of those falling into the container are written down. The percentage of the particle weight in each sieve size and in the lowest container is calculated.

5.3 Results and discussion

5.3.1. Sieving results

The samples we used were failed specimens of the uniaxial compression tests in Yucca Mountain Project Task 18 (See Task 18 Final Report (Ma and Daemen, 2004), or: http://www.unr.edu/rockmech/Research.htm for detail). All are from the same rock formation, Tptpmn (Topopah Spring crystal-poor Middle Nonlithophysal). Before sieving, the specimens without major flaws were selected in the specimen database. A

total of 63 specimens were selected. The sieving results are listed below (Tables 5.1 and 5.2):

Table 5.1: The particle weight distribution

Specimen ID	Strain Rate (1/s)	>1.5" (g)	1-1.5" (g)	0.75-1" (g)	0.5-0.75" (g)	0.375-0.5" (g)	0.25-0.375" (g)	<0.25" (g)
01023576-3-U	1.10E-08	952	628	376	78	20	38	26
01023586-3-U	1.34E-08	664	162	86	138	92	56	8
01023668-3-U	1.36E-08	808	560	78	302	62	76	32
01023706-1-U	2.78E-08	0	550	296	208	100	72	16
01025233-1-U	1.01E-07	338	1216	264	258	92	76	12
01023576-2-U	1.08E-07	1506	60	202	156	52	30	36
01025264-U	1.09E-07	1560	398	68	24	10	22	10
01023662-1-U	1.15E-07	138	634	460	348	66	60	4
01023682-2-U	1.16E-07	1912	260	0	20	18	8	2
01023751-1-U	1.16E-07	690	322	360	286	64	36	10
01025226-1-U	1.29E-07	534	342	190	144	86	22	4
01023687-3-U	1.31E-07	160	450	176	238	78	24	4
01023660-1-U	1.32E-07	1704	0	0	62	14	6	0
01023575-2-U	1.35E-07	1382	214	50	26	4	8	8
01023697-1-U	1.37E-07	1918	138	26	16	16	14	2
01023687-2-U	1.04E-06	1108	148	138	270	72	56	30
01025259-1-U	1.10E-06	436	538	358	264	80	72	28
01023749-2-U	1.15E-06	1600	236	52	104	48	16	4
01023686-2-U	1.16E-06	730	466	198	218	62	94	20
01023707-1-U	1.17E-06	924	518	64	226	66	36	2
01023667-1-U	1.19E-06	1438	284	88	132	36	14	2
01023580-U	1.24E-06	896	0	336	304	112	128	72
01023747-1-U	1.24E-06	0	430	214	320	108	78	14
01023686-1-U	1.28E-06	184	242	154	468	68	90	8
01025235-2-U	1.30E-06	248	620	238	240	88	56	6
01025260-1-U	1.33E-06	0	512	334	470	184	140	32
01023694-2-U	1.35E-06	328	332	250	270	96	58	16
01023722-2-U	1.38E-06	214	76	330	266	102	84	14
01025230-1-U	1.47E-06	362	492	196	378	86	42	14
01023732-U	9.80E-06	1840	0	118	30	8	12	2
01023662-2-U	9.89E-06	550	602	352	246	44	64	6
01023687-1-U	1.05E-05	0	504	374	330	166	162	54
01023743-1-U	1.05E-05	1696	14	74	146	38	38	10
01025224-3-U	1.06E-05	1724	264	108	40	14	44	36
01023664-U	1.08E-05	548	216	210	448	136	102	32
01023740-1-U	1.09E-05	1930	46	58	48	26	32	30

Specimen ID	Strain Rate (1/s)	>1.5" (g)	1-1.5" (g)	0.75-1" (g)	0.5-0.75" (g)	0.375-0.5" (g)	0.25-0.375" (g)	<0.25" (g)
01023579-1-U	1.11E-05	1354	174	18	116	18	20	4
01023657-1-U	1.13E-05	592	838	332	140	38	18	2
01023701-1-U	1.16E-05	320	554	230	336	146	104	14
01025230-2-U	1.16E-05	378	178	274	254	114	62	6
01023702-2-U	1.17E-05	434	374	246	304	42	60	10
01023657-3-U	1.18E-05	990	300	290	102	60	24	2
01023695-2-U	1.20E-05	100	792	324	338	64	56	8
01023750-U	1.21E-05	942	0	96	140	116	82	40
01023582-1-U	1.24E-05	554	590	262	262	106	128	114
01025234-1-U	1.30E-05	500	360	154	196	110	70	6
01023657-4-U	1.33E-05	0	356	272	256	100	74	10
01023707-3-U	1.33E-05	704	252	192	184	92	52	10
01023760-2-U	9.85E-05	548	334	390	270	38	70	18
01025225-1-U	1.05E-04	576	464	232	338	102	26	8
01023689-2-U	1.13E-04	392	316	352	402	100	108	24
01023747-3-U	1.15E-04	350	458	160	314	84	52	14
01025225-2-U	1.16E-04	494	480	320	140	56	34	4
01023692-U	1.18E-04	0	652	290	374	114	90	6
01025235-1-U	1.24E-04	0	460	292	254	70	56	14
01023703-1-U	1.25E-04	204	496	126	222	84	92	28
01023703-2-U	1.31E-04	338	442	144	234	78	52	4
01025224-1-U	1.32E-04	0	774	134	392	46	46	6
01023690-1-U	1.35E-04	0	200	332	390	114	70	12
01025227-1-U	9.65E-04	234	692	384	250	120	90	14
01025262-U	5.43E-03	612	78	120	300	88	66	18
01025232-1-U	7.45E-03	986	360	120	188	48	44	6
01025227-2-U	8.85E-03	0	554	284	162	86	76	40

Table 5.2: Distribution of the weight percentage

Specimen ID	Strain Rate (1/s)	>1.5" (%)	1-1.5" (%)	0.75-1" (%)	0.5-0.75" (%)	0.375-0.5" (%)	0.25-0.375" (%)	<0.25" (%)
01023576-3-U	1.10E-08	0.45	0.30	0.18	0.04	0.01	0.02	0.01
01023586-3-U	1.34E-08	0.55	0.13	0.07	0.11	0.08	0.05	0.01
01023668-3-U	1.36E-08	0.42	0.29	0.04	0.16	0.03	0.04	0.02
01023706-1-U	2.78E-08	0.00	0.44	0.24	0.17	0.08	0.06	0.01
01025233-1-U	1.01E-07	0.15	0.54	0.12	0.11	0.04	0.03	0.01
01023576-2-U	1.08E-07	0.74	0.03	0.10	0.08	0.03	0.01	0.02
01025264-U	1.09E-07	0.75	0.19	0.03	0.01	0.00	0.01	0.00
01023662-1-U	1.15E-07	0.08	0.37	0.27	0.20	0.04	0.04	0.00
01023682-2-U	1.16E-07	0.86	0.12	0.00	0.01	0.01	0.00	0.00
01023751-1-U	1.16E-07	0.39	0.18	0.20	0.16	0.04	0.02	0.01
01025226-1-U	1.29E-07	0.40	0.26	0.14	0.11	0.07	0.02	0.00
01023687-3-U	1.31E-07	0.14	0.40	0.16	0.21	0.07	0.02	0.00
01023660-1-U	1.32E-07	0.95	0.00	0.00	0.03	0.01	0.00	0.00
01023575-2-U	1.35E-07	0.82	0.13	0.03	0.02	0.00	0.00	0.00
01023697-1-U	1.37E-07	0.90	0.06	0.01	0.01	0.01	0.01	0.00
01023687-2-U	1.04E-06	0.61	0.08	0.08	0.15	0.04	0.03	0.02
01025259-1-U	1.10E-06	0.25	0.30	0.20	0.15	0.05	0.04	0.02
01023749-2-U	1.15E-06	0.78	0.11	0.03	0.05	0.02	0.01	0.00
01023686-2-U	1.16E-06	0.41	0.26	0.11	0.12	0.03	0.05	0.01
01023707-1-U	1.17E-06	0.50	0.28	0.03	0.12	0.04	0.02	0.00
01023667-1-U	1.19E-06	0.72	0.14	0.04	0.07	0.02	0.01	0.00
01023580-U	1.24E-06	0.48	0.00	0.18	0.16	0.06	0.07	0.04
01023747-1-U	1.24E-06	0.00	0.37	0.18	0.27	0.09	0.07	0.01
01023686-1-U	1.28E-06	0.15	0.20	0.13	0.39	0.06	0.07	0.01
01025235-2-U	1.30E-06	0.17	0.41	0.16	0.16	0.06	0.04	0.00
01025260-1-U	1.33E-06	0.00	0.31	0.20	0.28	0.11	0.08	0.02
01023694-2-U	1.35E-06	0.24	0.25	0.19	0.20	0.07	0.04	0.01
01023722-2-U	1.38E-06	0.20	0.07	0.30	0.24	0.09	0.08	0.01
01025230-1-U	1.47E-06	0.23	0.31	0.12	0.24	0.05	0.03	0.01
01023732-U	9.80E-06	0.92	0.00	0.06	0.01	0.00	0.01	0.00
01023662-2-U	9.89E-06	0.30	0.32	0.19	0.13	0.02	0.03	0.00
01023687-1-U	1.05E-05	0.00	0.32	0.24	0.21	0.10	0.10	0.03
01023743-1-U	1.05E-05	0.84	0.01	0.04	0.07	0.02	0.02	0.00
01025224-3-U	1.06E-05	0.77	0.12	0.05	0.02	0.01	0.02	0.02
01023664-U	1.08E-05	0.32	0.13	0.12	0.26	0.08	0.06	0.02
01023740-1-U	1.09E-05	0.89	0.02	0.03	0.02	0.01	0.01	0.01
01023579-1-U	1.11E-05	0.79	0.10	0.01	0.07	0.01	0.01	0.00

Specimen ID	Strain Rate (1/s)	>1.5" (%)	1-1.5" (%)	0.75-1" (%)	0.5-0.75" (%)	0.375-0.5" (%)	0.25-0.375" (%)	<0.25" (%)
01023657-1-U	1.13E-05	0.30	0.43	0.17	0.07	0.02	0.01	0.00
01023701-1-U	1.16E-05	0.19	0.33	0.13	0.20	0.09	0.06	0.01
01025230-2-U	1.16E-05	0.30	0.14	0.22	0.20	0.09	0.05	0.00
01023702-2-U	1.17E-05	0.30	0.25	0.17	0.21	0.03	0.04	0.01
01023657-3-U	1.18E-05	0.56	0.17	0.16	0.06	0.03	0.01	0.00
01023695-2-U	1.20E-05	0.06	0.47	0.19	0.20	0.04	0.03	0.00
01023750-U	1.21E-05	0.67	0.00	0.07	0.10	0.08	0.06	0.03
01023582-1-U	1.24E-05	0.27	0.29	0.13	0.13	0.05	0.06	0.06
01025234-1-U	1.30E-05	0.36	0.26	0.11	0.14	0.08	0.05	0.00
01023657-4-U	1.33E-05	0.00	0.33	0.25	0.24	0.09	0.07	0.01
01023707-3-U	1.33E-05	0.47	0.17	0.13	0.12	0.06	0.03	0.01
01023760-2-U	9.85E-05	0.33	0.20	0.23	0.16	0.02	0.04	0.01
01025225-1-U	1.05E-04	0.33	0.27	0.13	0.19	0.06	0.01	0.00
01023689-2-U	1.13E-04	0.23	0.19	0.21	0.24	0.06	0.06	0.01
01023747-3-U	1.15E-04	0.24	0.32	0.11	0.22	0.06	0.04	0.01
01025225-2-U	1.16E-04	0.32	0.31	0.21	0.09	0.04	0.02	0.00
01023692-U	1.18E-04	0.00	0.43	0.19	0.25	0.07	0.06	0.00
01025235-1-U	1.24E-04	0.00	0.40	0.25	0.22	0.06	0.05	0.01
01023703-1-U	1.25E-04	0.16	0.40	0.10	0.18	0.07	0.07	0.02
01023703-2-U	1.31E-04	0.26	0.34	0.11	0.18	0.06	0.04	0.00
01025224-1-U	1.32E-04	0.00	0.55	0.10	0.28	0.03	0.03	0.00
01023690-1-U	1.35E-04	0.00	0.18	0.30	0.35	0.10	0.06	0.01
01025227-1-U	9.65E-04	0.13	0.39	0.22	0.14	0.07	0.05	0.01
01025262-U	5.43E-03	0.48	0.06	0.09	0.23	0.07	0.05	0.01
01025232-1-U	7.45E-03	0.56	0.21	0.07	0.11	0.03	0.03	0.00
01025227-2-U	8.85E-03	0.00	0.46	0.24	0.13	0.07	0.06	0.03

5.3.2. Discussion

In order to determine the relationship between particle size and strain rate, the linear regression method was adopted. The regression equations are shown in the following graphs (the x-coordinate, strain rate, uses the logarithmic scale):

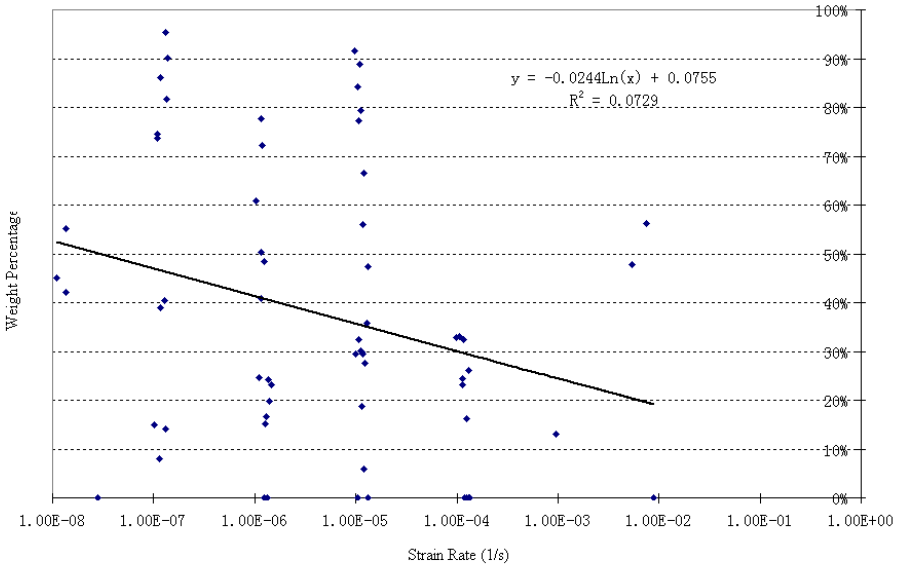

Fig. 5.3 Weight Percentage vs. Strain Rate (1) – Particles larger than 1.5”

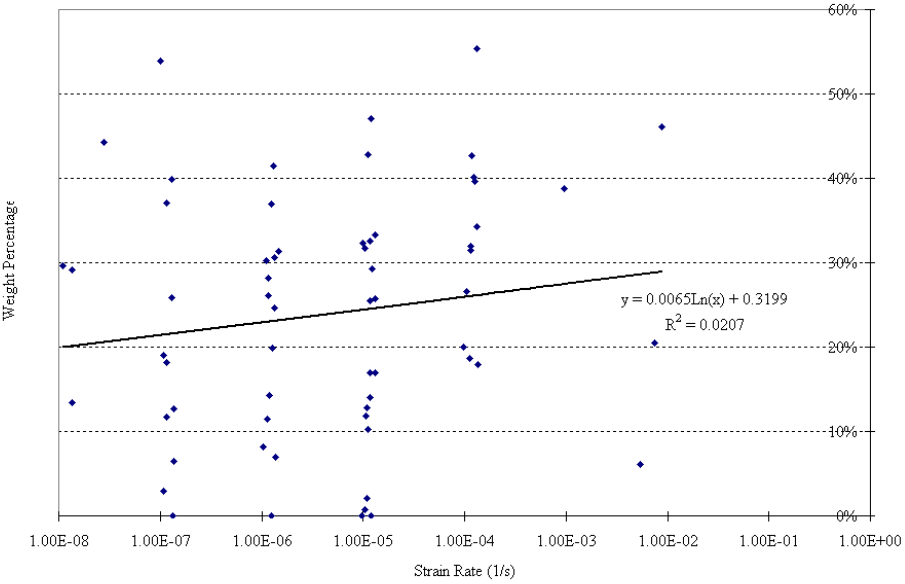

Fig. 5.4 Weight Percentage vs. Strain Rate (2) – Particles between 1” and 1.5”

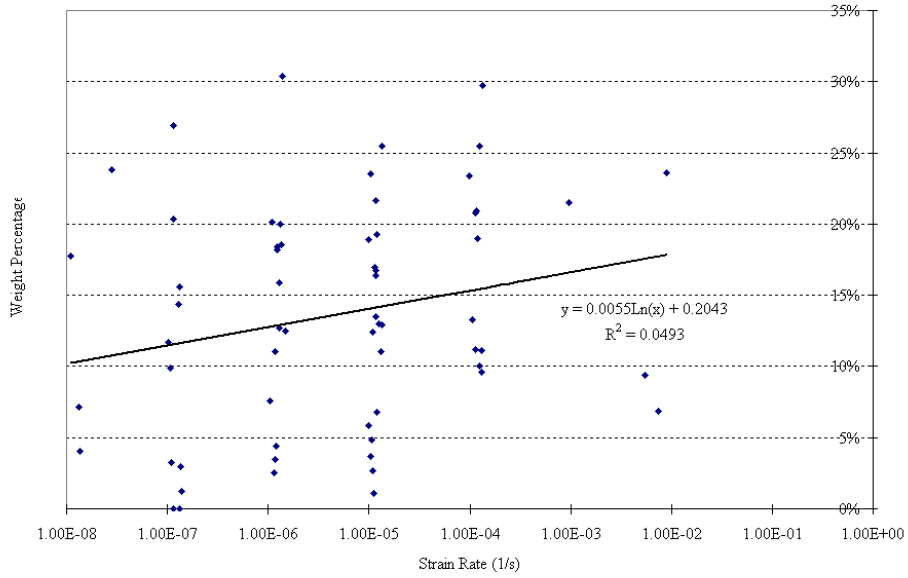

Fig. 5.5 Weight Percentage vs. Strain Rate (3) – Particles between ¾" and 1"

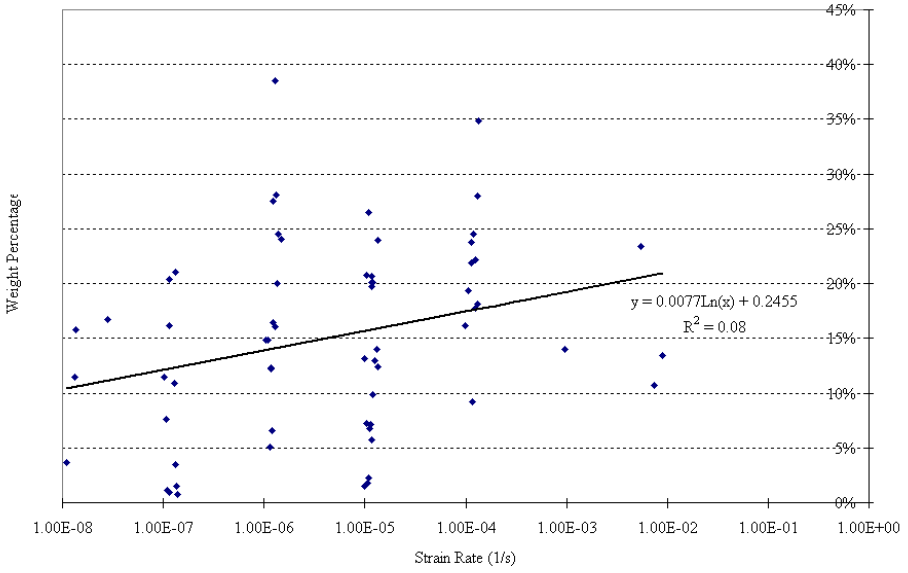

Fig. 5.6 Weight Percentage vs. Strain Rate (4) – Particles between ½" and ¾"

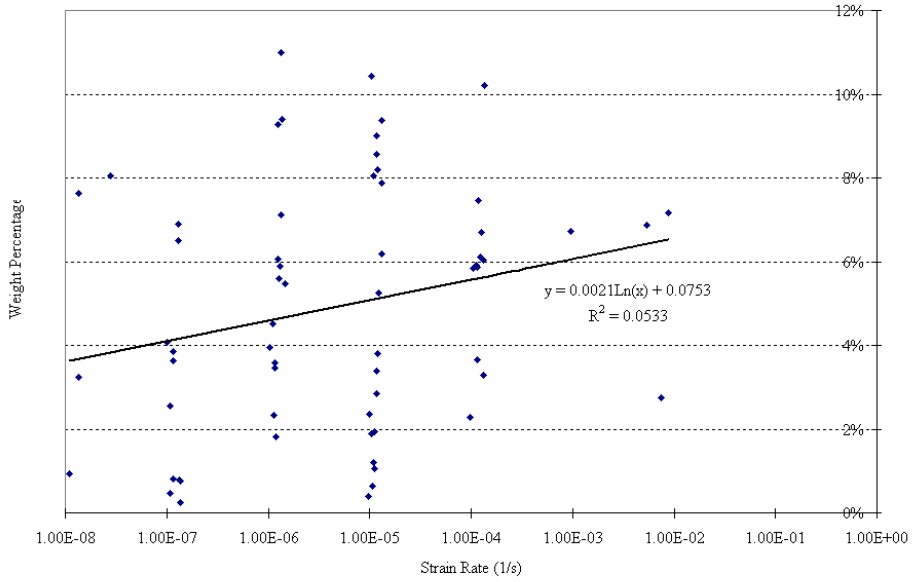

Fig. 5.7 Weight Percentage vs. Strain Rate (5) – Particles between 3/8" and ½"

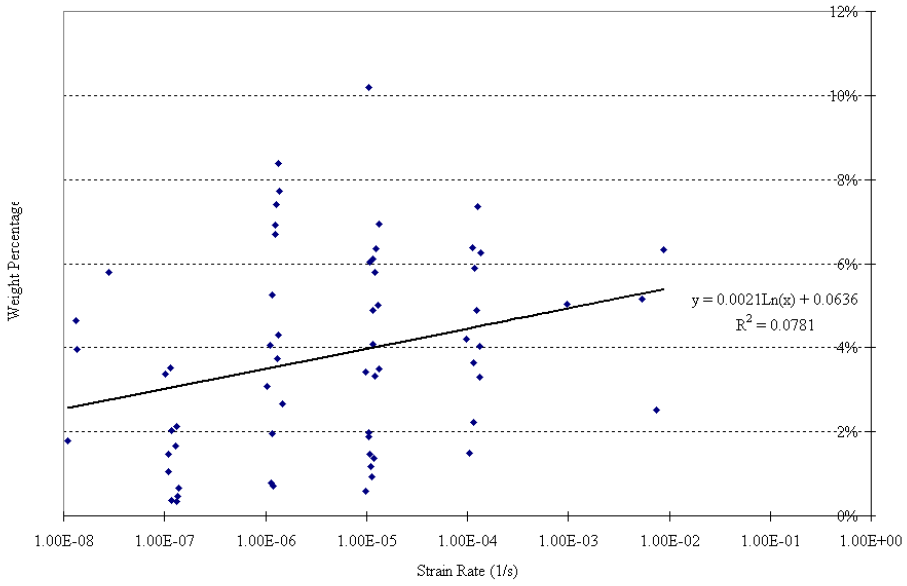

Fig. 5.8 Weight Percentage vs. Strain Rate (6) – Particles between 0.187" and 0.375"

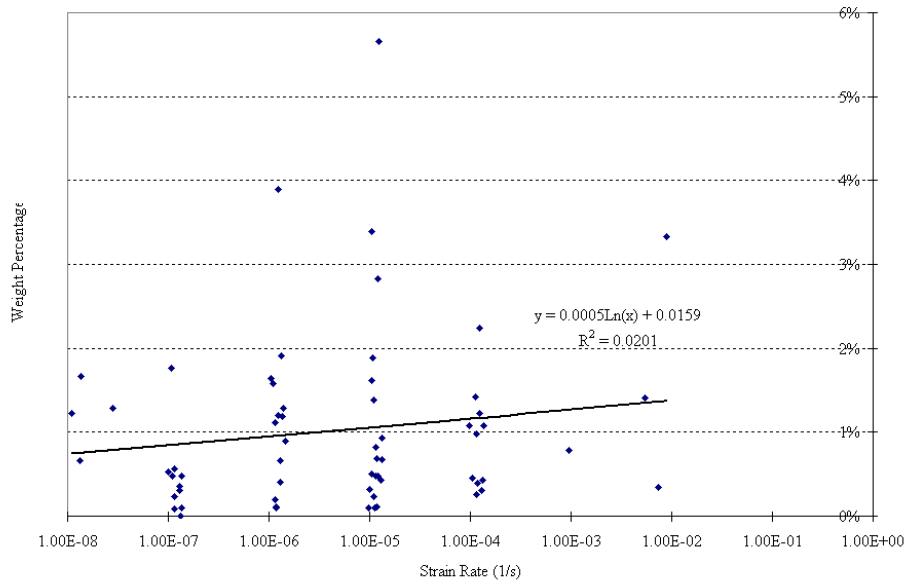

Fig. 5.9 Weight Percentage vs. Strain Rate (7) – Particles smaller than 0.187”

From the graphs we can see that the percentage of the largest particles (larger than 1.5 in) has the trend of going down with increasing strain rate. The fraction of smaller particles tends to increase with increasing strain rate. That is to say, **at the higher strain rate, tuff breaks into smaller pieces.**

The statistical validity of the results is questionable, for at least two reasons: the extreme scatter in the results, typical of many mechanical properties of Yucca Mountain tuffs, and the small number of results at the highest and lowest strain rates.

ARMA/USRMS 06-978

Stress Rate Dependent Strength of a Welded Tuff in Triaxial Tests

Ma, L.
Vector Engineering, Inc., Grass Valley, CA 95945, USA
Zhao, G.
School of Civil Engineering, Jinan University, P.R.China
Sunkara, A. and Daemen, J. J. K.
Department of Mining Engineering, University of Nevada, USA

ABSTRACT: Twenty seven triaxial compression tests have been conducted on welded tuff at constant and controlled axial piston displacement rates. The piston displacement rates were then converted to axial stress rates according to a nearly linear load-displacement relation. Specimens were tested in three orders of displacement rates or stress rates and at three confining pressures. Results of thirty eight uniaxial compression tests were incorporated into the group of triaxial tests. The specimens for the uniaxial tests were collected from the same location in Yucca Mountain as for the triaxial tests. The stress rates for triaxial and uniaxial tests are the same.

Strain gages were used for thirteen triaxial tests and all the uniaixal tests. Tests in three stress rates of the order of 0.4, 0.04 and 0.004 MPa/s and four confining pressures, 0, 5, 10 and 20 MPa were analyzed. Differential axial stress at failure increases with confining pressure and stress rate, both relations following power laws. Volumetric strain increases with confining pressure following an exponential law and decreases with stress rate following a power law. Young's modulus decreases with confining pressure and increases with stress rate. Poisson's ratio increases with confining pressure and stress rate.

1. INTRODUCTION

Results of twenty seven triaxial and thirty eight uniaxial compression tests on welded Topopah Spring tuff are presented. This testing program was a part of an investigation of long-term mechanical behavior of Yucca Mountain tuff in Nevada. Yucca Mountain has been selected as a candidate site for a High Level Nuclear Waste Repository in the United States [1]. The welded Topopah Spring Tuff is where the repository is to be excavated. Units exposed in the Topopah Spring Tuff include the Topopah Spring crystal-poor upper lithophysal zone (Tptpul), the Topopah Spring crystal-poor middle nonlithophysal zone (Tptpmn), the Topopah Spring crystal-poor lower lithophysal zone (Tptpll), and the Topopah Spring crystal-poor lower nonlithophysal zone (Tptpln) [2].

All the test specimens were from the Tptpmn zone. The specimens were prepared from rock drill cores received from the Sample Management Facility (SMF), Yucca Mountain Site Characterization Project. The drill cores were mainly from sidewalls of Alcove 5, which is for drift scale thermal test. The nominal diameter of the cores was 61 mm. For triaxial tests the ratio of length to diameter was controlled in the range of 1.9-2.5 to fit the 61 mm inner diameter Hoek triaxial cell. For uniaxial testing the ratio was between 1.8-2.6.

The triaxial tests were conducted at constant and controlled axial piston displacement rates. The piston displacement rates were then converted to axial stress rates according to a nearly linear load-displacement relation. Specimens were tested at three orders of displacement rates or stress rates and three confining pressures. Results of thirty eight uniaxial tests [3] were incorporated into the group of triaxial tests. The stress rates for triaxial and uniaxial tests are the same.

The average moisture content was 0.7%. The average density is 2.26 g/cm^3. The porosity of the

specimens in Tptpmn zone is in the range of 10-13% [3].

2. EXPERIMENTAL SETUP AND RESULTS

The tests were conducted in an MTS (Material Testing System), servo-controlled hydraulic test system. Load was measured using a load cell. Axial displacement was measured using an LVDT (Linear Variable Differential Transducer) in the MTS. Confining pressure was applied using an MTS servo-controlled hydraulic confining pressure generator which is controlled by the same program as axial load. The confining pressure is applied in such a way that the rate is slightly lower than axial loading rate to meet ASTM 2664 [4]. Strain was measured using electrical resistance strain gages. Four strain gages were used on each specimen for triaxial and six for uniaxial testing. Two or four measure axial strain. Two measure lateral strain. Strain gages were cemented at about midheight of each specimen. Strain in each direction was calculated by averaging all measurements in that direction. Strain gages were used in thirteen triaxial tests and all the uniaxial tests. The triaxial tests were conducted at three confining pressures, 5, 10 and 20 MPa and three stress rates of the order of 0.4, 0.04 and 0.004 MPa/s. Thus tests at four confining pressures and three stress rates are analyzed in this paper. Figure 1 shows a specimen with strain gage wires and the Hoek triaxial cell sitting in the MTS frame.

(a) (b)

Fig. 1. A specimen with strain gages and wires (a), and the Hoek triaxial cell sitting in the MTS frame (b).

Figures 2-5 give curves of differential axial stress (axial stress for uniaxial test)-axial strain (right), curves of differential axial stress-lateral strain (left) and curves of differential axial stress-volumetric strain (middle) for confining pressures 0, 5, 10 and 20 MPa, respectively at different stress rates. Test results used in the following analysis are summarized in Table 1. Volumetric strain is calculated by

$$\varepsilon_v = \varepsilon_1 + 2\varepsilon_3 \qquad (1)$$

where ε_1 is axial strain taken positive and ε_3 lateral strain taken negative.

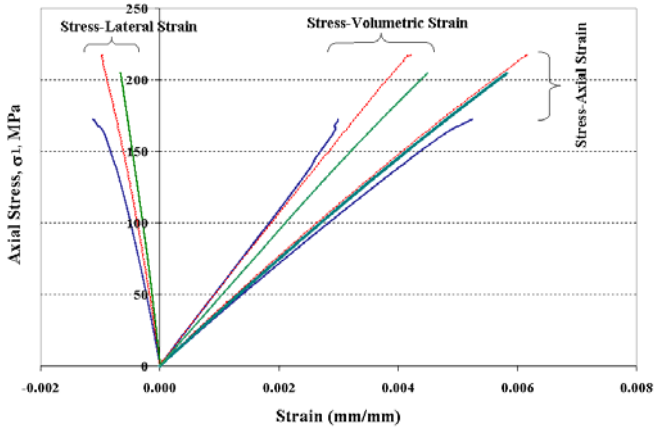

Fig. 2. Stress-strain curves for uniaxial compression tests. Specimen 01023657-3-U: axial stress at failure = 217 MPa, stress rate = 0.3604 MPa/s; Specimen 01023580-U: axial stress at failure = 172 MPa, stress rate = 0.0362 MPa/s; Specimen 01023662-1-U: axial stress at failure = 205 MPa, stress rate = 0.0036 MPa/s.

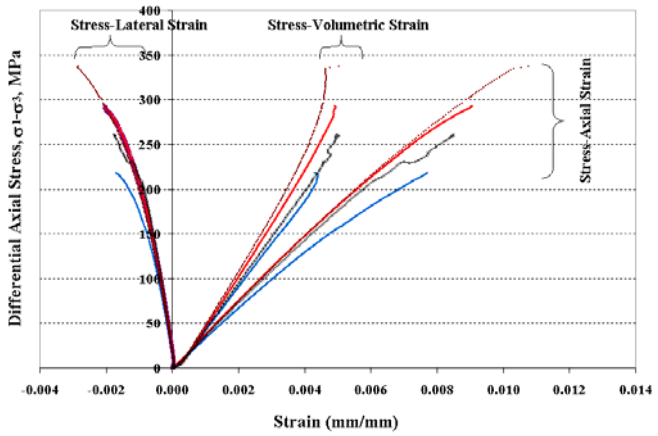

Fig. 3. Stress-strain curves for tests at confining pressure equal to 5 MPa. Specimen 01026153-1-T: axial stress at failure = 337 MPa, stress rate = 0.3772 MPa/s; Specimen 01026226-1-T: axial stress at failure = 262 MPa, stress rate = 0.3647 MPa/s; Specimen 01026258-4-T: axial stress at failure = 293 MPa, stress rate = 0.0038 MPa/s; Specimen 01026241-1-T: axial stress at failure = 218 MPa, stress rate = 0.0035 MPa/s.

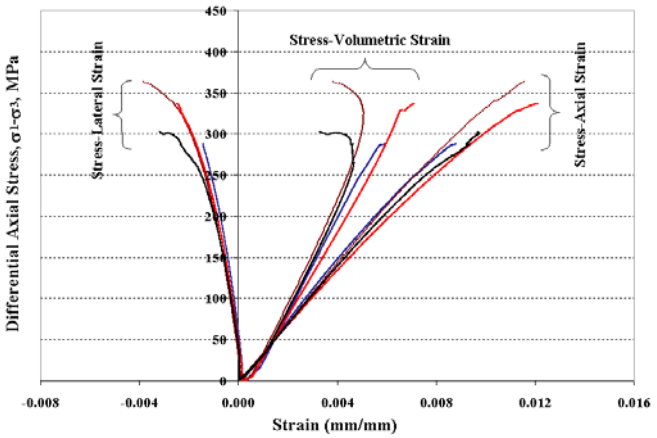

Fig. 4. Stress-strain curves for tests at confining pressure equal to 10 MPa. Specimen 01026144-1-T: axial stress at failure = 363 MPa, stress rate = 0.3743 MPa/s; Specimen 01026227-2-T: axial stress at failure = 303 MPa, stress rate = 0.0396 MPa/s; Specimen 01026225-6-T: axial stress at failure = 336 MPa, stress rate = 0.0375 MPa/s; Specimen 01026145-1-T: axial stress at failure = 288 MPa, stress rate = 0.0037 MPa/s.

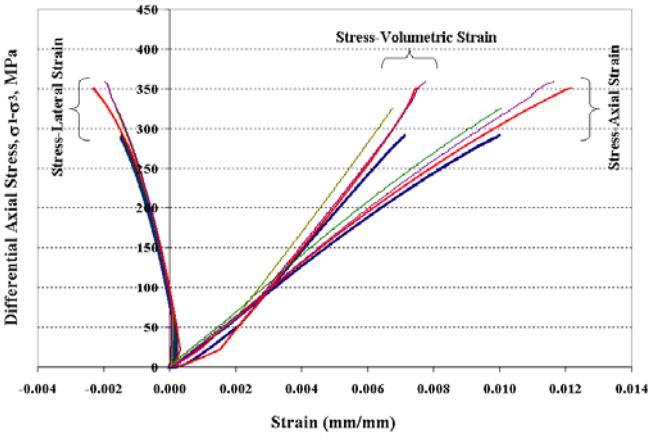

Fig. 5. Stress-strain curves for tests at confining pressure equal to 20 MPa. Specimen 01026145-2-T: axial stress at failure = 325 MPa, stress rate = 0.3952 MPa/s; Specimen 01026229-2-T: axial stress at failure = 358 MPa, stress rate = 0.3872 MPa/s; Specimen 01026255-1-T: axial stress at failure = 351 MPa, stress rate = 0.0036 MPa/s; Specimen 01026146-1-T: axial stress at failure = 292 MPa, stress rate = 0.0035 MPa/s.

3. ANALYSIS AND DISCUSSION

3.1. General observations

All the specimens in uniaxial tests exhibited brittle failure at all stress rates. The brittleness decreases with an increase of confining pressure. In uniaxial tests fractures were nearly parallel to the axis of the specimens, which failed predominantly by longitudinal splitting (Figure 6a). The main mechanism of inelastic deformation in brittle rocks under uniaxial compression is the development of cracks parallel to the compressive stress direction [5, 6]. In triaxial tests the main fracture exhibits inclined shear failure (Figure 6b). The inclination angle (to axis of specimen) increases with an increase of confining pressure. Stress-strain curves for uniaxial tests remain linear until very close to the peak (Figure 2). Nonlinearity increases with increasing confining pressure (Figures 3-5).

(a) (b)

Fig. 6. Specimens after failure: (a) After uniaxial test, longitudinal splitting dominates the failure mode. Specimen ID: 01023657-1-U (stress rate = 0.3805 MPa/s); (b) After triaxial test, shear failure. Specimen ID: 01026241-1-T (stress rate = 0.0035 MPa/s, confining pressure = 5 MPa).

3.2. Stress rate dependence of volumetric strain at failure

Given each stress rate and each confining pressure, volumetric strain at failure versus confining pressure and versus stress rate are plotted in Figures 7 and 8, respectively. To investigate the combined effects of confining pressure and stress rate on volumetric strain at failure, multivariate regression is performed. Eq. (2) is the regression equation that best describes the relationship among them.

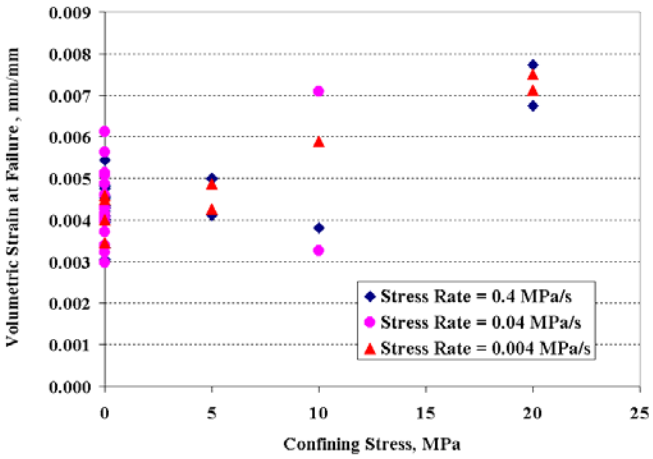

Fig. 7. Volumetric strain at failure as a function of confining pressure for each stress rate.

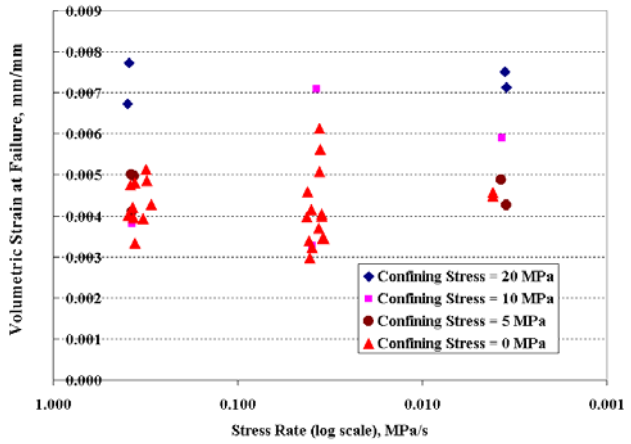

Fig. 8. Volumetric strain at failure as a function of stress rate for each confining pressure.

$$\varepsilon_v = 0.00417 e^{0.0259\,\sigma_3}\,\dot{\sigma}^{-0.00342} \qquad (2)$$

where $\dot{\sigma}$ denotes stress rate. In Eq. (2), volumetric strain at failure increases with an increase of confining pressure in an exponential law and decreases slightly with an increase of stress rate following a power law.

Eq. (2) was estimated using nonlinear regression. The results of the tests with strain measurement in Table 1 were used in the estimation. This regression was conducted using PROC NLIN with Marquardt algorithm in SAS (Version 8.2) program [7]. The PROC NLIN is a procedure to find least squares estimates of coefficients for nonlinear models. The Marquardt algorithm is a direct numerical search method.

In Eq. (2) student t-tests indicate that the coefficient of the whole term in the right hand side and the coefficient of σ_3 are significantly different from zero at the 95% confidence level (both P-values < 0.0001), the exponent of $\dot{\sigma}$ is not (P-value = 0.8, greater than 0.05). Pseudo-R-square for Eq. (2) is 0.52. This value explains the proportion of variance accounted for in the dependent variable by the model. It is equivalent to the R-square, the coefficient of determination, in linear regression.

Brittle failure of the tuff results from crack development [3]. Crack development causes dilatancy [6]. Dilatancy is an inelastic increase in volume due to fracturing. With an increase of confining pressure, more restriction is applied to decrease the dilatancy of a specimen. For a given confining pressure, the longer a specimen takes to fail, the more fatigue crack development and propagation will be created in the specimen. Dilatancy therefore gets larger.

3.3. *Stress Rate dependence of Young's modulus and Poisson's ratio*

Figures 9 and 10 give a plot of Young's modulus versus stress rate and a plot of Poisson's ratio versus stress rate at each confining stress level. Young's modulus and Poisson's ratio were calculated according to ASTM 3148 [8]. Eqs. (3) and (4) are the best estimates of their relations. The equations were estimated using the same method as in section 3.2.

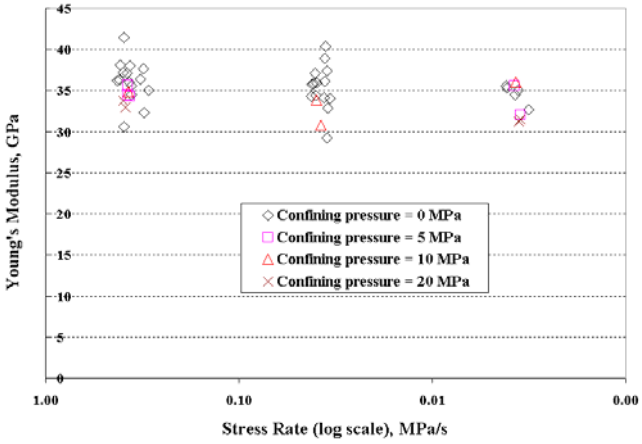

Fig. 9. Young's modulus as a function of stress rate for four confining pressures.

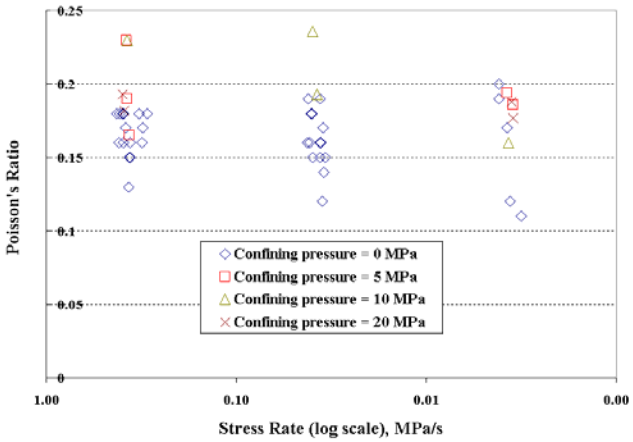

Fig. 10. Poisson's Ratio as a function of stress rate for four confining pressures.

$$E = 36.41 e^{-0.00462\,\sigma_3}\,\dot{\sigma}^{0.0084} \qquad (3)$$

$$\nu = 0.173 e^{0.00973\,\sigma_3}\,\dot{\sigma}^{0.0143} \qquad (4)$$

In Eq. (3) the 36.41 factor on the right hand side (P value < 0.0001) and the coefficient of σ_3 (P-value = 0.0073) are significantly different from zero at the 95% confidence level, the exponent of $\dot{\sigma}$ is not (P-

value = 0.11, greater than 0.05). Pseudo-R-square is 0.22.

Young's modulus decreases with an increase in confining pressure, and increases slightly with an increase in stress rate. The former is the opposite from the observation by Li et al. [9] for the Bukit Timah granite of Singapore. They reported that Young's modulus seems to increase slightly with increasing confining pressure.

From Eq. (4), Poisson's ratio increases with confining pressure and increases slightly with stress rate. The coefficient of the whole term in the right hand side (P value < 0.0001) and the coefficient of σ_3 (P-value = 0.0033) are significantly different from zero at the 95% confidence level, the exponent of $\dot{\sigma}$ is not (P-value = 0.22, greater than 0.05). Pseudo-R-square is 0.19.

3.4. *Stress rate dependency of differential axial stress at failure*

Differential axial stress at failure increases with confining pressure and stress rate as shown in Figures 11 and 12. The brittle strength increases at higher confining pressure, because it becomes more difficult for microcracks to open and propagate. The dependency of differential axial stress on stress rate and confining stress can be best described by a power law (e.g. [10, 11, 12]) as in Eq. (5). Eq. (5) is the best estimation for the test results. When $\dot{\sigma}$ = 1, Eq. (5) is an expression of the relation between differential axial stress at failure and confining pressure at standard loading rate specified in ASTM 2938 [13]. If σ_3 = 0, Eq. (5) reduces to the case of stress rate dependency under uniaxial compression. The intercept in the parenthesis is the average uniaxial strength of the tuff at standard loading rate.

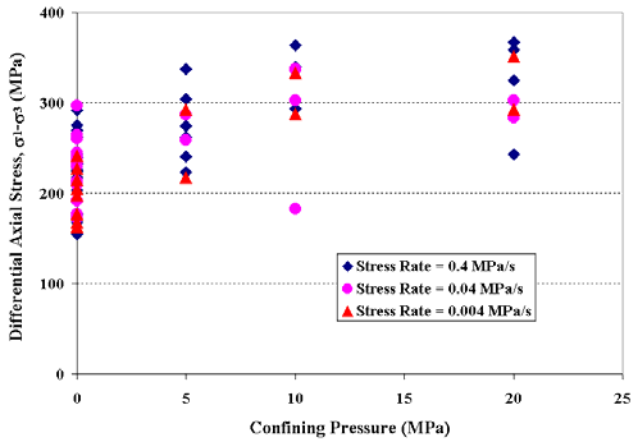

Fig. 11. Differential axial stress as a function of confining pressure for each stress rate.

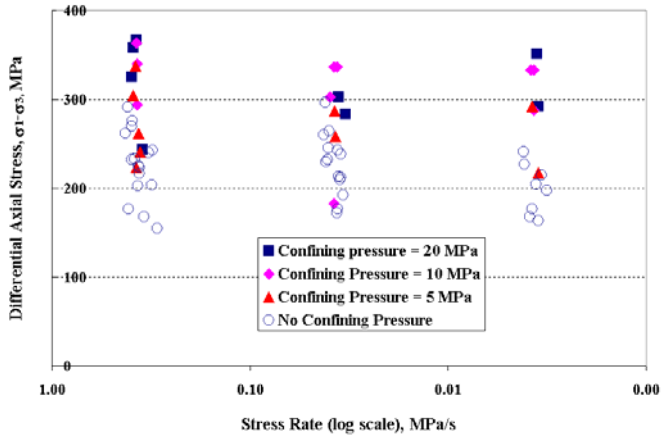

Fig. 12. Differential axial stress as a function of stress rate for each confining pressure.

$$\sigma_1 - \sigma_3 = (229.6 + 31.9\sigma_3^{0.4})\dot{\sigma}^{0.014} \qquad (5)$$

Eq. (5) was estimated using the same procedure described in sections 3.2 and 3.3. Student t-tests indicate that the coefficient and the exponent of σ_3 in Eq. (5) are significantly different from zero at the 95% confidence level (P-value = 0.05 for coefficient, P-value = 0.04 for exponent), but the exponent of $\dot{\sigma}$ is not (P-value = 0.2, greater than 0.05). Pseudo-R-square for Eq. (3) is 0.52. Figure 13 shows a 3-D plot of Eq. (5).

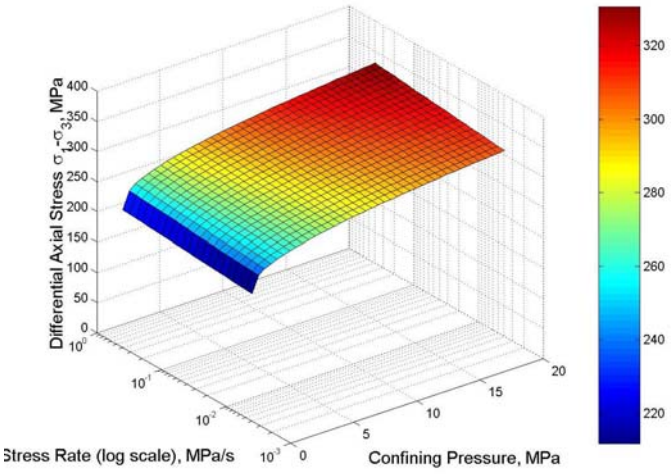

Fig. 13. Differential axial stress as a function of confining pressure and stress rate.

4. CONCLUSIONS

- Brittle failure was observed in uniaxial compression tests at all stress rates.
- Volumetric strain at failure increases with an increase of confining pressure following an exponential law and decreases slightly with an

increase in stress rate according to a power law.

- Young's modulus decreases with an increase in confining pressure following an exponential law and increases slightly with an increase of stress rate following a power law.
- Poisson's ratio increases with confining pressure following an exponential law and increases slightly with stress rate following a power law.
- Differential axial stress at failure increases with confining pressure and stress rate according to a power law.
- These conclusions have to be tempered and qualified by the fact that the data set is small, the rock properties are highly variable, and hence the resulting statistical significance is marginal, at best.

ACKNOWLEDGEMENTS

We thank mr. Jaime gonzalez, doe contract manager and mr. Rick blitz for experimental work.

This paper was prepared by university of nevada reno pursuant to a cooperative agreement fully funded by the united states department of energy, and neither university and community college system of nevada nor any of its contractors or subcontractors nor the united states department of energy, nor any person acting on behalf of either:

Makes any warranty or representation, express or implied, with respect to the accuracy, completeness, or usefulness of the information contained in this report, or that the use of any information, apparatus, method, or process disclosed in this report may not infringe privately-owned rights; or

Assumes any liabilities with respect to the use of, or for damages resulting from the use of, any information, apparatus, method or process disclosed in this report. Reference herein to any specific commercial product, process, or service by trade name, trademark, manufacturer, or otherwise, does not necessarily constitute or imply its endorsement, recommendation, or favoring by the united states department of energy. The views and opinions of authors expressed herein do not necessarily state or reflect those of the united states department of energy.

REFERENCES

1. OCRWM (Office of Civilian Radioactive Waste Management). Website: http://www.ocrwm.doe.gov, September 2004.
2. OCRWM. 1999. *Geology of the ECRB Cross Drift-Exploratory Studies Facility, Yucca Mountain Project, Yucca Mountain, Nevada*, Bureau of Reclamation and U.S. Geological Survey, Denver, Colorado.
3. Ma, L. and J.J.K. Daemen. 2006. Strain Rate Dependent Strength and Stress-Strain Characteristics of a Welded Tuff. *Bull. Eng. Geol.Env.*, http://dx.doi.org/10.1007/s10064-005-0038-6.
4. ASTM D 2664 Standard Test Method for Triaxial Compressive Strength of Undrained Rock Core Specimens without Pore Pressure Measurements. In *Annual Book of ASTM Standards, Section 4, Construction*. Volume 04.08 Soil and Rock; Building Stones. American Society for Testing and Materials, Philadelphia.
5. Walsh, J. B. 1965. The Effect of Cracks on the Uniaxial Elastic Compression of Rocks. *J. Geophys. Res*. 70: 2, 399-411.
6. Brace, W. F., B.W. Paulding, Jr., and C.H. Scholz. 1966. Dilatancy in the Fracture of Crystalline Rocks. *J. Geophys. Res*. 71: 16, 3,939-3,953.
7. Fernandez G. 2003. *Data Mining Using SAS Applications.* Chapman & Hall/CRC.
8. ASTM D 3148, Standard Test Method for Elastic Moduli of Intact Rock Core Specimens in Uniaxial Compression. In *Annual Book of ASTM Standards, Section 4, Construction*. Volume 04.08 Soil and Rock; Building Stones. American Society for Testing and Materials, Philadelphia.
9. Li, H.B., J. Zhao and T.J. Li. 1999. Triaxial Compression Tests on a Granite at Different Strain Rates and Confining Pressures. *Int. J. Rock Mech. Min. Sci.*, Technical Note. 30, 1057-1063.
10. Bieniawski, Z.T. 1974. Establishing the Strength of Rock Mechanics, J. South African Inst. Min. Metallugy. 74, 312-320.
11. Goodman, R. E. 1980. *Introduction to Rock Mechanics*. John Wiley & Sons, New York, p.88.
12. Brady, B.H.G. and E.T. Brown. 1985. *Rock Mechanics for Underground Mining*, George Allen & Unwin, London, p110.
13. ASTM D 2938, Standard Test Method for Unconfined Compressive Strength of Intact Rock Core Specimens. In *Annual Book of ASTM Standards, Section 4, Construction*. Volume 04.08 Soil and Rock; Building Stones. American Society for Testing and Materials, Philadelphia.

Table 1. Summary of triaxial and uniaxial compression test results

Serial #	Specimen ID	σ_3, MPa	$\dot{\sigma}$, MPa/s	σ_1, MPa	E, GPa	ν	ε_v,mm/mm
1	01026149-1-T	10	0.3709	349.65	NA	NA	NA
2	01026154-1-T	5	0.3589	245.59	NA	NA	NA
3	01026155-4-T	5	0.3882	309.54	NA	NA	NA
4	01026157-3-T	5	0.0372	291.97	NA	NA	NA
5	01026158-2-T	10	0.0037	342.99	NA	NA	NA
6	01026160-1-T	20	0.3741	386.53	NA	NA	NA
7	01026160-2-T	10	0.3727	303.57	NA	NA	NA
8	01026237-T	10	0.0378	192.32	NA	NA	NA
9	01026246-1-T	10	0.0038	343.18	NA	NA	NA
10	01026248-4-T	20	0.3492	263.32	NA	NA	NA
11	01026250-2-T	10	0.0365	346.93	NA	NA	NA
12	01026257-1-T	20	0.0359	322.84	NA	NA	NA
13	01026259-1-T	5	0.0371	263.58	NA	NA	NA
14	01026543-1-T	20	0.0330	303.15	NA	NA	NA
15	01026241-1-T	5	0.0035	222.67	32.06	0.19	0.0043
16	01026145-1-T	10	0.0037	297.62	36.01	0.16	0.0059
17	01026146-1-T	20	0.0035	312.23	31.55	0.18	0.0071
18	01026255-1-T	20	0.0036	370.88	31.20	0.19	0.0075
19	01026258-4-T	5	0.0038	297.54	35.60	0.19	0.0049
20	01026153-1-T	5	0.3772	342.13	34.40	0.23	0.0050
21	01026144-1-T	10	0.3743	373.76	34.89	0.23	0.0038
22	01026145-2-T	20	0.3952	344.98	33.77	0.19	0.0067
23	01026541-2-T	5	0.3748	228.3	35.64	0.19	0.0041
24	01026225-6-T	10	0.0375	346.46	30.74	0.19	0.0071
25	01026227-2-T	10	0.0396	312.55	33.88	0.24	0.0033
26	01026226-1-T	5	0.3647	266.74	34.33	0.17	0.0050
27	01026229-2-T	20	0.3872	378.43	33.00	0.18	0.0077
28	01023580-U	0	0.0362	172.00	34.10	0.19	0.0030
29	01023660-1-U	0	0.0039	168.10	33.08	NA	NA
30	01023657-1-U	0	0.3805	233.16	37.14	0.17	0.0041
31	01023697-1-U	0	0.0034	215.19	31.85	NA	NA
32	01023697-4-U	0	0.0035	163.16	29.95	NA	NA
33	01023657-3-U	0	0.3604	216.95	35.58	0.16	0.0042
34	01023662-2-U	0	0.3129	203.36	37.64	0.16	0.0033
35	01023664-U	0	0.3238	239.62	36.39	0.18	0.0040
36	01023701-1-U	0	0.3094	242.89	32.36	0.17	0.0048
37	01023687-1-U	0	0.3921	275.22	41.43	0.16	0.0045
38	01023740-1-U	0	0.3655	225.33	38.02	0.15	0.0040
39	01025224-3-U	0	0.2939	154.49	35.03	0.18	0.0039
40	01025230-2-U	0	0.3951	269.62	37.19	0.18	0.0043
41	01023667-1-U	0	0.0361	176.63	38.96	0.15	0.0032
42	01025259-1-U	0	0.0349	238.26	37.43	0.17	0.0051
43	01025230-1-U	0	0.0352	209.46	29.28	0.12	0.0061
44	01023722-2-U	0	0.0417	296.47	35.75	0.19	0.0049
45	01025235-2-U	0	0.0412	229.75	35.87	0.16	0.0043
46	01023687-2-U	0	0.0357	213.02	40.36	0.16	0.0037
47	01023686-2-U	0	0.0361	242.43	36.16	0.16	0.0041
48	01023695-2-U	0	0.3691	203.02	36.00	0.13	0.0043
49	01025234-1-U	0	0.4137	291.64	36.32	0.16	0.0054
50	01023702-2-U	0	0.3611	223.90	34.48	0.15	0.0048

Table 1 Continued

51	01023691-1-U	0	0.0423	259.94	34.35	0.16	0.0051
52	01023707-1-U	0	0.0339	192.01	34.07	0.15	0.0040
53	01023686-1-U	0	0.0405	232.54	37.12	0.18	0.0040
54	01025260-1-U	0	0.0346	212.17	32.86	0.14	0.0056
55	01023694-2-U	0	0.0401	244.80	34.44	0.18	0.0046
56	01023662-1-U	0	0.0036	204.55	35.04	0.12	0.0045
57	01025226-1-U	0	0.0041	227.37	35.32	0.20	0.0034
58	01023657-4-U	0	0.4254	261.63	36.18	0.18	0.0046
59	01023687-3-U	0	0.0041	241.02	35.58	0.19	0.0040
60	01023707-3-U	0	0.3942	232.55	30.56	0.18	0.0043
61	01023743-1-U	0	0.3418	167.47	37.59	NA	NA
62	01023747-1-U	0	0.0397	264.26	35.91	0.15	0.0034
63	01023750-U	0	0.4105	176.52	38.10	0.18	0.0030
64	01023751-1-U	0	0.0037	176.95	34.51	0.17	0.0034
65	01025233-1-U	0	0.0032	197.48	32.73	0.11	0.0046
Note: NA - Not Available.							

Lithophysal Porosity Effect on Mechanical Properties of Welded Topopah Spring Tuff

Lumin Ma[1] and Jaak J.K. Daemen[2]

1. Vector Engineering, Inc., 143E Spring Hill Dr., Grass Valley, CA 95945, USA
Tel: (775) 771-0899; Email: ma@vectoreng.com
2. Department of Mining Engineering, University of Nevada, Reno, Reno, Nevada, USA
Tel: (775) 784-4309; Email: daemen@mines.unr.edu

Abstract

About 81% of the proposed repository for the permanent disposal of high-level radioactive nuclear waste will be situated in the lower lithophysal unit of the Topopah Spring welded tuff (Tptpll), Yucca Mountain, Nevada, USA, and 4% will be in the upper lithophysal unit (Tptpul). Lithophysae or lithophysal cavities are a major feature in these units (Figure 1). Influence of the lithophysal cavities on properties of the welded tuff was investigated in this study. Seven cylindrical tuff specimens from Tptpll and twelve from Tptpul were tested in uniaxial compression. It was found that both uniaxial compressive strength and elastic modulus decrease with an increase in lithophysal porosity. The relationships between both strength and elastic modulus versus lithophysal porosity can be described with power functions and exponential functions. Exponential fitting has a slightly higher R-square (Figure 2). Sensitivity analysis indicates that sensitivity of strength to porosity is greater than sensitivity of elastic modulus to porosity. The difference between these two results from the dependency of peak axial strain on porosity according to the relationship among strength, strain at failure and elastic modulus. Thus, all three parameters decrease with an increase in lithophysal porosity.

Failure of the tuff specimens exhibited less brittle behavior, certainly for the second and later loading/unloading cycles, and especially as compared to nonlithophysal tuffs, with an increase in porosity. Figure 3 shows failed specimens. Loading/unloading cycles were applied to several specimens (Figure 4). The specimens memorize the unloading stress in the previous cycles before the specimens lost elasticity. A memory loss starts in the third cycle (Figure 4c).

Numerical analysis was conducted to simulate these dependencies using FLAC3D. The results were compared with studies performed by other investigators.

01014759-U, from Tptpll, porosity = 19.2%

01015003-U, from Tptpul, porosity = 22.5%

01015453-U, from Tptpul, porosity = 22.2%

Figure 1 Welded tuff specimens (61 mm diameter) containing lithophysal cavities

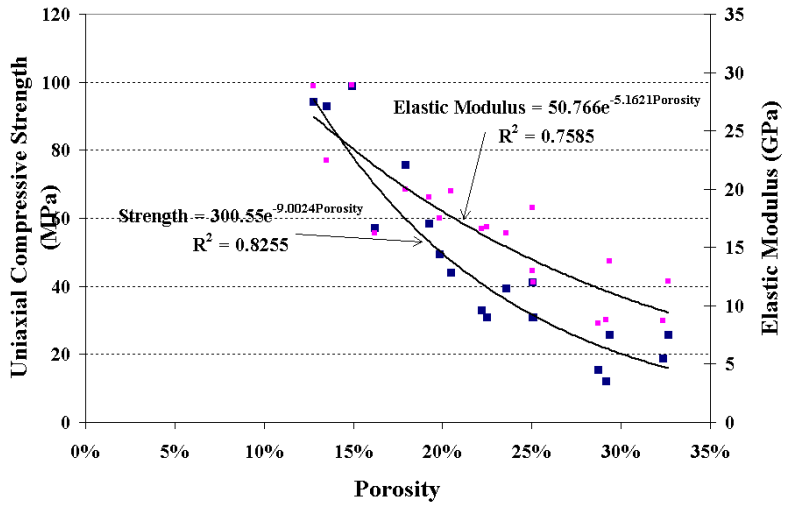

Figure 2 Uniaxial compressive strength and elastic modulus as exponential functions of lithophysal porosity

01014759-U, from Tptpll, porosity = 19.2%

01015003-U, from Tptpul, porosity = 22.5%

01015453-U, from Tptpul, porosity = 22.2%

Figure 3 Tuff specimens after failure (61 mm diameter)

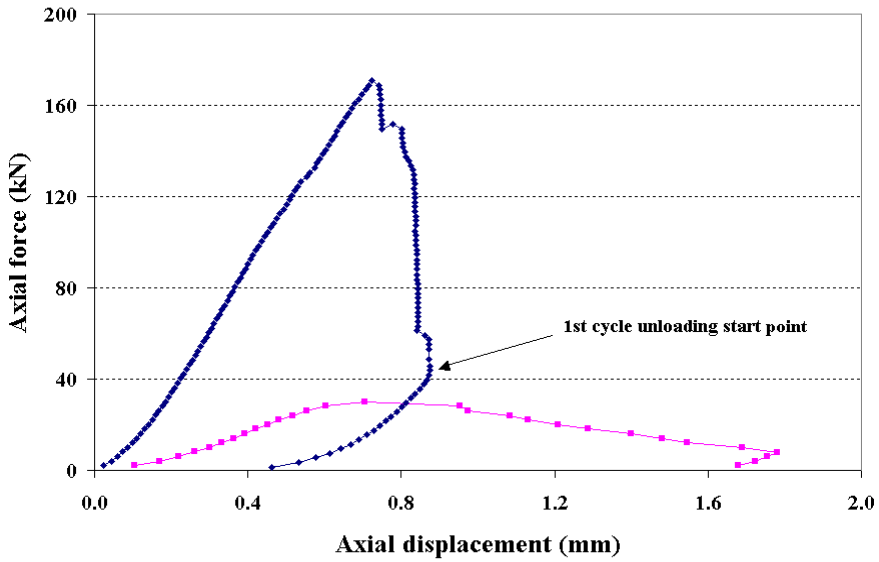

(a) Specimen 01014759-U

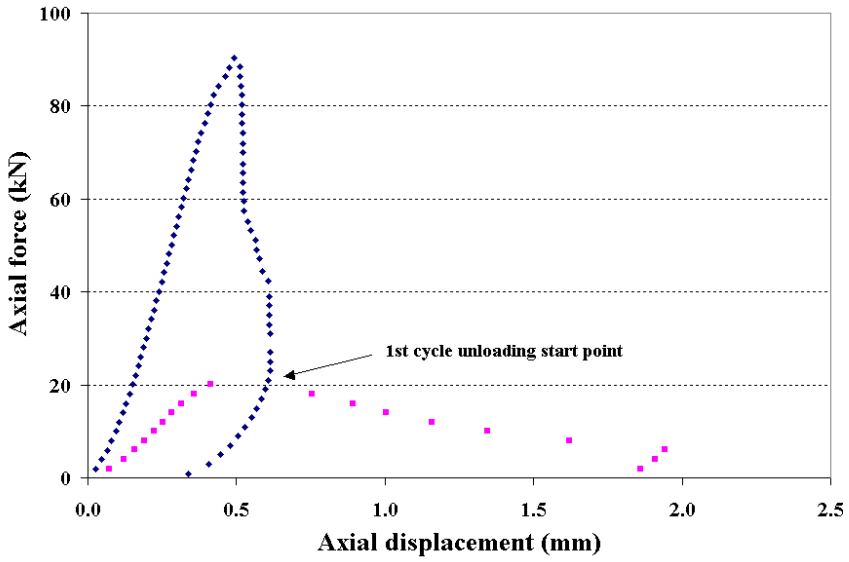

(b) Specimen 01015003-U

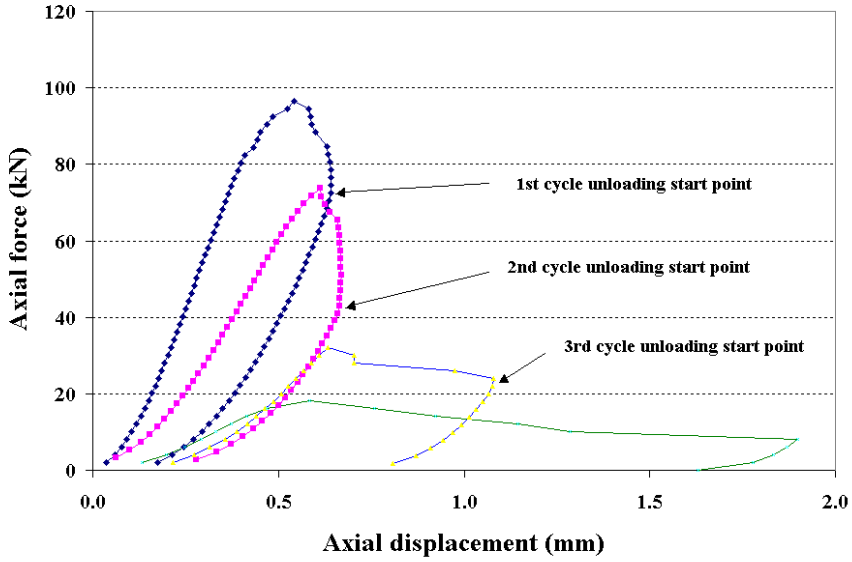

(c) Specimen 01015453-U

Figure 4 Curves of force-displacement with 2 to 4 loading/unloading cycles